BOSTON UNIVERSITY

GRADUATE SCHOOL OF ARTS AND SCIENCES

Dissertation

MEASUREMENT OF THE TOTAL AND DIFFERENTIAL CROSS SECTION OF Z BOSON PRODUCTION IN ASSOCIATION WITH JETS IN PROTON-PROTON COLLISIONS AT SQRT(S) = 13 TEV

by

DANIEL J. ARCARO

B.S., Boston University, 2013

Submitted in partial fulfillment of the

requirements for the degree of

Doctor of Philosophy

2020

Approved by

First Reader

Lawrence R. Sulak, PhD
Professor of Physics

Second Reader

John M. Butler, PhD
Professor of Physics

Acknowledgments

I would like to thank Larry Sulak for his wisdom and guidance in the world of experimental physics. I will carry the knowledge passed down from him throughout my life and future careers. This thesis would not have been possible without the Boston University CMS group and many CMS collaborators elsewhere.

Thank you to my friends and family for their support throughout my education and graduate career. I am especially lucky to have Clover for her collaboration and support during this journey.

MEASUREMENT OF THE TOTAL AND DIFFERENTIAL CROSS SECTION OF Z BOSON PRODUCTION IN ASSOCIATION WITH JETS IN PROTON-PROTON COLLISIONS AT SQRT(S) = 13 TEV

DANIEL J. ARCARO

Boston University, Graduate School of Arts and Sciences, 2020

Major Professor: Lawrence R. Sulak, PhD
Professor of Physics

ABSTRACT

Z boson production in association with jets at the LHC is a major source of background to standard model searches and it provides a sensitive evaluation of the accuracy of perturbative QCD predictions. The production of a Z boson, decaying to two charged muons ($\mu^+\mu^-$), in association with jets in proton-proton collisions at a center-of-mass energy of 13 TeV is presented. The cross sections and their ratios are measured with data recorded by the CMS experiment at the LHC in 2016, corresponding to an integrated luminosity of 35.9 fb^{-1}. The cross sections are measured as a function of observables including the transverse momentum and rapidity of the Z boson, the jet transverse momentum and rapidity for the five highest momentum jets, and jet multiplicity. The measurements are compared with predictions from a multi-leg next-to-leading-order Monte Carlo generator and a next-to-next-to-leading order calculation with next-to-next-to-leading logarithm resummation and parton showering.

Contents

List of Tables

List of Figures

List of Abbreviations

AMC	....	Advanced Mezzanine Card
CMS	....	Compact Muon Solenoid
CSC	....	Cathode Strip Chamber
DT	....	Drift Tube
DY	....	Drell-Yan
ECAL	....	Electromagnetic Calorimeter
FPGA	....	Field Programmable Gate Array
GbE	....	Gigabit Ethernet
HCAL	....	Hadron Calorimeter
HDL	....	Hardware Descriptor Language
HLT	....	High Level Trigger
HPD	....	Hybrid Photo Diode
JHEP	....	Journal of High Energy Physics
JINST	....	Journal of Instrumentation
LHC	....	Large Hadron Colliser
MC	....	Monte Carlo
MCH	....	MicroTCA Carrier Hub
MIP	....	Minimum Ionizing Particle
μTCA	....	micro Telecommunications Architecture
PDF	....	Parton Distribution Function
PMT	....	Photomultiplier Tube
pQCD	....	perturbative Quantum Chromodynamics
PS	....	Parton Shower
QCD	....	Quantum Chromodynamics
QED	....	Quantum Electrodynamics
QIE	....	Charge (Q) Itegrator Encoder
RPD	....	Resistive Plate Chamber
SiPM	....	Silicon Photomultiplier
SM	....	Standard Model

Chapter 1

Introduction and Theoretical Overview

1.1 Introduction

Modeling the strong interaction has been a long standing challenge in the field of particle physics. The challenge arises from the large coupling constant, of order one, at energies near the proton mass of 1 GeV. Our standard choice of perturbation theory cannot work in this strongly coupled regime and new techniques are required to make physical predictions. To add to the large coupling problem, the particles taking part in this interaction, the quarks and gluons, cannot be probed directly and are measured only through the resulting hadrons. In this thesis, we take advantage of the Large Hadron Collider (LHC) at CERN to probe the strong interactions and compare the results to state of the art predictions based on the Standard Model.

1.2 The Standard Model

The Standard Model (SM) [Patrignani et al. (2016)] describes the fundamental particles and their interactions including Quantum Electrodynamics (QED), Quantum Chromodynamics (QCD), and the weak interactions. The model is constructed to be invariant under local transformations of the $SU(3) \otimes SU(2) \otimes U(1)$ gauge group. There are three generations of both quarks and leptons and the interactions are mediated by the gauge bosons. The quarks and leptons are massive spin-1/2 fermions. There are three massive bosons, the W^+, W^-, and Z, that mediate the weak interaction and two massless gauge boson, the photon and gluon, that mediate QED and QCD interactions, respectively. The last particle is a spin-0 massive particle called

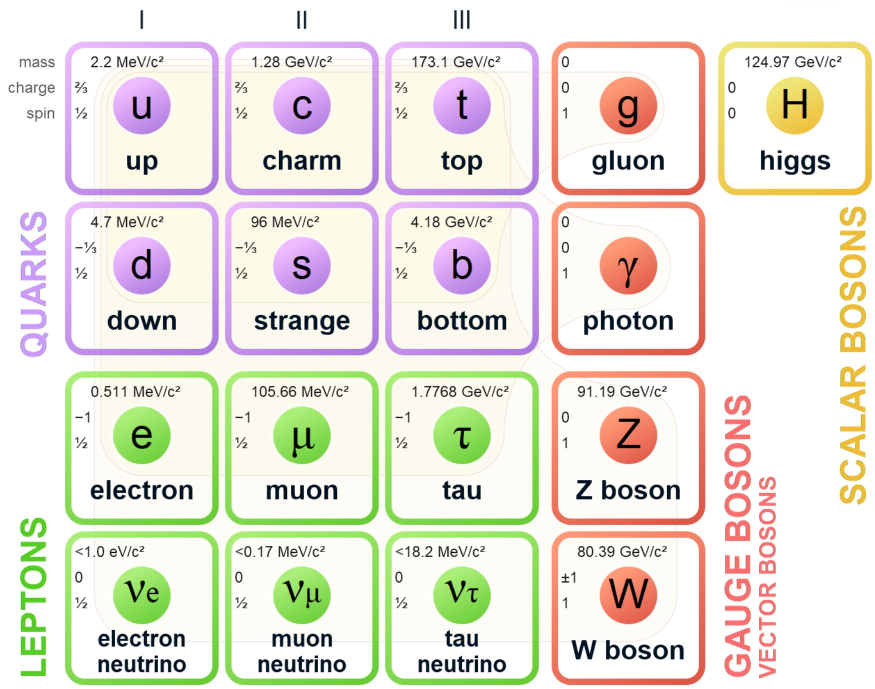

Figure 1·1: Standard Model of Elementary Particles.

the Higgs boson and was discovered at the LHC in 2012 [Chatrchyan et al. (2012b), Aad et al. (2012b)]. All particles and properties can be seen in Figure 1·1. The model is an extremely successful theory predicting precisely the fundamental structure of matter from nuclear decay to high energy scattering.

QED describes the interaction of charged fermions mediated by a photon. Later, QED was found to be part of the larger $SU(2) \otimes U(1)$ electroweak group described by the Glashow-Weinberg-Salam (GWS) theory [Glashow (1961), Weinberg (1967), Salam (1968)]. This incorporated the W and Z bosons and could predict phenomena such as quark mixing with the CKM matrix [Cabibbo (1963)].

QCD is invariant under $SU(3)$ gauge transformations and contains 8 gluon mediators, one for each generator of SU(3), and three generations of quarks. Both quarks and gluons carry color charge that is conserved in QCD interactions. The gluons mediate interactions between quarks and can also interact with other gluons. The gluon self interaction is responsible for asymptotic freedom where the QCD coupling becomes smaller at larger momentum transfers. The self interaction is also thought to lead to color confinement and not allow the observation of colored singlets.

From observation, the weak force, mediated by the W and Z bosons, is found to be short ranged in contrast to QED and the photon. This requires the W and Z to be massive, but a standard mass term in the Lagrangian would not be $SU(2)\otimes U(1)$ gauge invariant. Instead, by including the Higgs mechanism [Higgs (1964)], the electroweak symmetry is broken and three vector boson mass terms as well as a massive scalar Higgs boson are created.

1.3 Proton-proton collisions at the LHC

1.3.1 Parton distribution functions

At the current understanding of the strong interaction, bound states, like the protons in the initial scattering state, cannot be calculated from QCD. Instead, the proton-proton interaction is broken into two parts where one contains the bound structure of the proton and the other contains the hard scattering process. In the hard scattering, the cross section is calculated using perturbative techniques and the incoming partons carry a fraction of the proton's momentum. The momentum distribution of the parton, known as the parton distribution function (PDF), contains the information about the bound state structure of the proton and is extracted from measurements such as deep inelastic scattering. The total cross section is then the hard scattering cross section integrated over the momentum fraction and summed over different partons, q:

$$\sigma = \sum_q \int_0^1 dx_1 \int_0^1 dx_2 f_q(x_1) f_{\bar{q}}(x_2) \hat{\sigma}(x_1, x_2, Q^2) \tag{1.1}$$

The hard scattering term is only a function of the quark momentum and the interaction energy Q^2.

Factorization

As higher order processes are included in the cross section calculation, collinear emissions have to be included and lead to unphysical singularities at low mass. Instead of trying to include the collinear emissions in the hard scattering process, they can be absorbed into the PDF. The PDFs will then gain a dependence on the momentum transfer scale Q^2 as a consequence for absorbing the soft emission terms. We can interpret this dependence as a change in proton resolution with a change in Q^2. As we resolve the proton at a finer scale, or high Q^2, more constituents are present from gluon and quark splitting that can scatter off the incoming particle. The cross section with modified PDFs now becomes:

$$\sigma = \sum_q \int_0^1 dx_1 \int_0^1 dx_2 f_q(x_1, Q^2) f_{\bar{q}}(x_2, Q^2) \hat{\sigma}(x_1, x_2, Q^2) \tag{1.2}$$

A value for Q^2 must be chosen for the PDFs and should correspond to the interaction in the hard scattering process. For most interactions at the LHC the standard choice is the mass of the Z boson (M_Z). Interactions that take place with different Q^2 will lead to logarithmic errors in the factorization technique.

Factorization also leads to a set of equations that describe how the PDFs must evolve as a function of Q^2, known as the DGLAP equations [Altarelli and Parisi (1977)]. These integral-differential equations can evolve a PDF at one scale to another and allow a PDF measurement done at $Q^2 \approx 1\,\mathrm{GeV}^2$ to be used for $Q^2 = M_Z^2$. Many measurements have been made at various energies of the proton PDF and have been combined by various group such as CTEQ [Lai et al. (2010)] and NNPDF [Ball et al. (2013)].

1.3.2 Drell-Yan process

With the PDF measured from experiments, we can combine it with the hard scattering cross section to obtain physical results. In this thesis, the Drell-Yan (DY) [Drell and Yan (1970)] hard scattering process is considered. The DY process is the production of a lepton pair from the $q\bar{q}$ interaction mediated by a photon or Z boson, $Z/\gamma^* \rightarrow \ell^+\ell^-$. The DY process is readily detectable in collisions at the LHC and is commonly accompanied by a strong interaction. More detail of its role in evaluating QCD is given in section 1.4.

We consider a mediator with invariant mass only around the Z mass peak so that the DY process is dominated by the Z mediator. In this thesis, Z production and DY will be used interchangeably. At leading order in perturbative QCD (pQCD), the cross section can be computed exactly using the Feynman calculus from the GWS model and the (a) diagram in Figure 1·2.

$$\begin{aligned} \frac{d\hat{\sigma}}{dcos\theta} &= \frac{1}{128\pi s}(\frac{1}{N_c})^2 \sum_{color}\sum_{spin} |M_{\gamma*} + M_Z|^2 \\ &= \frac{\pi\alpha^2}{2sN_c}[A(1+cos^2\theta) + Bcos\theta] \end{aligned} \tag{1.3}$$

with

$$\begin{aligned} A &= Q_q^2 - 2Q_qV_\mu V_q\chi_1(s) + (A_\mu^2 + V_\mu^2)(A_q^2 + V_q^2)\chi_2(s) \\ B &= -4Q_qA_\mu A_q\chi_1(s) + 8A_\mu V_\mu A_qV_q\chi_2(s) \\ \chi_1(s) &= k\frac{s(s-M_Z^2)}{(s-M_Z^2)^2 + \Gamma_Z^2M_Z^2} \\ \chi_2(s) &= k^2\frac{s^2}{(s-M_Z^2)^2 + \Gamma_Z^2M_Z^2} \\ k &= \frac{\sqrt{2}G_FM_Z^2}{4\pi\alpha} \end{aligned}$$

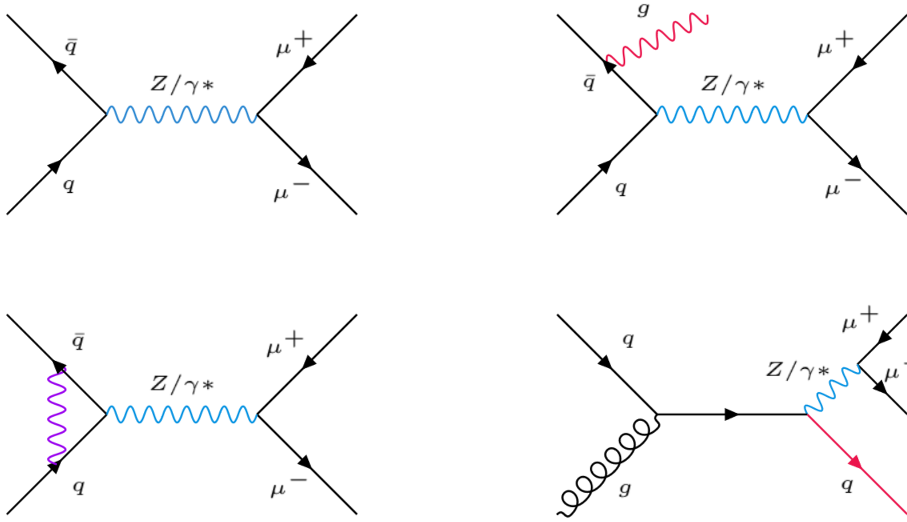

Figure 1·2: (a) Leading-order Drell-Yan process. (b) Next-to leading order process with one jet from initial state radiation. (c) Next-to leading order process with gluon loop. (d) Next-to leading order process with a quark-gluon initial state and one outgoing jet.

where s is the square of the center-of-mass energy and θ is the center-of-mass scattering angle of the outgoing muons, N_c is the number of colors, Q_q is the quark charge, G_F is the Fermi constant, α is the QED coupling constant, Γ_Z is the boson mass width (2.4952 GeV). $A_{\mu,q}$ and $V_{\mu,q}$ are the electroweak coupling constants for the muon and quarks [Patrignani et al. (2016)].

The resonance, in the form of a Breit-Wigner, gives rise to a large cross section around the Z mass. This region is dominated by the χ_2 term and is a results of the the Z exchange. Far away from the Z mass, the Z contributions become negligible and the cross section depends only the photon exchange. In this region the χ_2 term goes to zero and the χ_1 term, from the the $Z - \gamma$ interference, reduces to the photon propagator.

At leading order there are no outgoing partons so the Z transverse momentum is always 0. From the Z longitudinal momentum, measured from the lepton decay products, we can compute the momentum fractions of the incoming quarks. First, we define the Z rapidity of the Z boson y:

$$y = \frac{1}{2} ln(\frac{E + p_z}{E - p_z}) \tag{1.4}$$

Then construct the momentum fractions:

$$x_1 = \frac{M_Z}{\sqrt{s}} e^y \text{ and } x_2 = \frac{M_Z}{\sqrt{s}} e^{-y} \tag{1.5}$$

As we add higher order terms in α_S into the calculation, as seen in (b), (c), and (d) in Figure 1·2, many divergent terms emerge that must be accounted for to produce physical results. In general, the higher order expansion takes the form:

$$\hat{\sigma}(x_i, x_j, Q^2) = \hat{\sigma}_{LO} + \alpha_S \hat{\sigma}_{NLO} + ... \tag{1.6}$$

Similar to the case of factorization, as we correct divergent terms new scales are introduced. The more terms we calculate in the cross section, the smaller the final results depends on these arbitrary scales.

Renormalization

When calculating higher order diagrams, loops of both gluons and quarks need to be included. These terms lead to logarithms of the form $(\alpha_s log(Q^2/M^2))^n$ where M is the renormalization point of α_S and n is the number of loops. Like with factorization, α_S is redefined to absorb these logarithmic terms and we then rely on experimental measurements for α_S. The redefined α_S now has a Q^2 dependence and can be evolved to different Q^2 values using the Callan-Symanzik differential equation [Callan (1970), Symanzik (1970)]. α_S is commonly expressed in terms of Q^2 as:

$$\alpha_s(Q) = \frac{2\pi}{(11 - \frac{2}{3} n_f) log(Q/\Lambda)} \tag{1.7}$$

where n_f is the number of quarks and Λ is called the QCD scale. With multiple points of α_S measured at different Q^2 values, Λ is found to be $\sim 200\,\text{MeV}$.

Both the total and fully differentiable Drell-Yan cross section have been calculated to next-to-next leading order (NNLO) in perturbative QCD. Incorporating the NNLO changes the total cross section value by $\sim 3\%$ and typically has lower uncertainties compared to NLO. The uncertainties are reduced because of the reduced dependence on the renormalization scales.

1.3.3 Jet formation

Parton Shower

Even at NNLO in pQCD we cannot fully describe the interactions at the LHC where events can have many more outgoing partons. Instead of trying to fully describe the extra particles in pQCD, a method called the parton shower (PS) is used. The PS will estimate initial and final state radiation and generate more outgoing particles to mimic higher order calculations. The initial and final state radiation is done in steps where a probability is calculated for the splitting of a quark or gluon into lower momentum particles. The probability is calculated using solutions to the DGLAP equations and works by evolving the higher energy partons down to the scale of Λ ($\sim$200 MeV). Once the parton energies reach a cutoff scale the showering is stopped.

Hadronization

As mentioned earlier, hadrons are only observed in color singlet states because of color confinement. As two quarks are pulled apart the energy input into the system is enough to cause new quark-antiquark pairs to be created and form new color singlet state. This process is called hadronization and continues until all outgoing particles are color neutral. This process of hadronization is not calculable from QCD and instead effective models are used in MC generators. One effective theory, called the

Lund string model, uses a linear potential energy $V(r) = kr$ (k=1 GeV/fm) between two quarks. When the separation of the quarks is large enough, a quark-antiquark pair is produced. The "strings" between quarks are broken with the produced pairs and the process continues until only color singlets remain. The hadronization done in Pythia is based off this Lund string model. Short lived hadrons can then decay further using their particular lifetime before reaching the detector. The cluster of hadrons, which tend to be central around the initial outgoing parton from the hard scattering, is detected as a large spray of particles and is called a jet.

1.4 Drell-Yan at the LHC

To probe the strong interaction we take advantage of the worlds highest energy p-p scattering experiment at the Large Hadron Collider [Bruning et al. (2004)] using the Compact Muon Solenoid (CMS) detector [CMS (1994)]. The p-p collisions are dominated by the strong force and are a perfect testing ground for QCD predictions. As a consequence, events are noisy due to QCD radiation and multiple scatterings, so purely QCD events are difficult for CMS to reconstruct accurately. Instead, we employ a tagging particle in the Drell-Yan process, the Z boson, to select events and use as a well understood recoil object to the outgoing hadrons. The Z boson events will test our modeling in three regimes: the perturbative high energy tail, the low energy strongly coupled region, and large multiplicity events with higher order perturbative terms. The strongly coupled region is captured at low Z transverse momentum, where the Z is sensitive to soft QCD emissions. In high energy tails we can study the accuracy of perturbative QCD. Lastly, with large multiplicity events we can measure how higher order terms are modeled by the parton shower.

The clean and readily identifiable signature and large production rate of the DY process provides an opportunity to measure cross sections at the $\sim 5\%$ systematic limit of CMS. This precision can be used to accurately constrain the parton distribution functions (PDFs) and test how the factorization techniques and DGLAP equations hold at higher energies. We can also probe the strong coupling constant α_S and similarly compare it to the Callan-Symanzik evolution equation.

With the increased precision, any deviations in our predictions will excite work on new techniques to provide better agreement with experiment as well as improved theoretical uncertainty. An accurate understanding of this process is also critical in other Standard Model (SM) measurements and searches for physics beyond the SM. The DY process is an important background to Higgs boson production and signatures of both dark matter and supersymmetric particle production.

In addition to these physics motivations, Z + jets production serves as an important experimental benchmark. It is a key ingredient in calibrating several parts of the detector including the jet energy scale. Any improvements in modeling QCD will directly benefit the calibration techniques since they rely heavily on predictions from Monte Carlo (MC) based event generators and reliable higher-order theoretical calculations.

Differential cross sections of the Z boson in association with jets has been previously measured by CMS, ATLAS, and LHCb at center-of-mass energies of 7, 8, and 13 TeV [Aad et al. (2012a), Aad et al. (2013), Chatrchyan et al. (2012a), Khachatryan et al. (2015b)], [Khachatryan et al. (2015a), Khachatryan et al. (2017a), Aaij et al. (2016)] [Aaboud et al. (2016), Sirunyan et al. (2018)], and by CDF and D0 Collaborations at a center-of-mass energy of 1.96 TeV [Aaltonen et al. (2015), Abazov et al. (2008)].

This thesis expands upon the results at 13 TeV with a factor of 10 more integrated luminosity and a better characterized CMS detector. The first measurement of rapidity correlations between the Z and jets at 13 TeV is made. From the increased data set size, the first double differential as a function p_{T} and y is measured. We have also extended the jet transverse momentum measurements well into the TeV range.

Single and double differential cross sections of Z production are presented, decaying to a pair of oppositely charged muons, in associations with jets in proton-proton collisions at $\sqrt{s} = 13\,\mathrm{TeV}$ with an integrated luminosity of $35.9\,\mathrm{fb}^{-1}$ recorded in 2016 by CMS. Cross-sections are measured as a function of jet multiplicity (N_{jets}) and the jet kinematic, rapidity (y) and transverse momentum (p_{T}) of the individual jets, where the jets are ordered by decreasing p_{T}. Jet kinematic variables are presented for events with at least 1, 2, 3, 4, 5 jets as "inclusive" to designate events with at least N jets and as "exclusive" for events with exactly N jets. Furthermore, cross sections are measured as a function of the scalar sum of the jet transverse momenta (H_{T}) for events up to 5 energetic jets.

Chapter 2

The Compact Muon Solenoid

2.1 The CMS Detector

The central feature of the CMS apparatus is a superconducting solenoid of 6 m internal diameter, providing a magnetic field of 3.8 T. Within the solenoid volume is a silicon pixel and strip tracker, a lead tungstate crystal electromagnetic calorimeter (ECAL), and a brass and scintillator hadron calorimeter (HCAL), each composed of a barrel and two endcap sections. Forward calorimeters on each end extend the pseudorapidity coverage close to the beam pipe. Muons are detected in gas-ionization chambers embedded in the steel flux-return yoke outside the solenoid.

The silicon tracker measures charged particles within the pseudorapidity range $|\eta| < 2.5$. It consists of 1440 silicon pixel and 15,148 silicon strip detector modules. For non-isolated particles of $1 < p_{\mathrm{T}} < 10\,\mathrm{GeV}$ and $|\eta| < 1.4$, the track resolutions are typically 1.5% in p_{T} and 25–90 (45–150) μm in the transverse (longitudinal) impact parameter [Chatrchyan et al. (2014)].

The ECAL consists of 75,848 lead tungstate crystals, which provide coverage in pseudorapidity $|\eta| < 1.48$ in a barrel region (EB) and $1.48 < |\eta| < 3.0$ in two endcap regions (EE). Preshower detectors consisting of two planes of silicon sensors interleaved with a total of 3 interaction lengths of lead are located in front of each EE detector. In the barrel section of the ECAL, an energy resolution of about 1% is achieved for unconverted or late-converting photons that have energies in the range of tens of GeV. The remaining barrel photons have a resolution of about 1.3% up to a pseudorapidity of $|\eta| = 1$, rising to about 2.5% at $|\eta| = 1.4$. In the endcaps, the resolution of unconverted or late-converting photons is about 2.5%, while the remaining endcap photons have a resolution between 3 and 4% [Khachatryan et al. (2015d)].

The HCAL is describe in detail in section 2.2. When combining information from the entire detector, the jet energy resolution amounts typically to 15% at 10 GeV, 8% at 100 GeV, and 4% at 1 TeV, to be compared to about 40%, 12%, and 5% obtained when the ECAL and HCAL calorimeters alone are used.

Muons are measured in the pseudorapidity range $|\eta| < 2.4$, with detection planes made using three technologies: drift tubes (DT), cathode strip chambers (CSC), and resistive plate chambers (RPC). Matching muons to tracks measured in the silicon tracker results in a relative transverse momentum resolution, for muons with $20 < p_{\mathrm{T}} < 100\,\mathrm{GeV}$, of 1.3–2.0% in the barrel and better than 6% in the endcaps. The p_{T} resolution in the barrel is better than 10% for muons with p_{T} up to 1 TeV [Chatrchyan et al. (2012c)].

In the region $|\eta| < 1.74$, the HCAL cells have widths of 0.087 in pseudorapidity and 0.087 in azimuth (ϕ). In the η-ϕ plane, and for $|\eta| < 1.48$, the HCAL cells map on to 5×5 arrays of ECAL crystals to form calorimeter towers projecting radially outwards from close to the nominal interaction point. For $|\eta| > 1.74$, the coverage of the towers increases progressively to a maximum of 0.174 in $\Delta\eta$ and $\Delta\phi$. Within each tower, the energy deposits in ECAL and HCAL cells are summed to define the calorimeter tower energies, and are subsequently used to provide the energies and directions of hadronic jets.

Events of interest are selected using a two-tiered trigger system [Khachatryan et al. (2017b)]. The first level (L1), composed of custom hardware processors, uses information from the calorimeters and muon detectors to select events at a rate of around 100 kHz within a time interval of less than 4 μs. The second level, known as the high-level trigger (HLT), consists of a farm of processors running a version of the full event reconstruction software optimized for fast processing, and reduces the event rate to around 1 kHz before data storage. A more detailed description of the CMS detector, together with a definition of the coordinate system used and the relevant kinematic variables, can be found in Ref. [Chatrchyan et al. (2008)].

2.2 The CMS Hadron Calorimeter

2.2.1 Calorimeter Design

The Hadron Calorimeter of the CMS detector is a Shashlik sampling calorimeter designed to measure the energy of outgoing hadrons. It uses heavy absorber layers to induce showers from incident hadrons and thin layers of active material to sample the energy of the shower. The shower from an incident hadron typically has two distinct components; one hadronic and the other electromagnetic. The hadronic component consists of nuclear recoils in the absorber and has a radiation length of ∼15 cm in brass. From these nuclear interactions π^0 particles are created and quickly decay to two photons that initiate the electromagnetic component of the shower. The photons undergo pair production when interacting with a nucleus and produce electron-positron pairs that then produce more photons from bremsstrahlung. This process cascades into a shower and has a characteristic length of ∼1 cm in brass; much shorter than the hadronic component.

Any charged particles such as a $\pi^{\pm}$ or protons in the hadronic component or electrons in the EM component will excite electrons in the active material to the conduction band. The excited electrons relax and emit light typically in the ultraviolet range. Fluors are embedded in the plastic to convert the light into the blue spectrum. The light is extracted from the active material through a plastic wavelength shifting fiber wrapped once around the active layer. The wavelength is shifted to green to match the greatest conversion efficiency of the photo detectors. Clear fibers are spliced to the wavelength shifting fiber to bring the light to the photo detector mounted on the outside of CMS.

The geometry of the detector shown in Figure 2·1 is optimized to capture a full shower along the radial direction out from the interaction point. The detector is broken up into many trapezoidal towers that each point towards the interaction point and the light from a single tower is integrated with approximately three photo-detectors. This geometry gives the energy of a shower deposited in one η-ϕ area and approximately three radial sections. Each tower includes ∼17 layers of 5 cm of brass and 1 cm of scintillator. One tower will produce ∼20 photo-electrons from a minimum ionizing particle (MIP) passing completely through and achieves the sensitivity design goal of 3σ certainty for MIP detection.

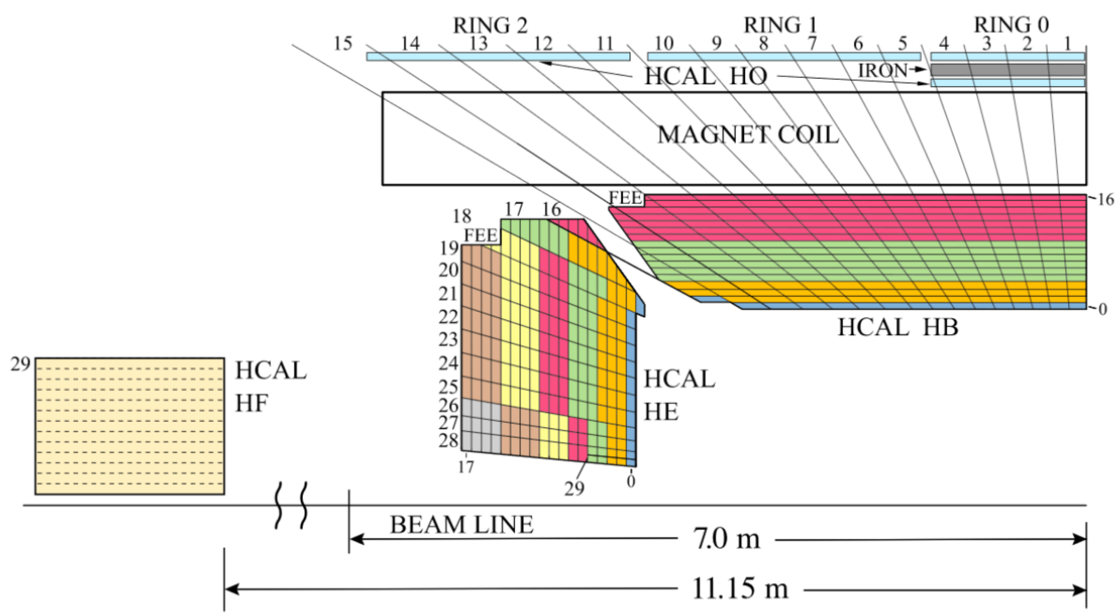

Figure 2·1: HCAL layout and segmentation in the Z-η plane.

The HCAL Barrel (HB) covers the range of $0 < |\eta| < 1.3$ and the full circle in ϕ. The barrel is broken up into 36 wedges in the ϕ direction and 17 in the η direction.

The HCAL Endcap (HE) covers $1.3 < |\eta| < 3.0$ with 36 wedges in ϕ. HB and HE are joined such that each covers the projection to the interaction point with a fraction of a tower. HO has two layers of scintillator with one placed outside the solenoid and another after the first steel return yoke. These two layers cover out to $|\eta| = 1.26$.

The HCAL forward calorimeters (HF) are located 11.2 m from the interaction point and extend the pseudorapidity coverage overlapping with the endcap from $|\eta| = 2.9$ down to $|\eta| = 5$. HF uses a steel absorber with embedded quartz fibers as the active media. The light is generated from Cherenkov radiation and not scintillation light.

Two forms of active calibration are built into the HCAL system: sourcing and laser. The sourcing is done though a series of tubes where a radioactive source (typically Cobalt-60) attached to a wire can be moved around HCAL. The laser system consists of another set of quartz fibers to inject laser light directly into the scintillating tiles. These two calibration methods will allow for monitoring of gain of the photo-detectors and light yield of the scintillator tiles.

2.2.2 Signal Transducers

Three technologies for converting light into electrical signals are used within HCAL for Run II. HB remained original with Hybrid Photo Diodes (HPD), HE was upgraded with Silicon Photo Multipliers (SiPM), and HF used Photomultiplier tubes (PMT).

The HPD uses the photoelectric effect to convert the incident light into electrons much like a PMT. The electrons are then accelerated with a strong field ($\sim 10^6 V/m$) in a vacuum into doped silicon. The resulting shower from the electron drifts to the back of the doped silicon to an array of avalanche diodes that produce the final signal. Fibers from each towers are bundled together (∼18 fibers) and mounted to a single HPD so that an HPD output is the sum of a full tower. The gain of the HPD at ∼7 kV is 2000 and produces ∼0.3 fC/photoelectron or ∼0.2 GeV/ fC.

Silicon photomultipliers (SiPM) are used in HO for all of Run II and have been installed in HE during the extended year end technical stop (EYETS). SiPMs have a gain of $\sim 10^6$ vs the HPD gain of $\sim 10^3$ and do not require high voltage. The higher gain will improve MIP detection and compensate for the lower light yield from the radiation damaged scintillators.

Each SiPM consists of a pixel array of avalanche photodiodes operating in Geiger mode. This means any carriers produced in the depletion region of the photodiode will create an avalanche and turn the pixel completely "on". Summing the current essentially counts the number of pixels turned on and is proportional to amount of light incident on the device. Since the number of pixels is finite there can be saturation for higher amounts of light incident on the device. This creates a non-linear scale for converting current to incident photons that must be taken into account when calculating energy deposits.

Geiger mode is achieved by bringing the reverse bias higher than the break down voltage of the silicon. One carrier created by a photon can cause a full avalanche and allow the device to detect single photons. The current generated by the break down will continue until the reverse bias voltage is brought below the breakdown voltage. This is usually done passively using a resistor in parallel with the diode. Once the current dissipates the voltage will return to above the breakdown voltage and the pixel will be reset. The full recovery time is ~5-10 ns which is fast enough to have a single pixel fire twice from a single scintillator signal. Since the SiPM consists of a large number of pixels many scintillator tiles can be paired with a single SiPM. Fibers are bundled like for the HPD case and mounted to a single SiPM.

Since HF is outside the strong magnetic field it uses conventional photomultiplier tubes. Quartz fibers embedded in the steel produce blue Cherenkov light that is routed directly to the PMTs. The Cherenkov radiation produces few photons compared to scintillation so the PMT gain is much higher at 15-75 fC/photoelectron.

2.2.3 Digitization and Readout

All of the transducer signals are digitized using an ASIC called the Charge (Q) Integrator Encoder (QIE). The main challenges for the QIE are to achieve accurate integration over each 25 ns bunch crossing with no deadtime and maintain a dynamic range of $\sim 10^4$. The 25 ns integration is achieved by using four integrators in each QIE chip that cycle every bunch crossing. Once 25 ns has elapsed one of the integrators sends the amount of charge to the next stage and the second integrator takes over for the next 25 ns. The cycle of the full chip to produce the final digital signal is done in four stages: integrate, compare, digitize, reset and takes 100 ns.

The range of the QIE with a transducer gain of 15–75 fC/photoelectron is ∼2.7–27 pC. In HF this corresponds to an energy of a few GeV to 5 TeV. Because of the improved SiPM gain, the QIE chips can relax the lowest sensitivity from 1 fC to as much as 3 fC and still retain a 10:1 signal to noise ratio for a single photon incident on the array (1 pixel on). The gains of the HF PMTs and SiPMs are the same order of magnitude so the newer QIE10 chips can have the same integration range for both positive and negative inputs. Some of the signal can be used to measure the pulse length through a TDC on the QIE10. More sensitivity as well as a smaller form factor for the device is allowing for more segmentation in the towers by a factor of ∼3 after EYETS.

2.3 Back End Electronics

2.3.1 Introduction to FPGA's

A Field Programmable Gate Array (FPGA) is a large array of logic blocks ($\sim 10^6$) that can be re-wired through an electrical signal. The ability to re-wire enables an

FPGA to change its output without changing the hardware. This provides a useful platform for projects that rely on frequent modification and bug fixes. Designing an ASIC to do the same job typically results in faster and more efficient computation, but future changes need to be planned for or would be impossible without building an entirely new ASIC.

The wiring of an FPGA is determined typically from proprietary software provided by the chip manufacture (called place-and-route software) using the logic code of the user. The logic code is written in a Hardware Descriptor Language (HDL) and a network of logic operations and interconnects called an netlist is created that replicates the HDL. The place-and-route then creates a file to load on the FPGA that will replicate the netlist using the specific FPGA.

Since the logic operations are evaluated on a clock cycle the timing of the system is predictable. This is crucial to make sure calculations from one bunch crossing propagates together and never mixes with another bunch crossing. Synchronization, together with the millions of logic blocks available in modern FPGAs, allows for parallel operations with predictable output timing.

2.3.2 Micro Telecommunications Crate

The Micro Telecommunications Architucture (μTCA) crate is defined by a backplane that houses 12 Advanced Mezzanine Cards (AMCs), two μTCA Carrier Hubs (MCH), and two power modules. For use in CMS the second MCH is replaced by a custom control card called the AMC13 [Hazen et al. (2013)] for clock, timing distribution, and data acquisition. The 12 AMCs are subdetector specific and can provide 1.0–3.125 Gb/s of throughput, fast data processing, and slow control for downstream components. The stock MCH provides Gigabit Ethernet (GbE) for remote control of all cards in the crate. All AMCs are connected to the MCH slots through the backplane through bidirectional links to send data and control signals.

2.3.3 HCAL Trigger and Readout Card

The HCAL Trigger and Readout Card (μHTR) is an AMC designed for HCAL to calculate trigger information for the regional calorimeter trigger (RCT) and store the event fragments until the trigger signal is returned through the AMC13. The trigger primitives (TPs) are calculated by converting the ADC values from the front end to E_T and sum portions of the detector. The conversion of ADC to energy is done by a look-up table (LUT) stored on the μHTR that contains the conversion for all ADC values for the specific region of HCAL. Each tower of HCAL is then summed before being sent to the RCT. In parallel to the TPs, the raw event fragments are stored in a first in first out (FIFO) pipeline of length $\sim$3.2 μs.

If the event passes both the RCT and global trigger a Level-1 Accept signal (L1A) is propagated through the AMC13 to the μHTR and the corresponding event fragment is sent to the AMC13. If no trigger is received the event fragment is overwritten after the $\sim$3.2 μs.

2.3.4 AMC13

Since its installation in 2015 the AMC13 has been in operation for many subsystems within the Compact Muon Solenoid detector at CERN. Along with other components of CMS the AMC13 has undergone several developments throughout its run to the hardware configuration and firmware. For the 2016-2018 run there are 15-20 AMC13 cards installed in the HCAL subsystem running continuously for $\sim$9 months each year. During the 2016 run, I was responsible for all maintenance and development of the AMC13 cards installed in HCAL. The card provides clock and timing commands to the HCAL DAQ electronics, builds events from AMC modules, and propagates the status of the μTCA crate upstream. The card must handle the 40 MHz signal rate set by the Large Hadron Collider and process events at 100 KHz with event sizes ranging from 4-5 kB depending on run conditions and the HCAL region.

For HCAL each AMC13 is located in a MCH slot of a μTCA crate. μHTRs fill the 12 AMC slots of the crate and provide the event fragments to the AMC13. Additional μTCA crates with an AMC13 were needed for the 2017 run to provide clock and configuration commands to on-detector electronics but not event building. A typical crate configuration is shown in Figure 2·2.

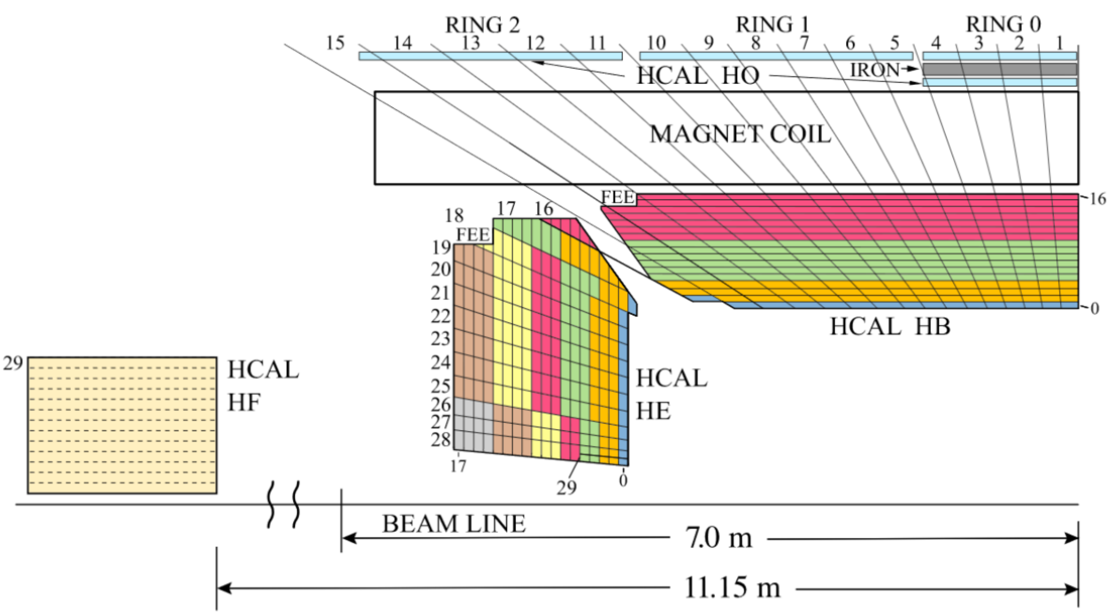

Figure 2·2: HCAL layout and segmentation in the Z-η plane.

The first job of the AMC13 is to keep the back-end in sync by distributing the LHC clock and other timing controls received by the Timing Control and Distribution System (TCDS). The clock and control signals are sent from TCDS encoded over a single data stream. The AMC13 separates the clock and control signal and distributes them over the backplane to the μHTRs. The clock frequency is measured and reported to the software for monitoring. The number of various control signals are saved in memory on the board along with a short history of the signals last received. The signal number counting is crucial for debugging where for example the number of

L1As received by the AMC13 can be compared to the μHTR to see where an event was lost.

Table 2.1: AMC13 Trigger Throttling State

Value	State	Comment
0000	Disconnected	Hardware failure or broken cable
0001	Warning overflow	Imminent buffer overflow
0010	Out of sync	FED is no more synchronized with the TTC values
0100	Busy	Cannot accept triggers
1000	Ready	Ready to accept triggers
1100	Error	Any other state that prevents correct functioning
1111	Disconnected	Hardware failure or broken cable

The trigger throttling system (TTS) relays electronic state information to the trigger system in order to throttle the rate of L1As. The AMC13 has 6 state levels given by table 2.1. If the state of the AMC13 is in Overflow the queue of events for the event builder is ∼90% full and the rate of triggers is throttled to 0 until the queue is cleared to ∼10%. Currently the μTCA system can reach a maximum of ∼250 kHz rate of events with $\sim 4kB$ event sizes. Since the Level-1 trigger has a maximum rate of 100 kHz the μTCA system rarely throttles L1As during collisions. Any throttling is a sign of an error with the μTCA electronics since they are not operating at full capability. After the EYETS HCAL will undergo extensive remapping and layers will be read out more finely in the radial direction. This adds more channels and hence larger event sizes for the μTCA system. During this time the AMC13 will be running closer to its design capabilities and the TTS system will be more vital to monitor.

In order to determine if an AMC13 performs adequately for data taking during collisions a stress test is conducted with each card. The stress test consists of checking basic functionality and running at high rates for an extended period of time. The basic functions include reading and writing to all registers, loading different FPGA firmware, and power cycling. The card is then ran at the maximum rate of ∼250 kHz determined by the μHTRs and other crates in the system. The AMC13 fails if any errors are seen with the card in ∼10 minutes of running and yields a failure rate of approximately 10%. The high rate in the stress test provides a fast way to determine the most capable and reliable cards. Since the failed cards passed the previous tests they can be used for non-critical systems such as test stands.

The μTCA crates contain 12 μHTR boards with each storing data in the pipeline from the Front End QIE cards. The μHTRs send an event from the pipeline once an L1A is received from the AMC13. The AMC13 combines the data from all 12 μHTRs into a single event fragment. This includes generating header and trailer information to identify the particular event (Event, bunch crossing, orbit numbers), providing the full event size and information about the individual μHTR data, and calculating a cyclic redundancy check on the data to catch data corruption errors later on. All of these functions are done on the Tier 1 board which houses the Kintex FPGA. The event is sent through the multi-mode fibers to a FEROL in the central data acquisition system. Currently the AMC13 has three multi-mode output modules on the front of the board and utilizes two for sending data out.

During the development of the AMC13 and when firmware updates are implemented the simplest validation is to check the output data format. This can quickly spot timing issues by looking at the event/orbit/bunch numbers, missing fragments, and data corruption. The simplified data format is shown in Figure 2·3. The header of an AMC13 event contains most relevant event timing information such as the event, orbit, and bunch number. The header also provides a way to navigate the AMC13 event with the total number of 64-bit numbers (or words). A parser was written to automate this process and provide the error checks that can be used to validate new firmware.

During the beginning of run 2 in 2015 HCAL required a data throughput of less than 10 Gbps for each μTCA crate. This meant the AMC13 could utilize one of its three fiber outputs to handle the data flow to cDAQ. The HCAL front ends

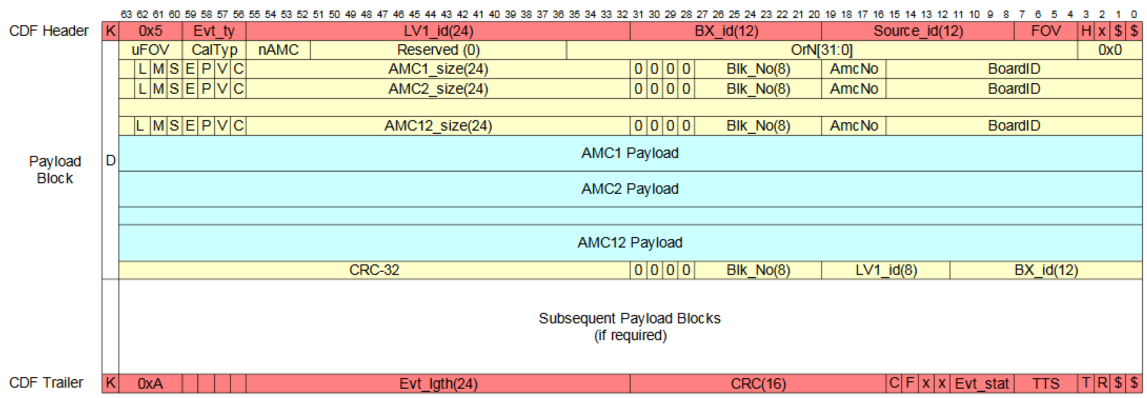

Figure 2·3: AMC13 data format with detailed header information.

were scheduled for upgrades after the 2016 run and all data rates were planned to increase due to segmentation. To handle this data rate the AMC13 would need to split the data flow through two fiber outputs, with 10 Gbps each. We commissioned this functionality in advance with the AMC13 during 2016 collisions. The data splitting functionality was already built into the AMC13 firmware but had no software support in both the AMC13 tool or the HCAL DAQ. Additionally, the extra fiber would need its own cDAQ FEROL and software support.

First, we implemented software to read out the modified event buffer. Each event was now split into two fragments with each appearing to have only half a crate active. The events needed to be merged together in the HCAL DAQ to remain compatible with all other parts of the local readout. Next, we worked with cDAQ to devise a new labeling system for the crates. Two symbolic front end driver identifications (FEDIDs), which uniquely label each DAQ crate in CMS, were created to point back to the correct physical crate. After stress tests of the system, we deployed the system for the the last month of the 2016 run and successfully recorded HCAL data with the two fiber system.

2.3.5 AMC13 Software

The AMC13 firmware run settings are determined by values in a built in flash memory. The memory can be read and written to by the CERN IPBus protocol and the AMC13 software is a high level wrapper of the IPBus software. IPBus is a hardware control protocol wrapped by IP for reliable remote control of the system.

To communicate with the AMC13 two C++ classes are used called AMC13Simple and AMC13Class. The class AMC13Simple provides base commands that can read from and write to registers on the flash memory. The FPGAs read the memory from their respective Tiers and carry out commands based on the values. For example, if a 1 is written to the first bit of memory on the Tier 1 board the card will enter Run mode where it will build events when it receives a Level 1 accept. These write commands are the building blocks of all of the controls to the AMC13.

The AMC13Class inherits all of the AMC13Simple commands and uses them to form user friendly and complex functionality. This allows for applications to the class and utilize the AMC13 board without having to know memory registers or the proper order of reads and writes.

The last element of the supported software is the AMC13Tool. The tool is an interactive session that allows for AMC13Class commands to be called directly on the command line. This type of communication is not used for collision operations but instead is a key method for testing and debugging. The tool can generate arbitrary events with varying trigger rates, active AMCs, AMC event sizes, trigger rules and more. Around 1k events can be written in the AMC13 event buffer and transferred to hard drives for event parsing. During collisions the command line tool can still be used to monitor specific cards that may be exhibiting issues.

There are two components to the AMC13 online monitoring: Event builder and Event buffer. The event builder component refers to comparing key elements of the data as they are being built by the event builder. The three most important checks are the event, orbit, and bunch crossing numbers, with many more available through the firmware. The AMC13 is able to look into the payloads received from the μHTRs and compare the values to its own internal counters. If the values do not match a register specific to the value being checked is incremented. This is done for every event accepted by the level one trigger and can be reliably measured down to one mismatch in millions of events. During collisions operations with $\sim$100 kHz L1A rate we expect the number of false positives to be less than 1 in 5×10^{10} events (or $\sim$12 hours of collisions for one fill). Since the mismatch counter is so reliable it is an immediate sign of a problem with the detector.

The second component of online monitoring, referred to here as the event buffer, has not yet been implemented to its full potential. Currently it is used during local runs as a convenient tool to record data since the usual DAQ subsystem is not used for local runs. For future runs the event buffer monitoring will offer online data quality monitoring of full HCAL events even during collisions. HCAL currently monitors only the trigger primitives online and the full event offline, so the event buffer would fill the gap online where we are blind and potentially save data. The event builder on the AMC13 works by writing the event from a crate to on board memory with a size limit of $\sim$1k events. The data can be read off at any point during running without effecting the crate or AMC13.

The event buffer uses a simple FIFO so once an event is read it can be overwritten by a new event. The events can then undergo the standard set of data quality checks done for the offline data. The read rate is limited to $\sim$100 Hz which is more than adequate to detect continuous errors and allow for intervention.

To bridge the gap between an error in the event builder system and HCAL operations is the alarmer. The program reads a table that is updated with all of the error register values on the μTCA cards and takes action corresponding to the errors. The action usually consists of changing the status of HCAL from "Running" to "Running Degraded" as well as sending out emails and text alerts with information about the errors. That status can immediately be seen in the control room and signals the shifter to call the HCAL on-call to get instructions on what actions to take.

Chapter 3

Z+jets Measurement

3.1 Data and Simulated Samples

The data sample analyzed corresponds to an integrated luminosity of $35.9\,\mathrm{fb}^{-1}$, collected in 13 TeV proton-proton collisions with the CMS detector during the 2016 data taking period. The single muon data sets, listed in 3.1, are use in this analysis. Candidate events are selected online using single muon triggers listed in 3.2, which require at least one isolated muon with $p_{\mathrm{T}} > 24\,\mathrm{GeV}$ and $|\eta| < 2.4$. The total trigger efficiency for events within the acceptance of this analysis is greater than 90%. The analysis uses CMSSW version `CMSSW_9_4_10` with the miniAOD v3 format. The Global tag and JSON file are listed below.

Data Global Tags:

- Era B-H: `94X_dataRun2_v10`

MC Global Tag:

- `94X_mcRun2_asymptotic_v3`

JSON File:

- `Cert_271036-284044_13TeV_23Sep2016ReReco_Collisions16_JSON.txt`

Simulated events for both signal and background are produced using various Monte Carlo (MC) event generators, with the CMS detector response modeled using the GEANT4 [Allison et al. (2006)] program. These events are then reconstructed using the same algorithms as used to reconstruct collision data. The normalization for the

Table 3.1: Single Muon Data Samples

Sample
/SingleMuon/Run2016B-17Jul2018_ver2-v1/MINIAOD
/SingleMuon/Run2016C-17Jul2018-v1/MINIAOD
/SingleMuon/Run2016D-17Jul2018-v1/MINIAOD
/SingleMuon/Run2016E-17Jul2018-v1/MINIAOD
/SingleMuon/Run2016F-17Jul2018-v1/MINIAOD
/SingleMuon/Run2016G-17Jul2018-v1/MINIAOD
/SingleMuon/Run2016H-17Jul2018-v1/MINIAOD

Table 3.2: Single Muon Triggers

HLT_IsoMu24
HLT_IsoTkMu24

MC samples is calculated from the integrated luminosity and the cross section for the process in the sample.

For the simulation of the signal, we use a sample generated with MADGRAPH5 aMC@NLO (shortened as MG5_aMC) [Alwall et al. (2008)] using the FxFx merging scheme [Frederix and Frixione (2012)]. Parton shower and hadronization are simulated with PYTHIA8 [Sjöstrand et al. (2008)] using the CUETP8M1 tune [CMS Collaboration (2015)]. The matrix elements include Z + 0,1,2 jets at NLO, giving a LO accuracy for Z + 3 jets.

To gain more statistics for the signal MC, a binned sample in the number of outgoing partons (npNLO) in the hard scattering is used. All signal samples and their corresponding event numbers, effective event numbers, and cross sections are shown in 3.3. The number of effective events is the sum of event weights before any offline selections. The effective number of events is smaller than the number of events because the event weights can be negative. This is a result of the the method used by MG5_aMC to compute NLO accurate cross sections. To combine the inclusive and binned samples a weight as a function of npNLO is derived from the formula:

$$\text{weight}(npNLO) = \frac{(L_{int}) * \sigma_{npNLO}}{N_{eff}} \tag{3.1}$$

where L_{int} is the integrated luminosity and N_{eff} is the number of effective events, or the sum of event weights. The calculated weights as a function of npNLO is given in table 3.4.

Table 3.3: Monte Carlo Signal Samples. Both inclusive and binned samples are combined.

MC	Events	Eff. Events	XSec (pb)
DYJetsToLL_M-50_TuneCUETP8M1_13TeV-amcatnloFXFX-pythia8	122055388	81781064	5931.9
DYToLL_0J_13TeV-amcatnloFXFX-pythia8	93832853	76690000	4620.52
DYToLL_1J_13TeV-amcatnloFXFX-pythia8	91500283	41572416	859.59
DYToLL_2J_13TeV-amcatnloFXFX-pythia8	90299356	26282782	338.26

The weighted inclusive and binned sample npNLO distributions match to within 1%. After the final event selections the inclusive and binned jet multiplicity have a trend in the ratio as seen in figure 3·1. This difference is caused by different Madgraph versions being used in the production of the samples: version (2.2 and 2.3). The difference is most significant at high multiplicity where statistical uncertainty covers the difference and we do not apply any reweighting.

Table 3.4: DY npNLO Weights

npNLO	Weight
0	1.15
1	0.57
2	0.38

The production of Z $\rightarrow \mu^+\mu^-$ + jets can be mimicked by various background sources: ($t\bar{t}$), single top, dibosons (WW, WZ, ZZ), tri-bosons (ZZZ, WWZ,WZZ), and W bosons produced in association with jets, as well as Z+jets events in which the Z boson decays into Z $\rightarrow \tau^+\tau^-$. Background processes are split into two components: the resonant and non-resonant background. The irreducible resonant background comes from events with a real Z boson in the final state (WZ, ZZ, ZVV, etc.) and it is estimated using MC samples. The non-resonant background comes from events which do not have a Z boson in the final state (such as $t\bar{t}$) and is estimated using events with both an electron and muon. The non-resonant calculation is discussed

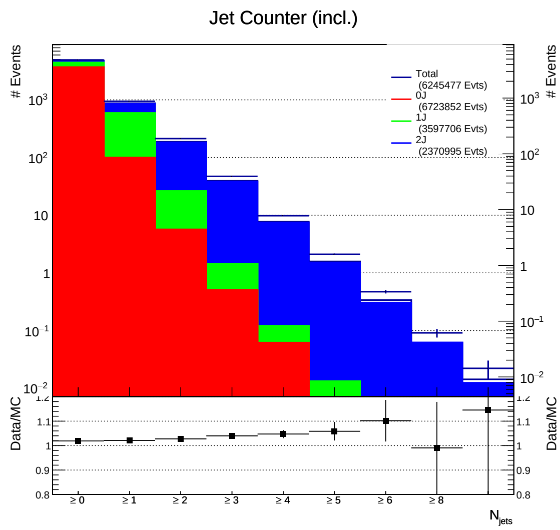

Figure 3·1: Jet multiplicity for the inclusive and binned samples. The binned samples are stacked and normalized to total cross section of the samples (5931.9fb for inclusive, 5818.37fb for binned).

further in sec.3.5. Z $\rightarrow \tau^+\tau^-$ events are considered background and are estimated using the NLO MG5_aMC signal sample.

Background samples corresponding to diboson electroweak production [Campbell et al. (2011)] are generated at NLO with POWHEG [Nason (2004); Frixione et al. (2007a); Alioli et al. (2010); Frixione et al. (2007b)] interfaced to PYTHIA 8 or MADGRAPH5_aMC@NLO interfaced to PYTHIA 8. The background sample corresponding to tribosons (ZVV) are generated at NLO using MADGRAPH5_aMC@NLO interfaced with PYTHIA 8. Multi-boson samples with their corresponding number of events and cross section are shown in 3.5.

Table 3.5: Monte Carlo Resonant Samples

MC	Events	XSec (pb)
ZZTo2L2Nu_13TeV_powheg_pythia8	57586850	0.5644
ZZTo2L2Q_13TeV_amcatnloFXFX_madspin_pythia8	15462693	3.222
ZZTo4L_13TeV_powheg_pythia8	103121112	1.256
WZTo2L2Q_13TeV_amcatnloFXFX_madspin_pythia8	26517272	5.606
WZTo3LNu_TuneCUETP8M1_13TeV-powheg-pythia8	19993200	4.430
WWZ_TuneCUETP8M1_13TeV-amcatnlo-pythia8	250000	0.1651
WZZ_TuneCUETP8M1_13TeV-amcatnlo-pythia8	246800	0.05565
ZZZ_TuneCUETP8M1_13TeV-amcatnlo-pythia8	249237	0.01398

As a cross-check for the non-resonant control region technique we include MC samples that estimate the same events. The list of samples is shown in 3.6. The closure tests are shown and discussed more in sec. 3.5.

Table 3.6: Monte Carlo Non-Resonant Samples with T* = TuneCUETP8M1.

Sample Name	Events	XSec (pb)
ST_s-channel_4f_leptonDecays_13TeV-amcatnlo-pythia8_T*	1000000	3.35
ST_t-channel_antitop_4f_inclusiveDecays_13TeV-powhegV2-madspin-pythia8_T*	38811017	136.0
ST_t-channel_top_4f_inclusiveDecays_13TeV-powhegV2-madspin-pythia8_T*	67240808	80.95
ST_tW_top_5f_inclusiveDecays_13TeV-powheg-pythia8_T*	6952830	35.6
ST_tW_antitop_5f_inclusiveDecays_13TeV-powheg-pythia8_T*	6933094	35.6
TT_TuneCUETP8M2T4_13TeV-powheg-pythia8	77081156	831.7
WJetsToLNu_TuneCUETP8M1_13TeV-amcatnloFXFX-pythia8	86916455	61526
WWTo2L2Nu_13TeV-powheg	1982372	12.21

3.2 Event Reconstruction

The global event reconstruction (also called particle-flow event reconstruction [Sirunyan et al. (2017)]) aims to reconstruct and identify each individual particle in an event, with an optimized combination of all sub-detector information. In this process, the identification of the particle type (photon, electron, muon, charged hadron, neutral hadron) plays an important role in the determination of the particle direction and energy.

The reconstructed vertex with the largest value of summed physics-object p_{T}^2 is taken to be the primary pp interaction vertex. The physics objects include the jets, clustered using the jet finding algorithm [Cacciari et al. (2008, 2012)] with the tracks assigned to the vertex as inputs, and the associated missing transverse momentum, taken as the negative vector sum of the p_{T} of those jets.

Electron candidates are reconstructed by combining the information from the ECAL and from the silicon tracker. The energy of electrons is determined from a combination of the electron momentum at the primary interaction vertex as determined by the tracker, the energy of the corresponding ECAL cluster, and the energy sum of all bremsstrahlung photons spatially compatible with originating from the electron track. The Super Cluster (SC) reconstruction efficiency for $E_T^{SC} > 5\,\mathrm{GeV}$ is close to 100%. The momentum resolution for electrons with $p_{\mathrm{T}} \approx 45\,\mathrm{GeV}$ from $\mathrm{Z}(\rightarrow e^{+}e^{-})$ decays ranges from 1.7% to 4.5%. It is generally better in the barrel region than in the endcaps, and depends on the bremsstrahlung energy emitted by the electron, as it traverses the material in front of the ECAL [Khachatryan et al. (2015c)]. To reduce the electron misidentification rate, electron candidates are subjected to additional identification criteria, which are based on the distribution of the electromagnetic shower in the ECAL, a matching of the trajectory of an electron track with the cluster in the ECAL, and its consistency with originating from the selected primary vertex.

Jets are formed from the particles reconstructed by the PF algorithm, using the FAST-JET software package and the anti-k_{T} jet clustering algorithm [Cacciari et al. (2008)] with a distance parameter of 0.4. The jet four-momentum is obtained according to the E-scheme (vector sum of the four-momenta of the constituents). The technique of charged-hadron subtraction (CHS) [Collaboration (2014)] is used to reduce the pileup contribution by removing charged particles that originate from pileup vertices. The jet four-momentum is corrected for the difference observed in the simulation between jets built from PF candidates and generator-level particles. The jet mass and direction are kept constant for the corrections. An offset correction is applied to jet energies to take into account the contribution from additional proton-proton interactions within the same or nearby bunch crossings. Further jet energy corrections are applied for differences between data and simulation in the pileup in zero-bias events and in the p_{T} balance in dijet, $\mathrm{Z}+$ jet, and $\gamma+$ jet events.

To maximize the reconstruction efficiency while reducing the instrumental background and contamination from pileup jets, tight identification quality criteria are applied on jets, based on the energy fraction carried by charged and neutral hadrons, as well as charged leptons and photons. A minimum threshold of 30 GeV on the p_{T} of jets is required to ensure that they are well measured and to reduce the pileup contamination. Jets are required to have $|\eta| < 2.4$ and to be separated from all selected lepton candidates by at least $R \leq 0.4$.

3.2.1 Muons Reconstruction

Muon candidates are reconstructed with a global track fit, the combinatorial Kalman filter method [Adam et al. (2005)], using both the inner tracking system and the muon spectrometer [Chatrchyan et al. (2012c)]. The momentum of the muons is obtained from the curvature of the corresponding track. Two unique techniques are used to increase the efficiency over a wide range in muon momentum: global and tracker muons. The global muons starts first with a fit done with the hits in the DTs, CSCs, and RPCs of the muon spectrometer to form a standalone muon. If a tracker track is matched to the standalone muon it is promoted to a global muon. The efficiency of the global muon algorithm is higher than 95% for muons with $p_{\mathrm{T}} > 20$ GeV. The relative p_{T} resolution at 100 GeV is 2% in the barrel and 6% in the endcap and increases to 10% in the endcap at 1 TeV.

The tracker muon starts instead in the tracker, where all tracker tracks with $p_{\mathrm{T}} > 0.5$ GeV or $p > 2$ GeV are considered as muons. The tracks are then extrapolated to the muon system taking into account the interaction with the detector medium. If a hit in a DT or CSC is within 3 cm or 4σ of the muon track (in the local coordinate system of the muon chamber) the track is considered a tracker muon. No fit is done for the combined tracker track and muon system hits so the tracker muon p_{T} is calculated from the tracker track curvature. The efficiency at low muon p_{T} is greater than global muons because of the low p_{T} seeds and the requirement of only one hit in the muon system.

3.3 Sample Corrections

3.3.1 Rochester Correction

To correct misalignment of the CMS detector in both data and MC the Rochester corrections are applied. This provides corrections as a function of muon charge, p_{T}, and η. The corrections check for discrepancies in the invariant mass of the muon pair in different regions (η and ϕ) of the detector and different charge.

3.3.2 Muon Scale Factors

To calculate the cross section of Z boson production we must approximate the efficiency of the detector and account for missed Z decays. Within the fiducial region of CMS there are many ways to miss a muon including inactive material, measurement noise, and limits on fitting algorithms. Many of these efficiencies could be increased to improve acceptance but would come at the cost of mistaking other objects as muons or picking up cosmic muons. The efficiencies of each step in the measurement process can be approximated by the Tag and Probe (T&P) method [Chatrchyan et al. (2011)].

T&P uses a high quality muon as a "tag" and picks other muons, called "probes", in the same event that result in an invariant mass of $\pm 20\,\mathrm{GeV}$ from the Z mass. The "tag" muons have strict quality cuts on the track fit, are required to be within the barrel, and have $p_{\mathrm{T}} > 30\,\mathrm{GeV}$. This sample of probes is then put through any selection criteria being measured including reconstruction, identification, isolation, or triggering. The ratio of probes that pass the selection to the total number of probes is estimated to be the efficiency. This method of measuring the efficiency assumes muons only from Z boson decays so a background subtraction is applied before the final count of passing and total probes is measured. The total passing and failing mass spectra are fit using a convolution of a function that looks like the signal (typically Breight-Wigner) and one that looks like the background (e.g. exponential) as shown in Figure 3·2. The area of the signal function alone is then the number of muons from Z decays.

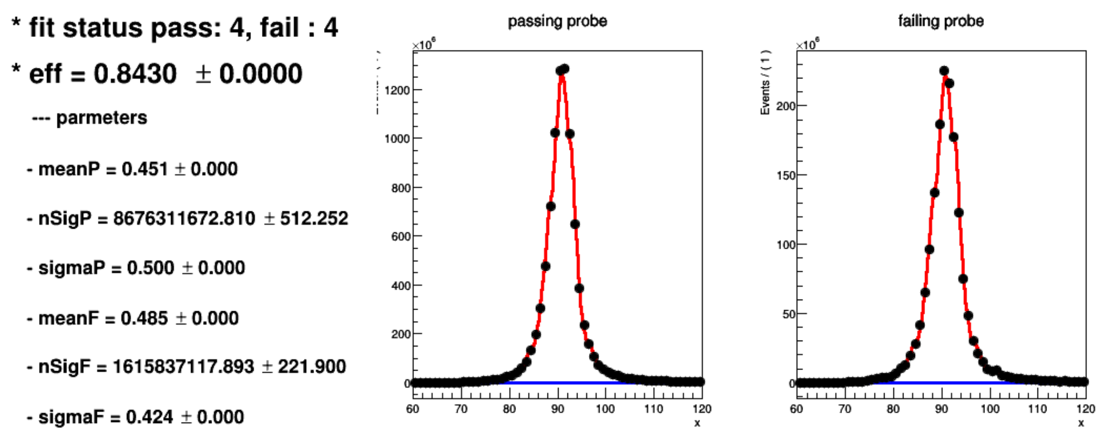

Figure 3·2: Example of Tag and Probe fit for passing and failing probes in $0.0 < \eta < 0.8$ and $40 < p_{\mathrm{T}} < 50\,\mathrm{GeV}$. The trigger efficiency is measured as 84%. The various fit parameters are also shown.

The efficiencies are calculated as a function of muon p_{T} and η using the same binning scheme as the main analysis. At the reconstruction level the MC is weighted so the efficiency matches data by use of scale factors (SF). The SFs are simply the ratio of the data and MC efficiency for each p_{T}, η bin. Once the data is unfolded it is divided by the efficiency to produce a cross section measurement. The efficiency measurements of data and MC for the single muon trigger is shown in fig. 3·3. The SFs are shown in the same figure in the ratio plot (Data/MC). Above the p_{T} cut of 30 GeV the SFs stabilize around 0.9. The ID and isolation SFs are provided by the CMS Muon Physics Object Group (POG) and the trigger SFs are calculated from Muon POG T&P Software.

3.3.3 Pileup

Pileup scale factors are applied to the MC events to account for the difference in pileup profiles between data and MC. This is done with the data pileup estimated

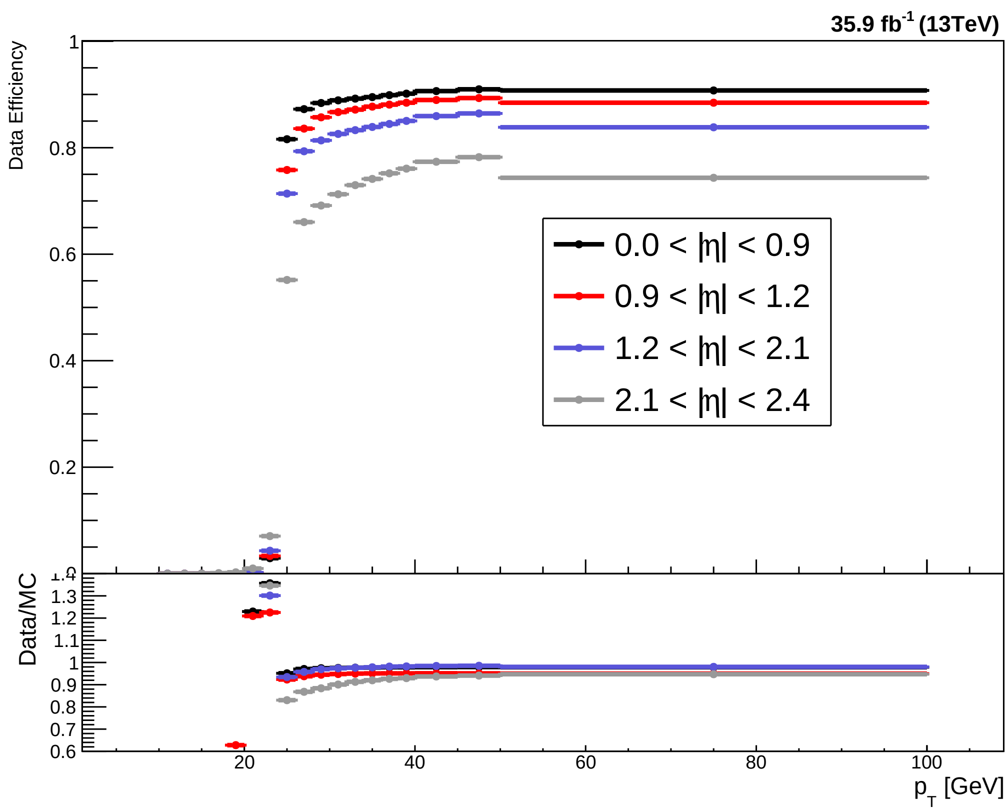

Figure 3·3: Data efficiencies for single muon triggers (HLT_IsoMu24 or HLT_IsoTkMu24). The turn on is smeared around 24 GeV because of differences in the online and offline reconstruction. The measurement is broken up into 18 p_{T} bins and 4 η bins.

from the CMS Beam Radiation Instrumentation and Luminosity Project (BRIL) with eras B-H and the MC pileup profile used to generate the events. A value of 69.2 mb is used for the minimum bias cross section in the calculation. As a check on the pile up reweighting figure 3·4 shows the comparison of the number of vertices in data and MC. The minimum bias is then varied with its 4.6% uncertainty to obtain a different data pileup profile and compared again to MC in figure 3·4.

The number of vertices without pile re-weighting is shown in figure 3·4. To look at the effect of highly ionizing particles (HIP) in the tracker, Figure 3·5 shows the number of vertices in eras B-F and G-H. The HIPs lowered the efficiency of track reconstructure and subsequently mismeasured the number of vertices in a collision. This problem was mitigated in G and H eras.

3.3.4 L1 Prefire Weights

Due to a timing drift of the ECAL with respect to the calorimeter trigger primitives (TP), high eta TPs could be assigned to the previous bunch crossing BX-1 (BX negative 1) instead of BX0. A TP corresponding to the BX0 would then not be able to generate a level 1 accept (L1A) because of the CMS trigger rules. The BX-1 TP event will most likely be a minimum bias event and get rejected at the high level trigger. These missing events are not simulated in the MC and the MC must be corrected using weights.

The event weights are calculated using the p_{T} and η of all photons and jets in an event and generate a probability for the event to be lost due to prefiring. The weight is applied to each MC event in the analysis. For the full analysis selection the average of the prefiring weights is 0.98.

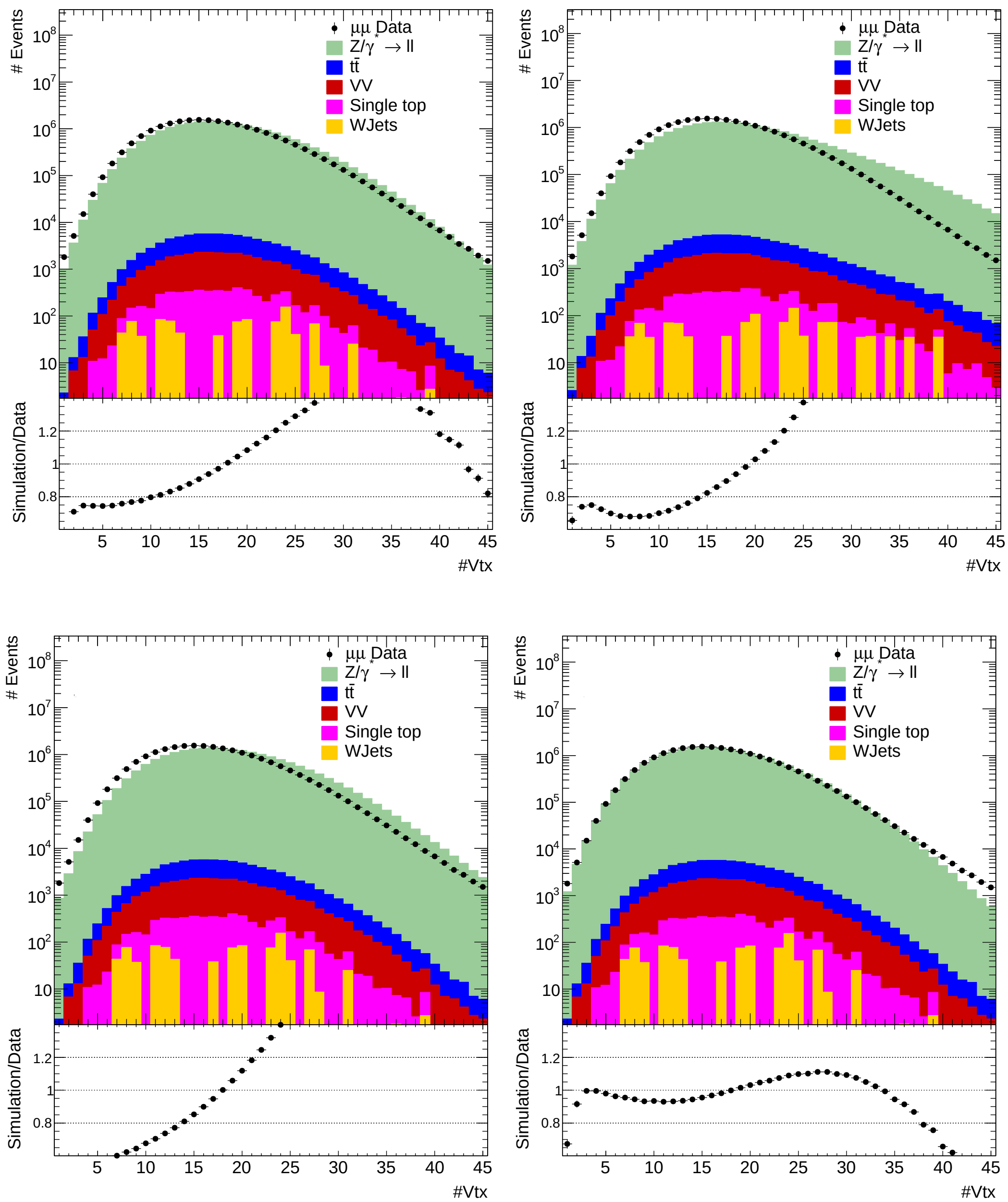

Figure 3·4: Number of vertices in data and MC. Minimum bias of 69.2 mb (top left) is used for the data profile. Minimum Bias of 69.2 mb varied 4.6% up (bottom left) and down (bottom right). Number of vertices in data and MC without re-weighting the MC (top right).

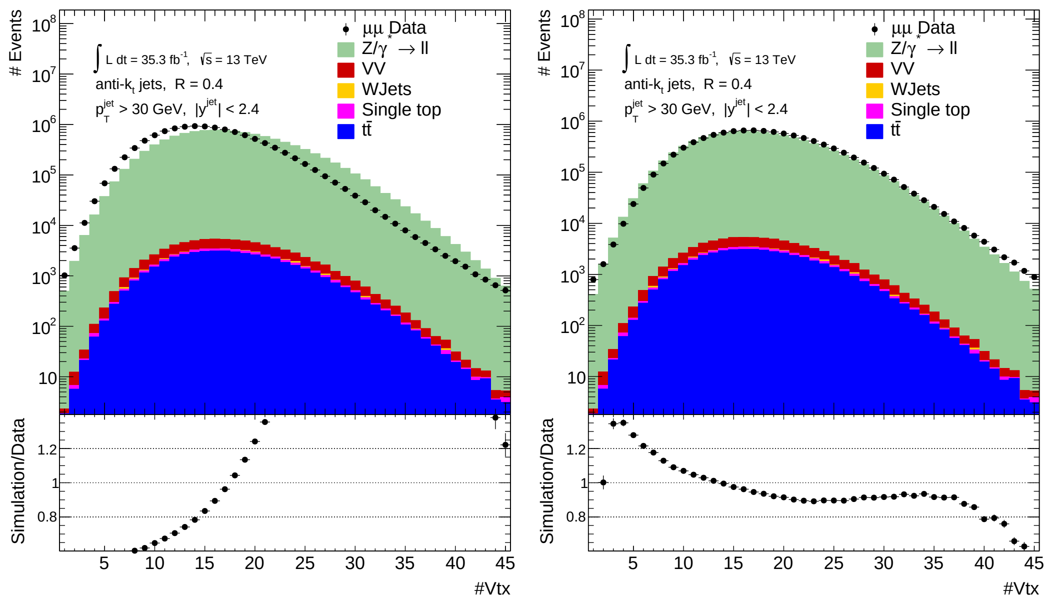

Figure 3·5: Number of vertices in era B-F (Left) and G-H (Right). Minimum bias of 69.2 mb is used to calculate the profile. A large discrepancy is seen in the earlier B-F eras because of the problem of highly ionizing particles (HIP).

3.4 Object Selections

3.4.1 Muon Selection

The main goal when choosing cuts for the muons is to select as many Z events as possible. Selecting muon only around the Z peak enhances the DY cross section significantly over all background sources so signal to background is not as much of a concern. Two muons are required with opposite sign and an invariant mass of $71.0 < M_{\mu\mu} < 111.0\,\text{GeV}$. The edge of the mass window is chosen so the signal to background stays above 10:1. Only the two highest p_{T} muons that pass the muon selection criteria are considered for the Z boson candidate.

Muon Identification: The Medium muon ID is used in this analysis. Medium ID selects either global or tracker muon and adds track-quality and muon-quality requirements such as a track χ^2 cut. The Medium ID provides at least 95% efficiency but still rejects over 90% of fake muons from jets.

Muon Isolation: The final decay products of the Z decay are typically well separated so large energy deposits around a muon track signify the muon is fake or a decay from a jet. Both of these cases can be vetoed using isolation defined as:

$$I_{\mu} = \frac{\sum p_{\text{T}}(CH) + max(0, \sum E_T(NH) + \sum E_T(\gamma) - \frac{1}{2}\sum p_{\text{T}}(PU))}{p_{\text{T}}(\mu)} \tag{3.2}$$

where CH is charged hadron and NH is neutral hadron. The sums are over all particles within $\Delta R < 0.4$ of the muon and only particles from the primary vertex are used except for the pileup term. I_{μ} provides a measure of the momentum around the muon compared to the muon p_{T}. A value of 0.15, or 15% the muon p_{T}, is chosen to veto fakes and achieve 95% efficiency.

Muon Transverse Momentum: Ideally we would collect muons down to the $\sim$ 1.6 GeV momentum limit of CMS, but we are limited by the online trigger of 24 GeV. This cut will miss decays in high η since most muons will have 45 GeV momentum and $\eta = 2.4$ corresponds to p_{T} less than 20 GeV. The online and offline reconstruction use slightly different algorithms due to time constraints so the edge of the trigger is blurred offline. To avoid mis-modeling this effect in MC, we choose a cut above the turn on curve at $p_{\mathrm{T}} = 30$ GeV.

Muon η: We use the full coverage of the muon spectrometer which extends out to $\eta = 2.4$.

3.4.2 Jet Selections

First, any jets within $\Delta R = 0.4$ of the two leading muons are discarded from the jet collection. This eliminate jets in the collection that are clustered from the energy deposits of the muons in the calorimeter. Cuts concerning the jet composition are applied in order to avoid mis-identification of pileup and to increase noise rejection. This list of cuts (see table 3.7) constitutes the Loose identification criterion provided by the JetMET POG. To reduce pileup jets, an MVA discriminator is used with working points from the JetMET POG. The working points are MVA cuts as a function of jet η and the loose working point is used for this analysis.

Table 3.7: Loose Jet ID Parameters

Neutral Hadron Fraction	< 0.99
Neutral EM Fraction	< 0.99
Number of Constituents	> 1
Charged Hadron Fraction	> 0
Charged Multiplicity	> 0
Charged EM Fraction	< 0.99

Reconstructed (RECO) jets in MC have their transverse momenta smeared in order to more closely match what is observed in data. Smearing is done according to the formula given by the JetMET group. If a RECO level jet is found to have a generator (referred to as GEN here, also called truth) level jet match, the RECO jet p_{T} is pushed away from the truth jet value by a factor given by:

$$c_{JER} = 1 + (s_{JER} - 1)\frac{p_T^{RECO} - p_T^{GEN}}{p_T^{RECO}} \tag{3.3}$$

where s_{JER} is the data-MC jet resolution scale factor dependent on the jet η and p_{T}. p_T^{RECO} is the jet transverse momentum at RECO level. p_T^{GEN} is the jet transverse momentum at GEN level. The final smeared p_T is the given by:

$$p_T^{smeared} = p_{\mathrm{T}} \times c_{JER} \tag{3.4}$$

The criteria for a RECO-GEN match is as follows:

$$\Delta R < \frac{R_{cone}}{2} \qquad |p_T^{RECO} - p_T^{GEN}| < 3 \times \sigma_{JER} \times p_{\mathrm{T}} \tag{3.5}$$

where ΔR is the angular separation between the RECO and GEN jet, R_{cone} is the cone size for the jets clustering algorithm: $R = 0.4$. p_T^{RECO} and p_T^{GEN} are defined previously. σ_{JER} is the relative p_{T} resolution in MC.

If a match is not found for the RECO jet, a Gaussian smearing is done which pushes the jet p_{T} in a random direction an amount dependent on the resolution.

$$c_{JER} = 1 + Gauss(0, \sigma_{JER})\sqrt{max(s_{JER}^2 - 1, 0)} \tag{3.6}$$

where all values have been defined previously. Lastly, if a match is found and the scale factor s_{JER} is less than 1.0 no smearing is done. An uncertainty for this technique is discussed in the systematics section.

A cut of 30 GeV on jet p_{T} is applied to reduce the pileup contamination as well as large uncertainty on the energy measurement. To ensure a good quality of the tracking information, jets with $|\eta| < 2.4$ are removed from the collection. Finally, the jet collection is ordered by decreasing p_{T} values.

3.4.3 Particle Level Objects

The particle, or GEN, level objects are accessed only for the MC samples and are used to extract the differential cross section in the MC. In unfolding, the GEN level objects are also used to determine the smearing function of the CMS detector. This process is described in section 3.8.

The GEN objects are defined to be particles with a lifetime of >1 cm (excluding neutrinos) and identified using the same algorithms as for the data. In addition, muons are dressed by adding the momenta of all photons within $\Delta R < 0.1$ from their directions to account for final state radiation. The momenta of the leading GEN muons are summed to obtain the GEN Z momentum. The GEN muons are required to pass the same kinematic selections as at detector level.

GEN jets are clustered from stable particles using the same anti-kT algorithm used for jet reconstruction. Prior to clustering neutrinos are removed and photons from final state radiation in a cone of R=0.4 are added. The kinematic cuts applied are the same as the RECO level selections. The jets are then ordered by p_{T}.

3.5 Background Estimation

Background events are split into two categories: resonant and non-resonant. The resonant background, which consists mainly of multi-boson events with at least one Z boson in the final state, are estimated using MC samples. The non-resonant events contain two leptons primarily from W decays, such as $t\bar{t}$, and are estimated from a data-driven method. The Z $\rightarrow \tau^+\tau^-$ is considered a background and is estimated from the MG5_aMC signal MC sample.

The data driven method for the non-resonant background uses a control region containing events with one electron and muon ($e^{\pm}\mu^{\mp}$) passing all other signal region criteria. The control region is then used to estimate the non-resonant background in the signal region by applying a conversion factor to account for cross section and lepton efficiency differences. Assuming lepton flavor symmetry, the cross section for a $e^{\pm}\mu^{\mp}$ final state and a $\mu^{+}\mu^{-}$ final state differs only by a factor of 2. The efficiency ratio between muons and electrons is estimated using the total yields of the two channels:

$$k_{e\mu} = \frac{\sqrt{N_{\mu\mu}}}{\sqrt{N_{ee}}} = \frac{\epsilon_{\mu}}{\epsilon_{e}} \approx 1.3 \tag{3.7}$$

where $N_{\ell\ell}$ are the number of events in the $\mathrm{Z} \rightarrow \ell\ell$ channel signal region. Resonant, signal, and background events are estimated in the control region by the signal region MC and subtracted to avoid double counting.

Combining the two we can estimate the number of non-resonant events in $\mu\mu$ from $e^{\pm}\mu^{\pm}$:

$$N_{\mu\mu} = \frac{1}{2} N_{e\mu} k_{e\mu} \tag{3.8}$$

As a closure test for this background estimation method we use MC samples including $t\bar{t}$, WW, single top, and W+Jets listed in Table 3.5. In figures 3·6-3·12 the MC samples are compared to the data-driven method for the jet and Z kinematics and differ by 5%-10%. The MC in the jet multiplicity plot (figure 3·7) deviates from data especially at higher multiplicities. In previous analyses scale factors applied to the MC would correct for this difference.

Data and simulation of muon variables and reconstructed Z boson are shown in Figures 3·13 - 3·14. Overall the agreement is very good and lower than 5% in most distributions. The Z boson p_{T} with 0 or 1 jet inclusive shows deviations that will be discussed in section 3.11.

The jet multiplicity, kinematics of the jets, dijet mass, and total hadronic p_{T} are shown in Figures 3·15 - 3·18. The $\Delta\phi$ distributions are shown in Figure 3·19.

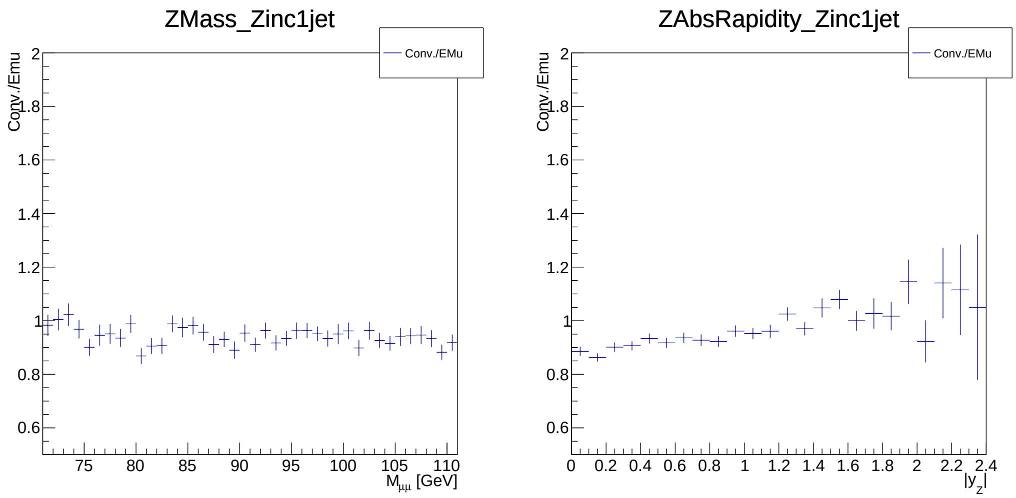

Figure 3·6: Comparison of two background estimation methods: MC samples only (Conv.) and data-driven method (EMu). Dimuon mass and Z candidate $|y|$ with one jet inclusive.

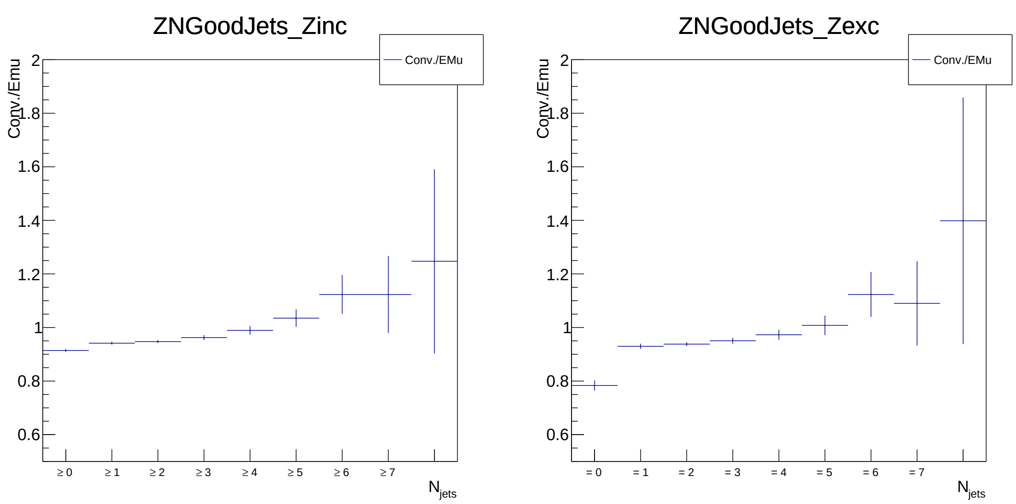

Figure 3·7: Comparison of two background estimation methods: MC samples only (Conv.) and data-driven method (EMu). Jet multiplicity inclusive and exclusive.

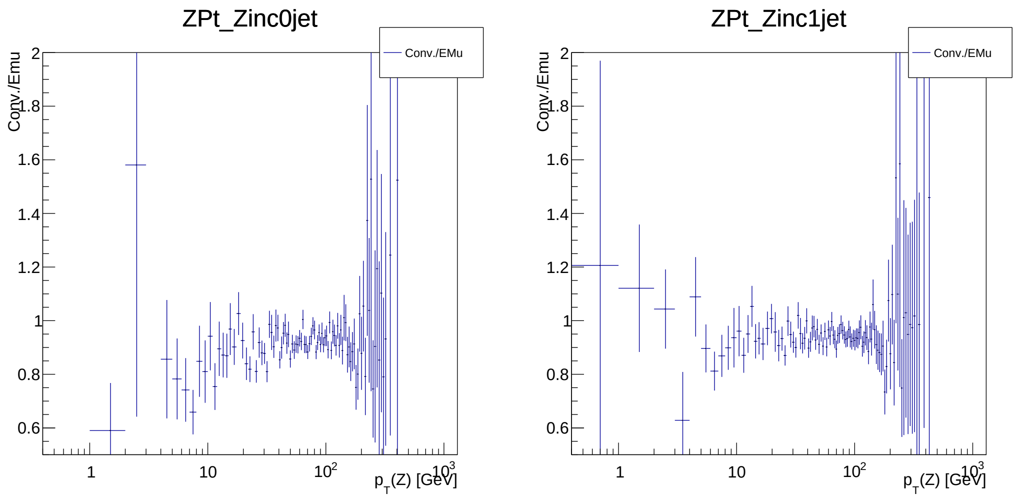

Figure 3·8: Comparison of two background estimation methods: MC samples only (Conv.) and data-driven method (EMu). Z candidate p_T 0 and 1 jets inclusive.

The number of background events is small compared to the signal and it amounts to approximately 1% for ≥0 jets and increases to 10% at 5 or more jets. For transverse momentum variables, the background increases from 1% below 100 GeV to 10% in the high-p_{T} tails. Agreement is better than 10% in all jet observables except for the parton shower region of the jet multiplicity (above 4 jets).

3.6 Observables

In this paper, the cross sections are presented as functions of several kinematic and angular observables to characterize the production mechanisms of $\mathrm{Z} \rightarrow \mu^+\mu^- +$ jets events.

The differential cross section is measured as functions of the exclusive and inclusive jet multiplicities for a total number of up to eight jets in the final state, of the jet kinematic variables including jet p_{T}, the jet rapidity (y) and the scalar sum of the jet transverse momenta (H_{T}) for $N_{jets} \geq 1, 2, 3, 4, 5$.

The $p_{\mathrm{T}}(Z)$ measurement is important for test of QCD predictions. The high p_{T}

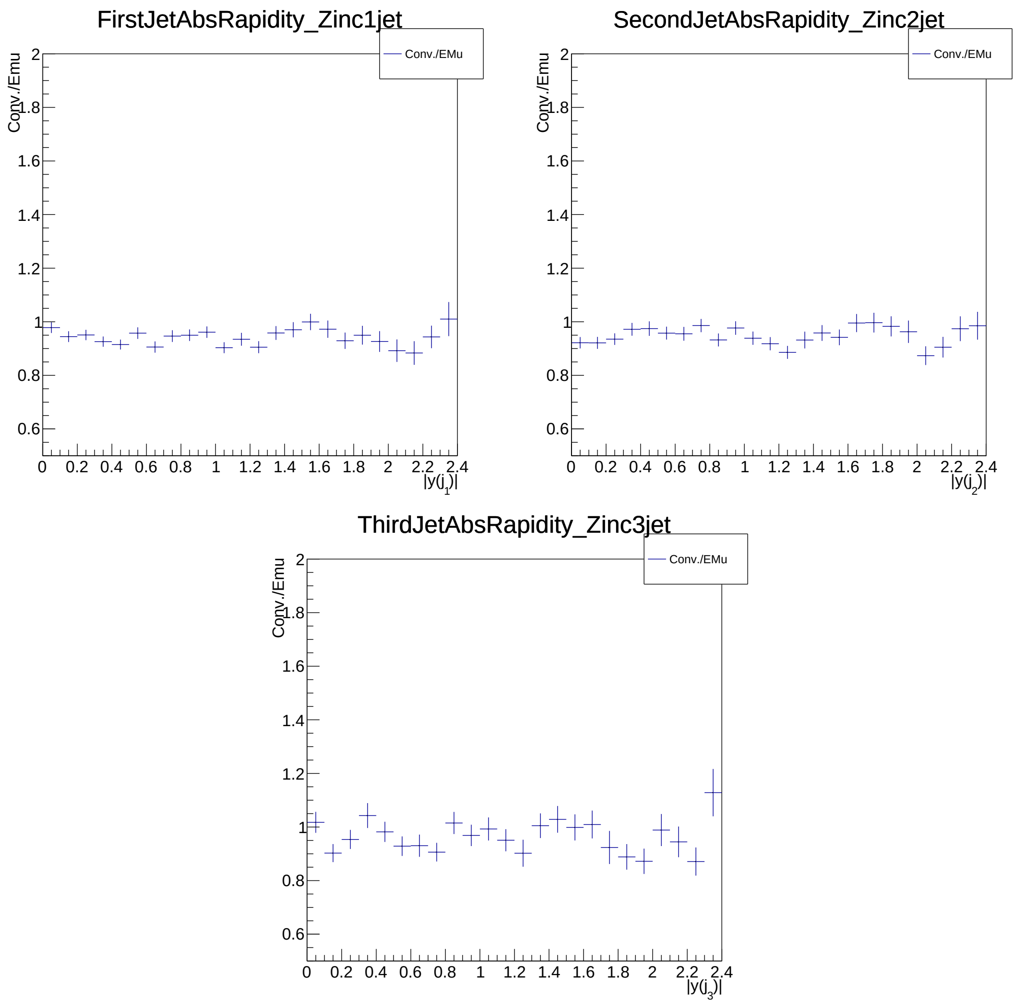

Figure 3·9: Comparison of two background estimation methods: MC samples only (Conv.) and data-driven method (EMu). First, second, and third jet absolute rapidity.

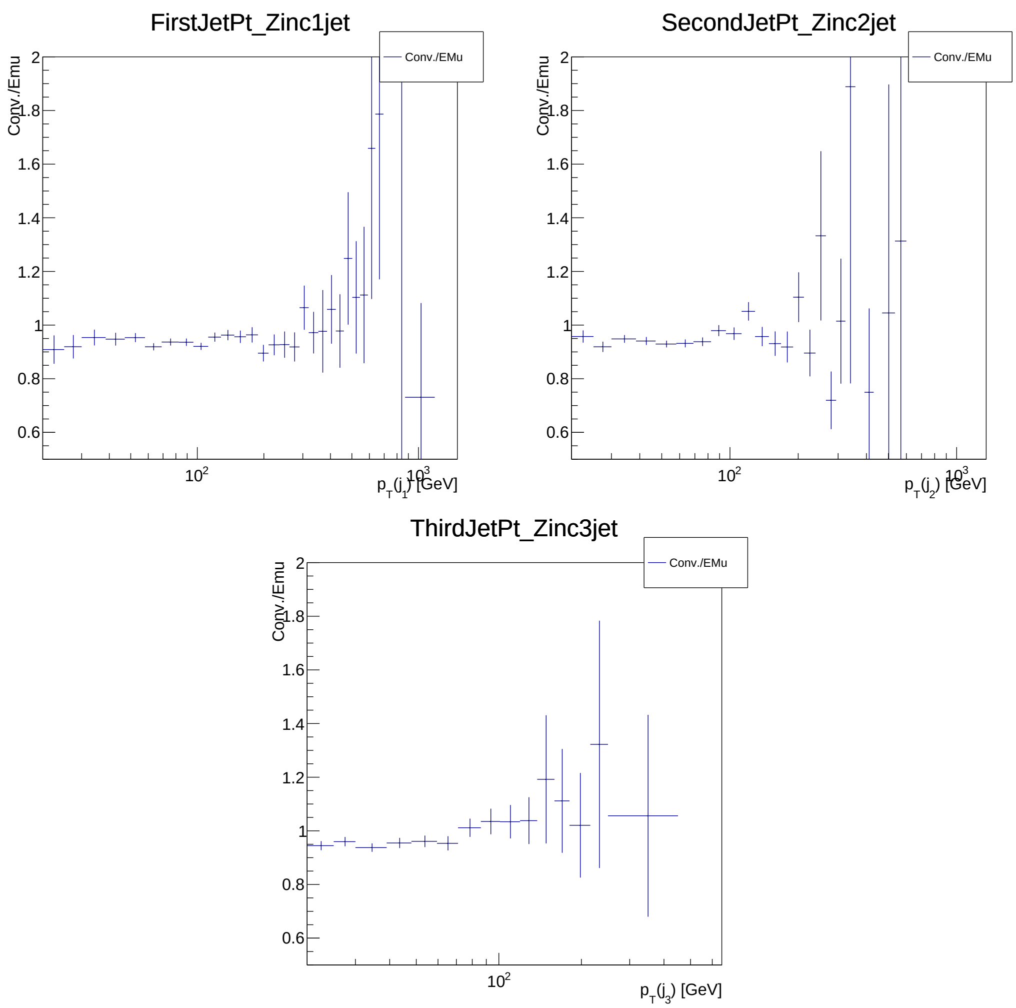

Figure 3·10: Comparison of two background estimation methods: MC samples only (Conv.) and data-driven method (EMu). First, second, and third jet p_T.

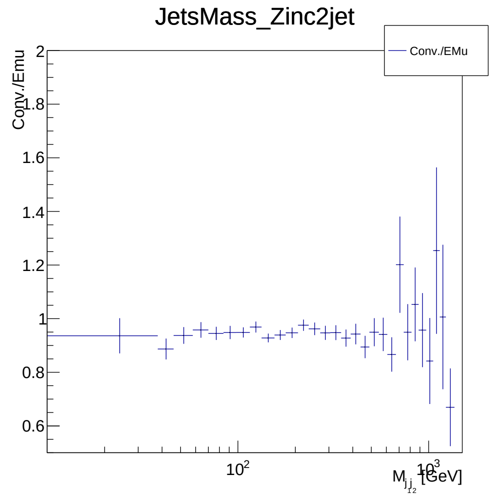

Figure 3·11: Comparison of two background estimation methods: MC samples only (Conv.) and data-driven method (EMu). Invariant mass of leading and subleading jet.

region of the $p_{\mathrm{T}}(Z)$ spectrum is affected by pQCD corrections, while non-perturbative corrections modify the low p_{T} region, so that $p_{\mathrm{T}}(Z)$ can be described through fixed-order calculations in pQCD. It is sensitive to the gluon and the light-quark PDFs in the not-so-well constrained intermediate (Bjorken-x) region. On the other hand the $p_{\mathrm{T}}(Z)$ measurement is also sensitive to soft QCD radiation (at small p_{T}).

The rapidity (y) of Z boson ($y(Z)$) is related to the momentum fraction (x) carried by the parton in the forward-going (backward-going) proton. Therefore, the y distribution directly reflects the PDFs of the interacting partons. At the LHC, the $y(Z)$ distribution is expected to be symmetric around zero, therefore the appropriate measurement is the distribution of Z bosons as a function of the $|y|$.

The jet kinematic variables, H_{T}, and the dijet mass are sensitive to the hard scattering process. The comparison of these variable to predictions will highlight the effects of including various orders in pQCD on the hard scattering cross section.

In terms of angular correlations between jets, cross sections are measured as a function of the difference in $\Delta y(j_i,j_k)$, and of the difference in azimuthal angle $\Delta\phi(j_i,j_k)$,

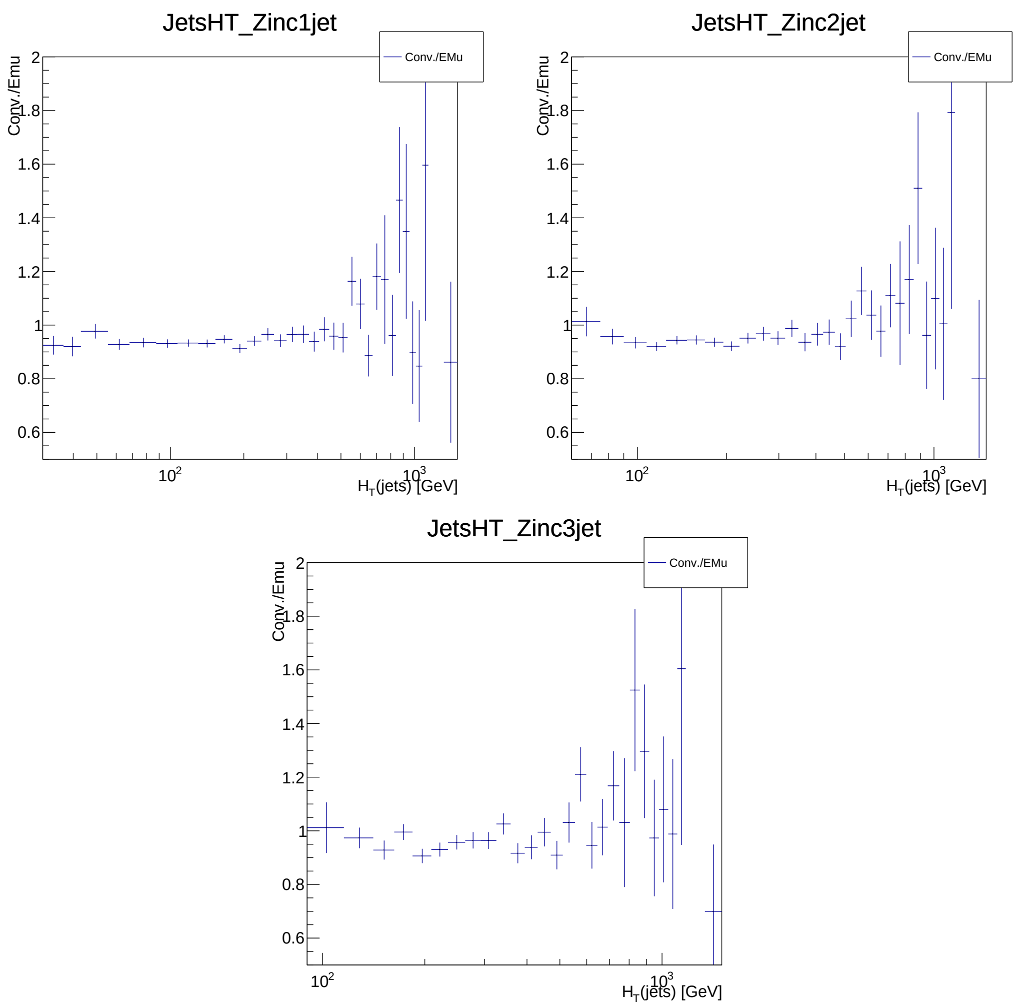

Figure 3·12: Comparison of two background estimation methods: MC samples only (Conv.) and data-driven method (EMu). Total hadronic p_T one, two, and three jets inclusive.

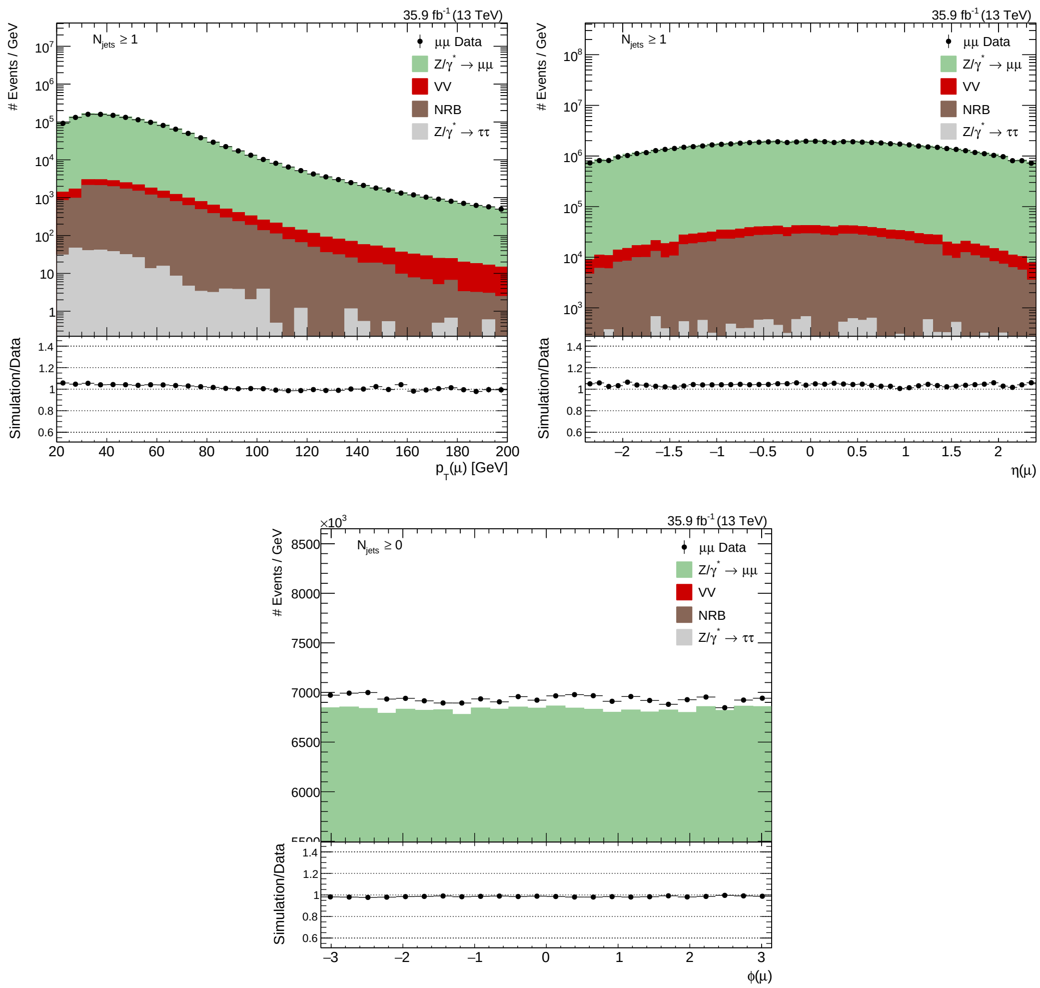

Figure 3·13: Lepton p_T (left), η (center), ϕ (right) with one jet inclusive.

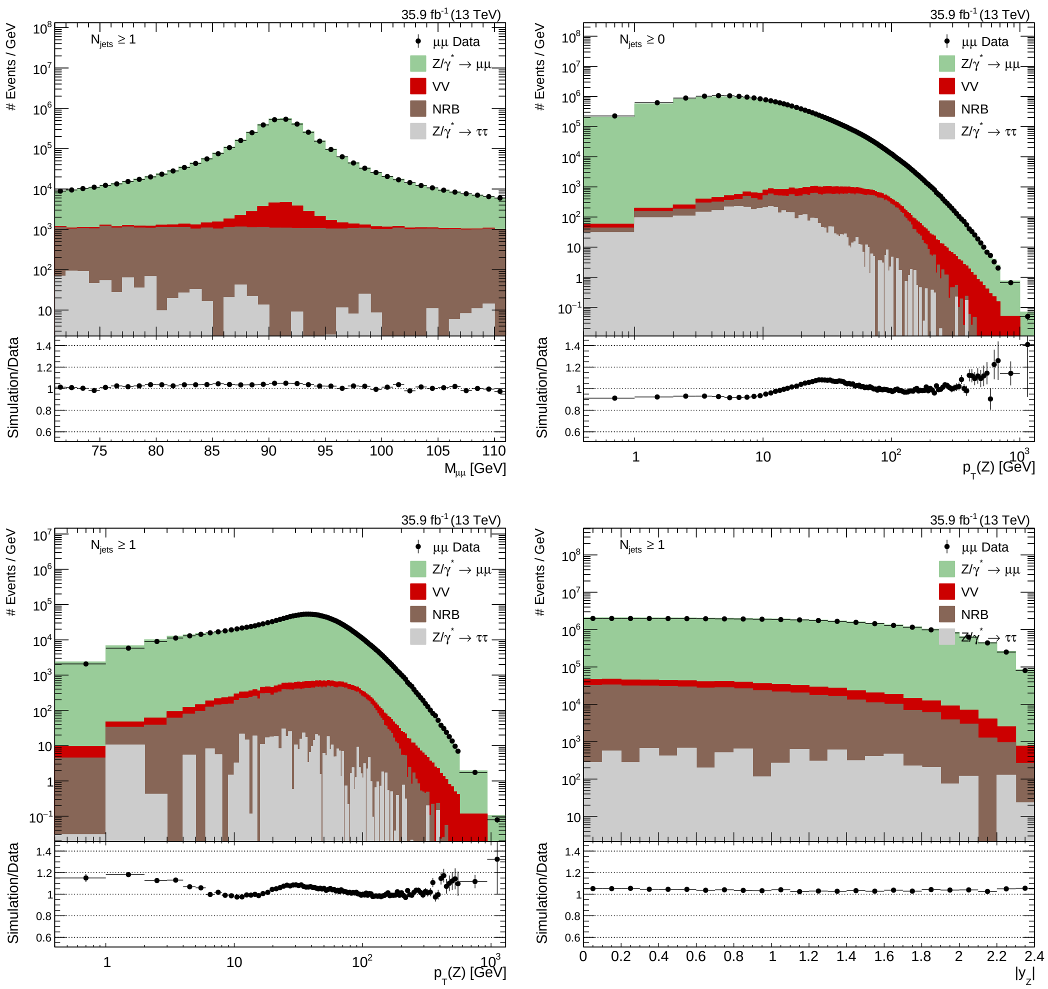

Figure 3·14: Z candidate p_T (upper) and $|y|$ (lower) with at least zero jets (left) and at least one jet (right). The background is estimated from both simulation and data driven methods describe in section 3.5. The ratio shows the combined statistical uncertainty of the data and total simulation.

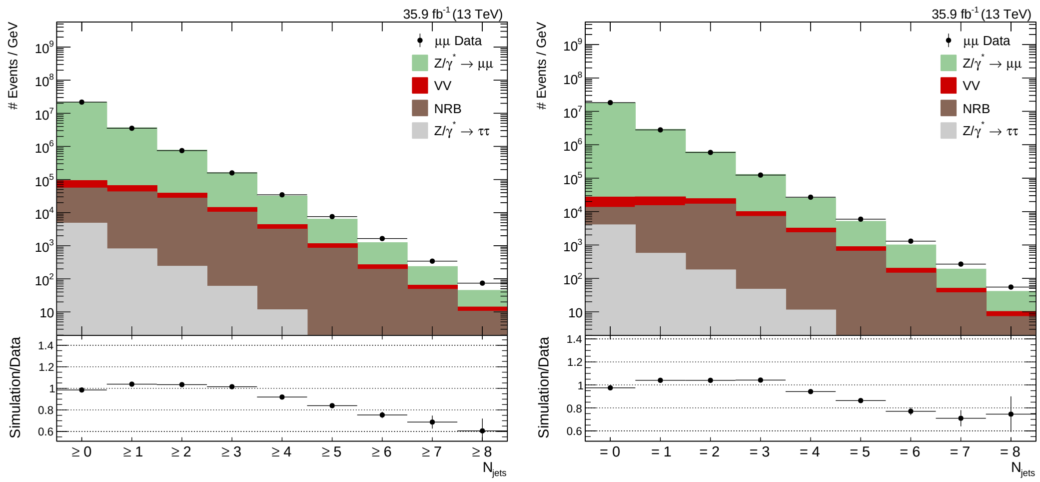

Figure 3·15: Inclusive (left) and exclusive (right) jet multiplicity. The background is estimated from both simulation and data driven methods describe in section 3.5. The ratio shows the combined statistical uncertainty of the data and total simulation.

between the i^{th} and k^{th} jets from the p_{T}-ordered list of jets in the event. From the point of angular correlations between Z boson and jets, cross sections are measured as a function of the difference in $\Delta y(Z,j_k)$, and of the difference in azimuthal angle $\Delta\phi(Z,j_k)$, between the i^{th} and k^{th} jets from the p_{T}-ordered list of jets in the event. The azimuthal angle separation $(\Delta\phi)$ between the final state Z boson and jet is sensitive to the soft gluon radiation. The advantage of studying the ϕ distribution is that it only depends on the directions of the final state Z boson and jet.

Lastly, double differential cross sections are measured as functions of leading jet p_{T} and y, leading jet and $y(Z)$, $p_{\mathrm{T}}(Z)$ and y. With larger datasets, we are able to probe finer regions of phase space with small statistical uncertainty. When splitting the p_{T} distributions in y we are able to observe any difference as a function of the scattering angle of the Z and jets.

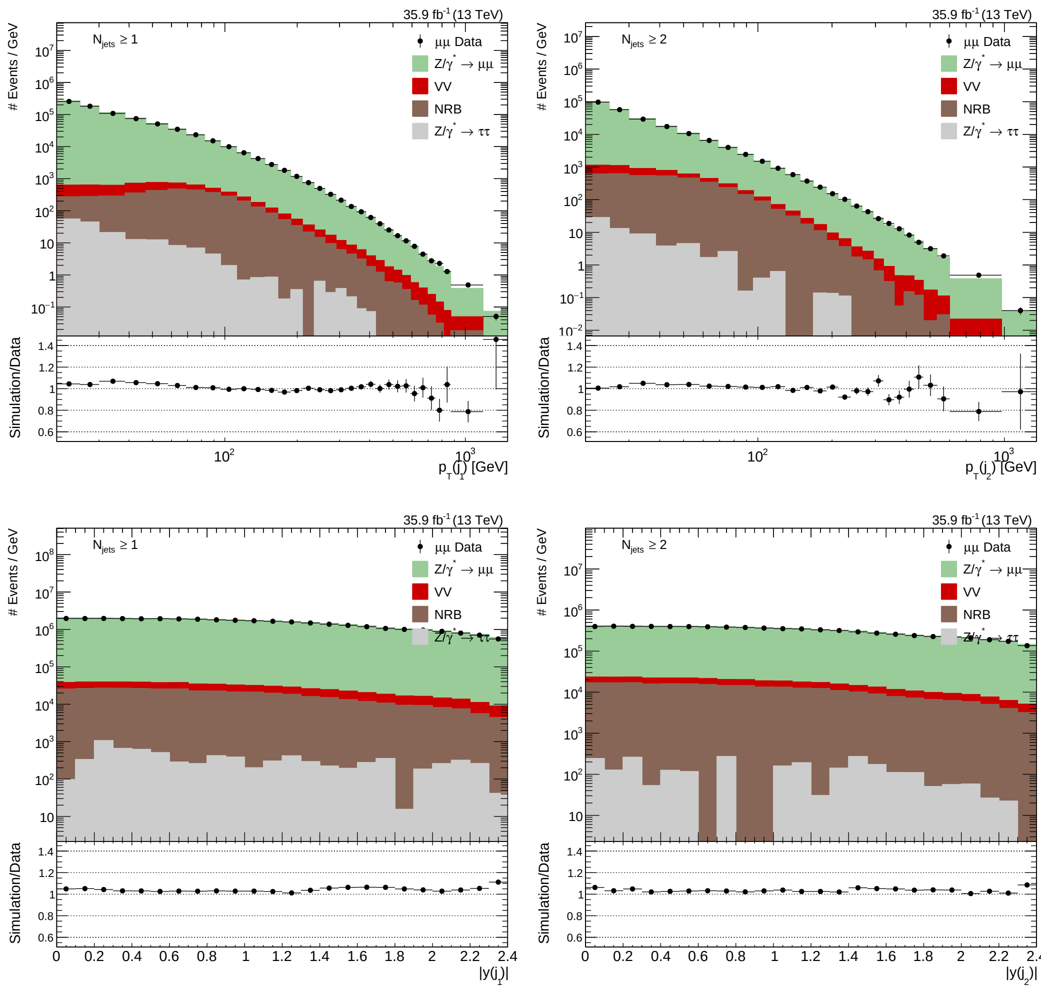

Figure 3·16: Jet p_T (upper) and $|y|$ (lower) for the leading jet (left) and sub-leading jet (right). The background is estimated from both simulation and data driven methods describe in section 3.5. The ratio shows the combined statistical uncertainty of the data and total simulation.

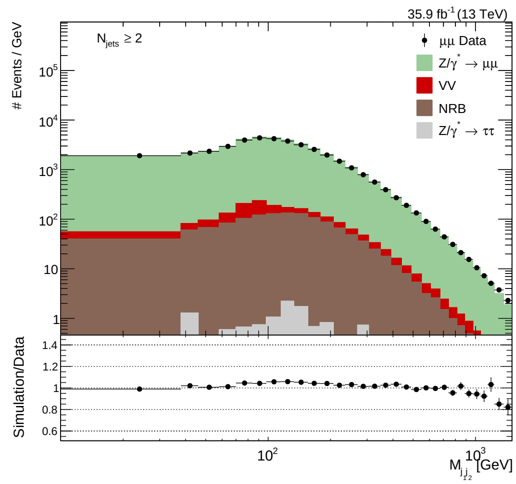

Figure 3·17: Invariant mass of leading and subleading jet.

3.7 Phenomenological Models and Theoretical Calculations

We compare the measured Z + jets differential cross sections to three calculations: MG5_AMC at next-to leading order (NLO), MG5_AMC at leading order (LO), and the GENEVA MC program [Alioli et al. (2015), Alioli et al. (2013)]. The two MG5_AMC calculations (version 2.2.2) [Alwall et al. (2014)] are interfaced with PYTHIA 8 (version 8.212) [Sjöstrand et al. (2015)]. For the LO MG5_AMC, the generator calculates LO MEs for five processes: pp $\rightarrow$ Z + Njets with $N = 0...4$. The NNPDF 3.0 LO PDF [Ball et al. (2015)] is used and $\alpha_S(m_Z)$ is set to 0.130. The NLO MG5_AMC prediction includes NLO ME calculations for pp $\rightarrow$ Z + Njets with N up to 2. The NNPDF 3.0 NLO PDF is used and $\alpha_S(m_Z)$ is set to 0.118. Both predictions use PYTHIA 8 to model the initial+final state parton showers (PS) and hadronization with the CUETP8M1 [Khachatryan et al. (2016)] tune that includes the NNPDF 2.3 [Ball et al. (2013)] LO PDF and $\alpha_S(m_Z) = 0.130$. ME and PS matching is done using the k_T-MLM [Alwall et al. (2008, 2009)] scheme with the matching scale set at 19 GeV for the LO MG5_AMC and the FxFx [Frederix and Frixione (2012)] scheme with the matching scale set to 30 GeV for the NLO MG5_AMC.

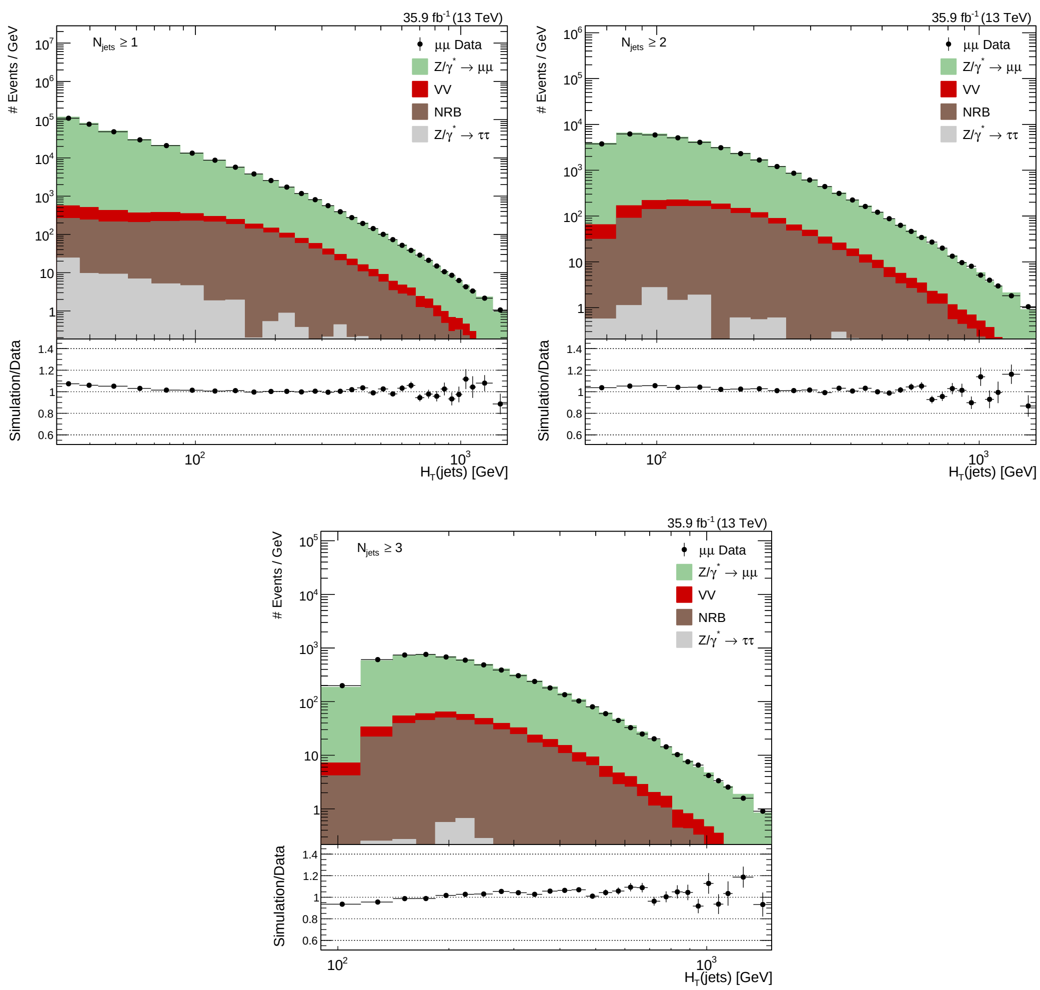

Figure 3·18: Total hadronic p_T one, two, and three jets inclusive.

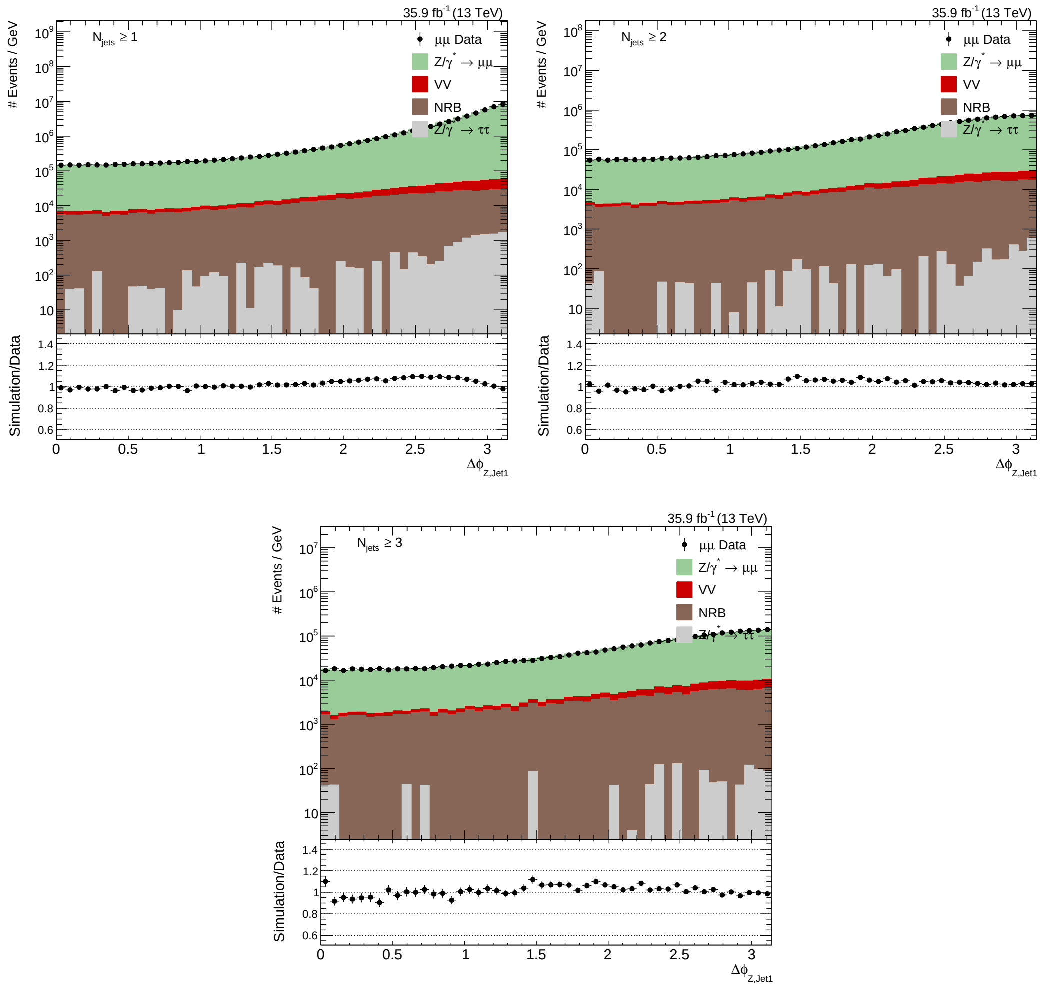

Figure 3·19: Difference in azimuthal angle between the Z boson and leading jet with one(left), two(right), and three(right) jet inclusive.

The GENEVA MC calculates up to Next-to-next LO (NNLO) in the Drell-Yan process. This additional order should provide a better description of the data in the high energy tails of distributions where perturbative QCD is dominant. In addition, the Next-to-next Leading Log (NNLL) terms are calculated using resummation to improve modeling in low p_{T} regions and reduce the dependence on the PS. To obtain fully exclusive final state prediction, a parton shower must still be used. PYTHIA 8 is used for both the parton shower and hadronization.

In this analysis uncertainties in the ME calculations are estimated for the NLO MG5_AMC as recommended by the authors. Fixed-order cross section calculations depend on the renormalization (μ_{R}) and factorization (μ_{F}) scales. The uncertainty coming from missing terms in the fixed-order calculation is estimated by varying the μ_{R} and μ_{F} scales by factors of 0.5 and 2. Uncertainties in PDF and α_S values are also estimated in the case of the FxFx-merged sample. The PDF uncertainty is estimated using the set of 100 replicas of the NNPDF 3.0 NLO PDF, and the uncertainty in the α_S value used in the ME calculation is estimated by varying it by ± 0.001. These two uncertainties are added in quadrature to the ME calculation uncertainties. All these uncertainties are obtained using the reweighting method [Frederix et al. (2012)] implemented in these generators. For the LO MG5_AMC and GENEVA samples, only statistical uncertainties are used.

3.8 Unfolding Procedure

Unfolding is done in order to reverse the effects of the detector and estimate the particle, or generator (GEN), level distributions in data. With a particle level distribution any theory or experimental data can be readily compared to the distributions without a need for detector simulation. Unfolding requires understanding the finite resolutions of the detector where an observable is smeared about its true value by a Gaussian of width equal to the resolution. The measured observables are also taken from a Poisson distribution with the true smeared or reconstructed (RECO) value as the mean. When considering binned distribution the unfolding problem amounts to solving the matrix equation Rx = y - b where R is the response matrix, x is the unknown particle level distribution, y is the measured reconstructed distribution, and b is the reconstructed background. The MadGraph5_aMC@NLO MC sample is used to extract the nominal response matrix that characterizes the detector transformation.

The response matrix R is created by a pair of observables where one value is at GEN level and the other at RECO level. Pairs are created by ordering the particles in p_{T} and selecting both with the same index. The ordering can be done by ΔR matches and can lower the mismatch rate for a GEN and RECO pair. Since the mismatch rate is at the percent level the response matrix and the unfolding is insensitive to how the matching is done and the p_{T} ordering is used for simplicity. If a GEN (RECO) observable does not have a matching RECO (GEN) observable it is put into the corresponding GEN (RECO) underflow bin. The GEN underflow bins are used in the TUnfold package [Schmitt (2012)] to calculate the efficiency since the underflow events represent events that were not found after reconstruction. The RECO underflow bins are events that do not have a GEN match and are considered fakes. A toy response matrix is shown in Figure 3·20. The matrix is normalized over a single GEN bin including the underflow bin. The normalization transforms the response matrix into probabilities for a GEN value in bin i to have a RECO match in bin j. The RECO background b and fakes are subtracted from the RECO distribution y bin by bin with the background approximated by both MC sample and data driven methods described in section 3.5.

The unfolding is done using the TUnfold package which utilizes a χ^2 minimization using a Tikhonov [Tikhonov (1963)] regularization term:

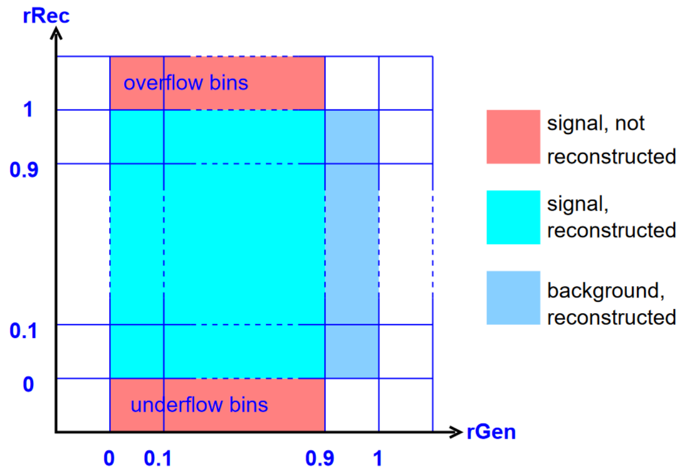

Figure 3·20: Example construction of a response matrix used in unfolding. The underflow and overflow regions are events that exist at particle level, but were not detected.

$$\chi^2 = \chi_0^2 + \chi_{reg}^2 = (y - Ax)^T V_{yy}^{-1}(y - Ax) + \tau^2 x^T L^{-1} Lx \tag{3.9}$$

where x and y have been previously defined, V is the RECO covariance matrix, τ is the regularization strength, and L defines the regularization conditions. The regularization term is needed to dampen Poisson fluctuation which tend to be amplified during the unfolding process. In this analysis the regularization term does not have a bias vector and is done in curvature mode where the matrix L is the discrete second derivative. To approximate the amount of regularization needed for a specific variable the condition of the response matrix can be calculated. The condition is the ratio of the largest and smallest single values of the response matrix. If the condition is low (< 10) then no regularization is most likely needed and if it is large ($> 10^4$) strong regularization is needed.

In this analysis variable associated with angles such as η and $|y|$ have low condition numbers and are unfolded without regularization. Momentum variables have condition numbers in between the extremes defined above and need some regularization. Condition values are shown on the response matrices for select variable in figures 3·21 - 3·23 and all condition numbers are shown in table 3.8. The strength of the regularization τ is chosen using the L-Curve method [Calvetti et al. (2004)]. This plots the minimized values of χ_0^2 vs χ_{reg}^2 with different value of τ. The location of highest curvature is chosen as the optimal amount of regularization.

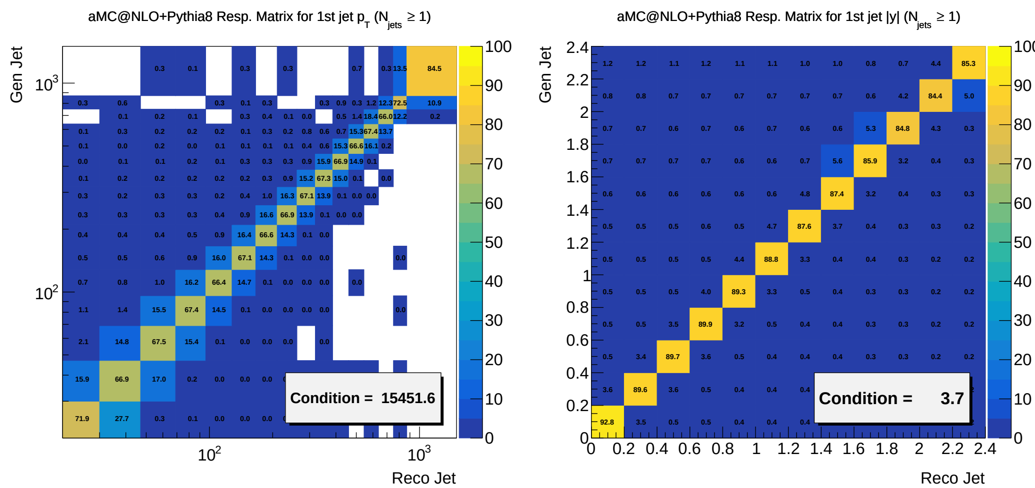

Figure 3·21: The response matrices of the leading jet $|y|$ (left) and p_T (right) with at least one jet. The reco and gen values are taken from the NLO MG5_aMC.

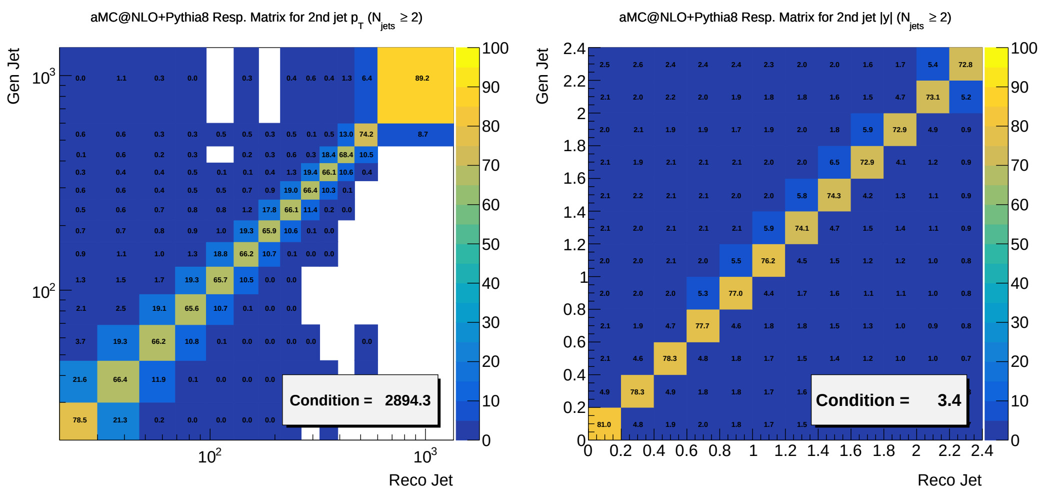

Figure 3·22: The response matrices of the second jet $|y|$ (left) and p_T (right) with at least two jets. The reco and gen values are taken from the NLO MG5_aMC.

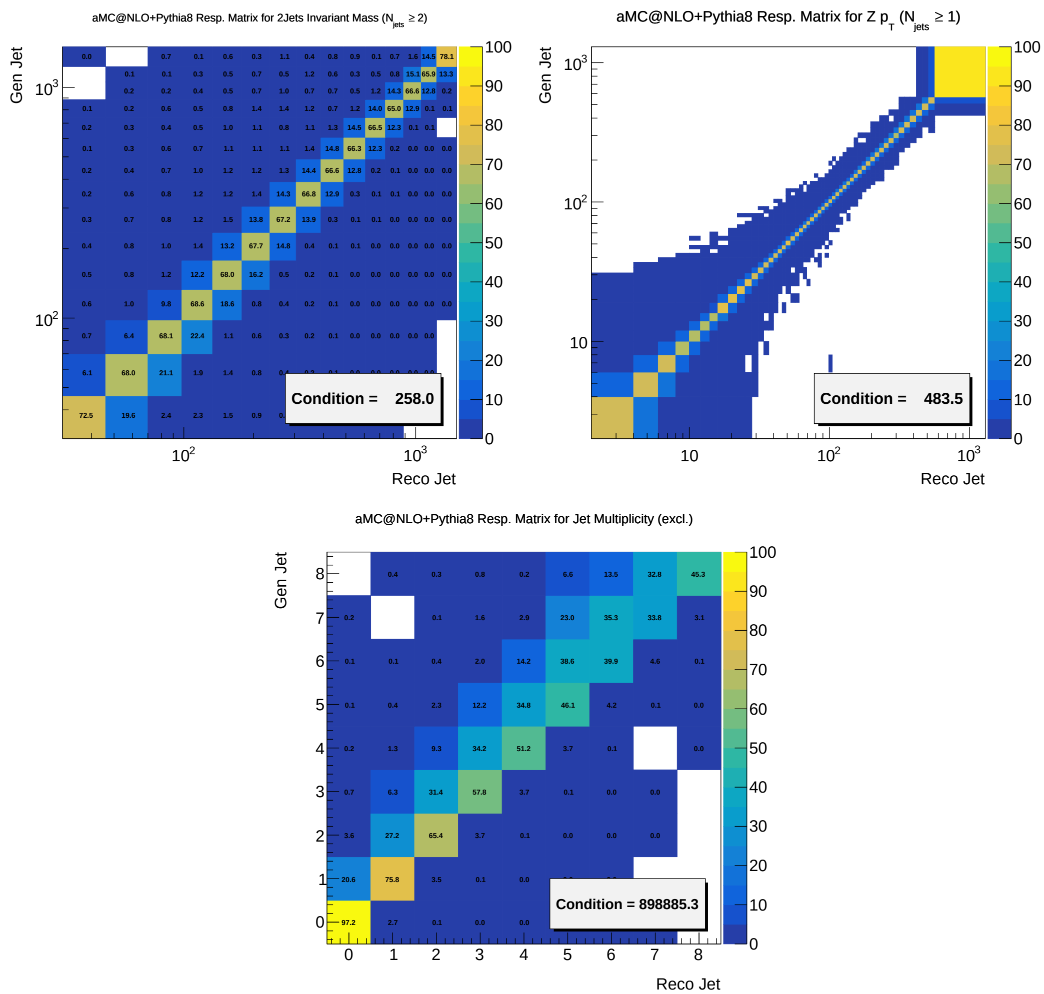

Figure 3·23: The response matrix of the dijet mass with at least two jets, the Z p_T with at least one jet, and the jet multiplicity exclusive. The reco and gen values are taken from the NLO MG5_aMC.

The statistical uncertainties from both the data distribution y and response matrix R are calculated analytically in the TUnfold package. The systematic uncertainties are calculated from an envelope of two unfolded distributions after varying the response matrix. More details of the systematic errors are given in section 3.9.

Unfolding is validated using the bottom line test and comparing the folded-unfolded data distributions to the RECO distributions as a closure test. For the bottom line test χ^2 is calculated for the unfolded and RECO space to check if $\chi^2_{Unf} \leq \chi^2_{Reco}$. A table of the χ^2 and degrees of freedom are shown in table 3.8. The number of degrees of freedom is approximately the number of bins in the respective space. The number of RECO bins is always two times the number of GEN bins as mentioned in the binning strategy above.

The binning for all variables is based on the detector resolution and statistics. A measure of detector resolution is migration and can be defined as the fraction of events of a GEN bin that are reconstructed to a different RECO bin. In this analysis at least 68% of the GEN events must be reconstructed in the same RECO bin. For better performance with unfolding the number of RECO bins is larger than the number of GEN bins. For all variables the number of RECO bins is double with each GEN bin split evenly in half. All bins are also adjusted so that at least 100 signal events in each bin of the data distribution to stabilize statistical fluctuations and lessen the need for regularization.

3.9 Systematical Uncertainties

The sources of experimental uncertainties are divided into the following categories: Jet Energy Scale (JES) and Jet Energy Resolution (JER), Lepton Efficiencies (identification, isolation, and track reconstruction), Lepton Energy Scale (LES) and Resolution (LER), Trigger efficiency, Luminosity, Pileup, Background and Unfolding uncertainties. The listed uncertainties are assumed to be independent such that each can be computed individually and added in quadrature to obtain a total uncertainty.

To compute the systematic uncertainty from each source, the analysis is repeated using the source values increased and decreased by 1σ from the central value to obtain a new response matrix. Unfolding is done using the varies response matrices and the envelop of the unfolded data is used to estimate the uncertainty. This results in bin-by-bin uncertainty contributions from each source in the unfolded distributions.

Jet Energy Scale and Resolution

The JES uncertainty originates mainly from HCAL uncertainties associated with a sampling calorimeter and it is the dominant source of systematic uncertainty. It affects both the reconstruction of the transverse energy of the selected jets and also the reconstructed kinematic variables measured with the calorimeter. In this analysis jet energy corrections (JEC) were applied to take into account inefficiencies, non-linearities and finite resolutions in energy and position of the reconstructed jets. The effect of the JES uncertainty is studied by scaling up and down the reconstructed jet energy by p_{T} and η-dependent scale factors. A similar procedure is followed for the JER. The uncertainties due to the JES and the JER vary in the range 1-11% as a function of jet multiplicity.

Muon Energy Scale and Resolution

The muon energy scale and resolution systematics are estimated from variations in the Rochester correction described in 3.3.1. The variations included in the package are statistical and parameters used in the fitting method such as the fitting function and Z mass window. For each event the RMS is calculated for the different statistical values and the maximum deviation is taken as the systematic for all other variations. All systematics are added in quadrature and the Rochester correction is pushed up or down by the total systematic about the central value. The scale and resolution uncertainties are due to modeling the energy loss through matter for low p_{T} muons and limits on DT and CSC resolution ($\sim$ 200-300 μm) for high p_{T} muons.

Muon Efficiencies

Efficiency uncertainties are calculated from variations done with the Tag and Probe method. The correlated sources include variations in the fit procedure, MC sample, and tag selection. A Breight-wigner is used as the alternate fit function to the nominal crystal ball function. The leading order Madgraph MC sample is used as the alternate sample to the nominal NLO Madgraph sample. For the alternate tag selection the p_{T} cut is increased to 35 GeV from the nominal of 30 GeV. All of these sources are treated as correlated and varied together.

For the statistical uncertainty each bin is treated as an independent uncertainty source and is not correlated with other bins. The analysis must be repeated then for each bin of the scale factor varied up and down by the statistical uncertainty. To reduce computation time the analysis is run only once and copies of the response matrices are produced corresponding to each scale factor bin variation. This is possible because the scale factor only changes the overall event weight and does not change the kinematics of any object. The data is then unfolded using all response matrix variations and the width is taken as the uncertainty. All variations are added in quadrature for each bin to obtain the total uncorrelated efficiency uncertainty.

Integrated Luminosity

A normalization uncertainty is assigned to the imperfect knowledge of the integrated luminosity. This is applied as an overall normalization uncertainty on all processes and takes a value of 2.5% [Collaboration (2017)].

Pile Up

To match the pileup conditions in data and in MC simulation, pileup reweighing is applied for the simulated samples. The reweighing factors depend on the minimum-bias cross section. We vary the nominal minimum-bias cross section of 69.2 mb up and down by its uncertainty of 4.6% when reconstructing the response matrices, and take the difference in the unfolded data as the uncertainty.

Background Cross Section

The resonant background samples are varied by their corresponding cross section uncertainty before being subtracted from data prior to unfolding. The non-resonant samples are varied by the uncertainty on the conversion factor $k_{e\mu}$. All background sources are varied at the same time and in the same direction.

Parton Distribution Function, α_S

Weights are provided in the MC signal sample corresponding to variations in the Parton Distribution Function (PDF) by changing (fill in). Each weight is used to fill the generator level histograms and creates an envelop for each histogram corresponding to the PDF variations. The standard deviation in each bin is calculated from:

$$\sigma^2 = \frac{\sum(var_i^2) - (\sum(var_i^2))^2}{nPDF(nPDF-1)} \tag{3.10}$$

where var_i is the bin value of the ith variation and nPDF is the total number of variations. The strong coupling constant α_S uncertainty is obtained in a similar way as the PDF where the variation is calculated from variations in weights. The weights correspond to α_S being varied by 0.001 from the nominal value of 0.118.

All uncertainties, except for statistical, are considered highly correlated across bins. This means if a particular source is increased, it will have an effect on all bins in the distribution. The statistical uncertainty in the scale factor is treated differently because a particular bin of the muon p_{T} and η would effect only a localized area of the Z p_{T} or Z y. Other sources, such as the JES, do not have this effect, and instead change the final distributions approximately equally for each bin. Two examples of the total correlations, the Z p_{T} and leading jet p_{T}, are shown in Figure 3·24. The dominant source of uncertainties, JES and lumi, are fully correlated so the correlations is close to one in most bins. This changes slightly in the tail where the uncorrelated statistical uncertainty becomes dominant.

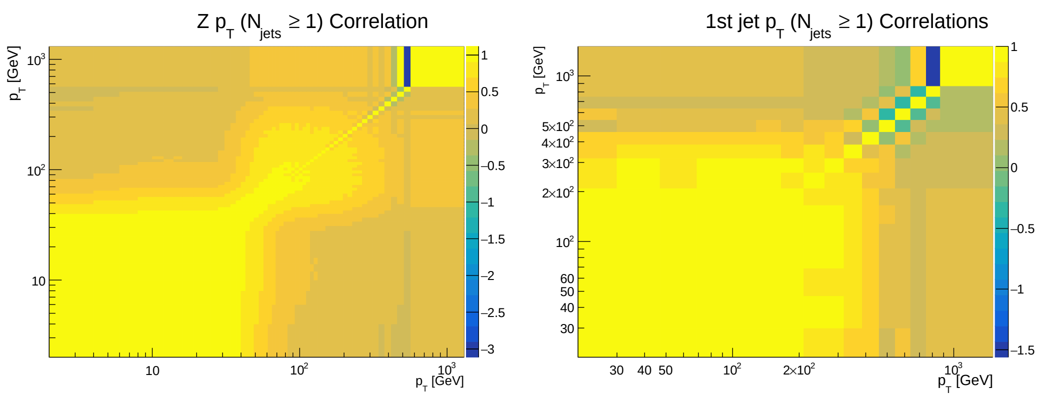

Figure 3·24: Total correlations of the Z p_{T} and leading jet p_{T}. Fully correlated jet energy scale and luminosity uncertainties dominate until the statistical limit at high p_{T}.

Unfolding

The uncertainty on the unfolding procedure is due to both the statistical uncertainty in the response matrix coming from the finite size of the MC sample used to compute it and to the possible event generator dependence of the response matrix itself.

Because of the finite statistics, a different binning will lead to a different response matrix. This uncertainty is estimated by weighting the MC to agree with the data in each distribution and building a new response matrix. The weighting is done using a finer binning than for the measurement. The difference between the nominal results and the results unfolded using the alternative response matrix is taken as the systematic uncertainty.

An additional uncertainty comes from the finite size of the MC sample used to build the response matrix. This source of uncertainty is called unfolding statistics ("unf stat") and is included in the systematic uncertainty of the measurement as well. Statistical fluctuations in the response matrix are propagated analytically in the TUnfold package.

The technique for estimating the unfolding uncertainty comes from the 2015 Z+jets analysis Sirunyan et al. (2018). The procedure mainly estimates the uncertainty from the shape within bins. The ratio of the background subtracted data and signal MC with 5 times finer binning is fit with Chebyshev polynomials. The function is then used to reweight the signal MC RECO level when repeating the analysis to create a varied response matrix. All unfolding steps are then repeated and the difference with the central value is taken to be the uncertainty.

Lastly, the background samples are varied by their corresponding cross section uncertainty before being subtracted from data prior to unfolding. The systematic uncertainties used for the combination of the electron and muon channels are summarized in Tables A.1 - A.37 in the Appendix.

3.10 Software

The analysis software has multiple stages in order to deal with the high level physics object from CMS events and reduce them to variable distributions. The process of creating the high level physics objects from raw detector data is done centrally and the reconstruction c++ code and object classes are defined in the CMS Software (CMSSW). The raw detector events are reconstructed with algorithms such as Particle Flow to pick out particles from an event and save information such as a particle four vector. Two layers of skims are then done to reduce the data set size and remove any information not necessary for physics analyses. The first skimmed data set is called Analysis Object Data (AOD) and the second is miniAOD. The miniAOD data set is used as the starting point of this analysis.

The first step of the analysis software, called Shears framework, is to reduce the miniAOD data set further and remove the class structure. This is done in two steps called Baobab and Bonsai. Baobab is an EDAnalyzer and interacts directly with miniAOD. The skimming in Shears is done by saving only lepton, AK04 jets, trigger information, and weights from each event. The miniAOD is organized in classes such as "muon" where the objects have member variables such as the four vector. This makes reading and writing events to file difficult and adds unnecessary complexity to the analysis. Shears takes the information in "muon" and saves it as vectors where the index is the ith muon in the event. This format is typically called flat ntuples. This means an event will contain a vector for the muons p_{T} and the first element will be the p_{T} of the first muon in the event. Care has to be taken so that the vectors of the same physics object all have the same size and the indices match.

Preliminary cuts on the objects saved can be done during the Baobab stage to further reduce the size, but all events must be counted to preserve the luminosity estimate for MC. Commonly, a soft momentum cut is used for both the leptons and jets around 10 GeV and events must have at least one lepton to be saved. In the Bonsai stage of Shears we skim based on the final state particles we are looking for in the analysis. For this Z analysis we require at least two leptons and cut lepton p_{T} at 15 GeV.

The ntuples are less than 5TB for the full $36\,\mathrm{fb}^{-1}$ and can be stored on a local cluster or private space on a CMS Tier 2/3 machine. The final step of producing variable histograms uses the ntuples as the input events. When running over events in the ntuple all histograms are filled with information from one event at a time. The MC weights and any corrections are done on the fly and respect the order in which the corrections are derived such as applying the muon ID scale factors before applying the Rochester corrections.

3.11 Results

The 2016 data statistically allows us to determine the differential cross sections of jet multiplicities up to eight jets and to study the cross sections as a function of several kinematic observables up to five jets. The single-differential and double-differential cross section measurements for unfolded data are shown in Figures 3·25-3·47. All results are compared with theoretical prediction from MG5_aMC at LO and MG5_aMC at NLO and compared to the GENEVA MC program for results with at least one or two jets.

The single differential as a function of jet transverse momenta and rapidities up to five leading jets can be seen in figures 3·25-3·29, and the double-differential as a function of leading jet y and p_{T} can be seen in Figure 3·30. For all quantities data distributions are well reproduced by the simulations. The MG5_aMC at LO, MG5_aMC at NLO, describe the data well in general. The GENEVA prediction shows good agreement for the measured p_{T} and y of the first jet, while it undershoots the data at low p_{T} for the second jet. Adding higher order terms does not lead to significant changes in agreement even at the highest jet p_{T}.

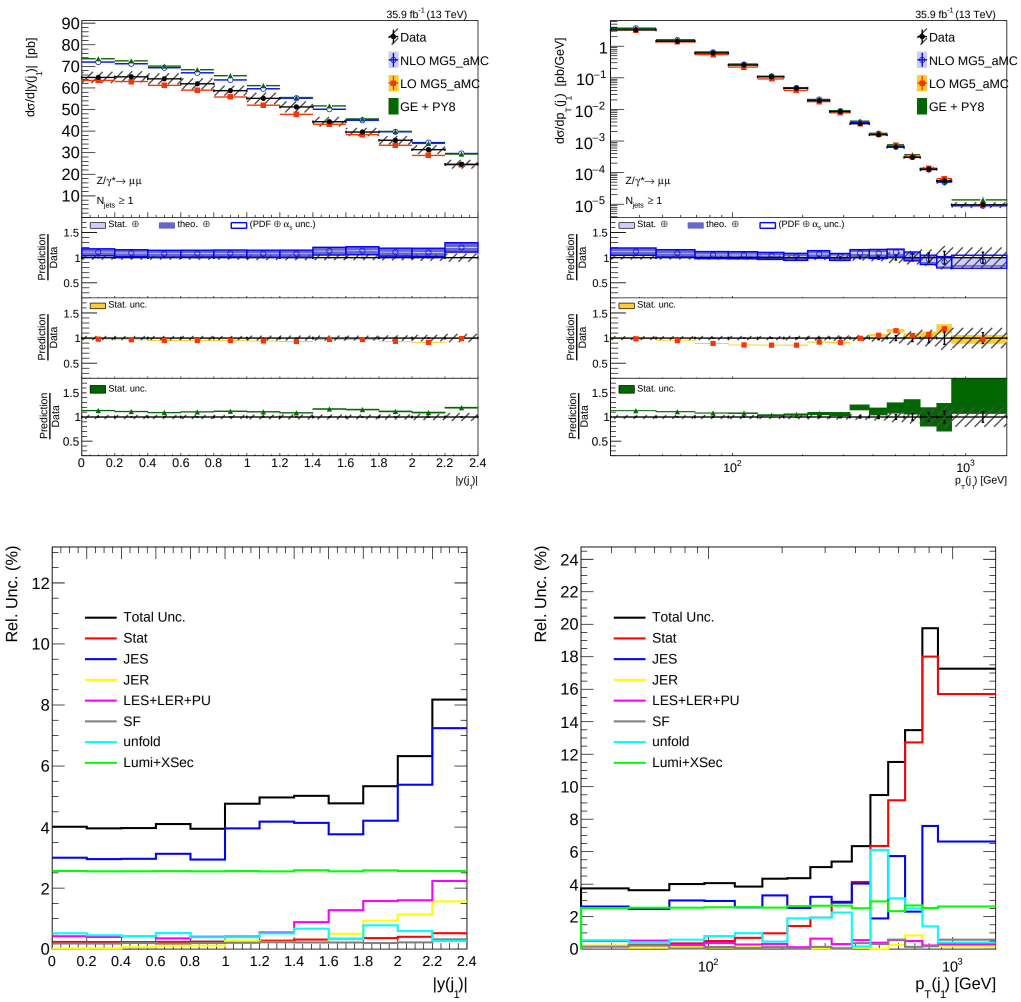

Figure 3·25: The measured differential cross section as a function of leading jet $|y|$ (left) and p_T (right) with at least one jet for the combined channel. For data the black bars show the statistical uncertainty and the hashed area shows the total uncertainty. A break down of the uncertainty for each bin is shown in the right plots with sources defined in section 3.9. The measurement is compared to NLO MG5_AMC, LO MG5_AMC, and GENEVA. The uncertainty for predictions is shown only in the ratio plots with statistical, PDF, and scale uncertainties for the NLO MG5_AMC and statistical only for the GENEVA and LO MG5_AMC predictions.

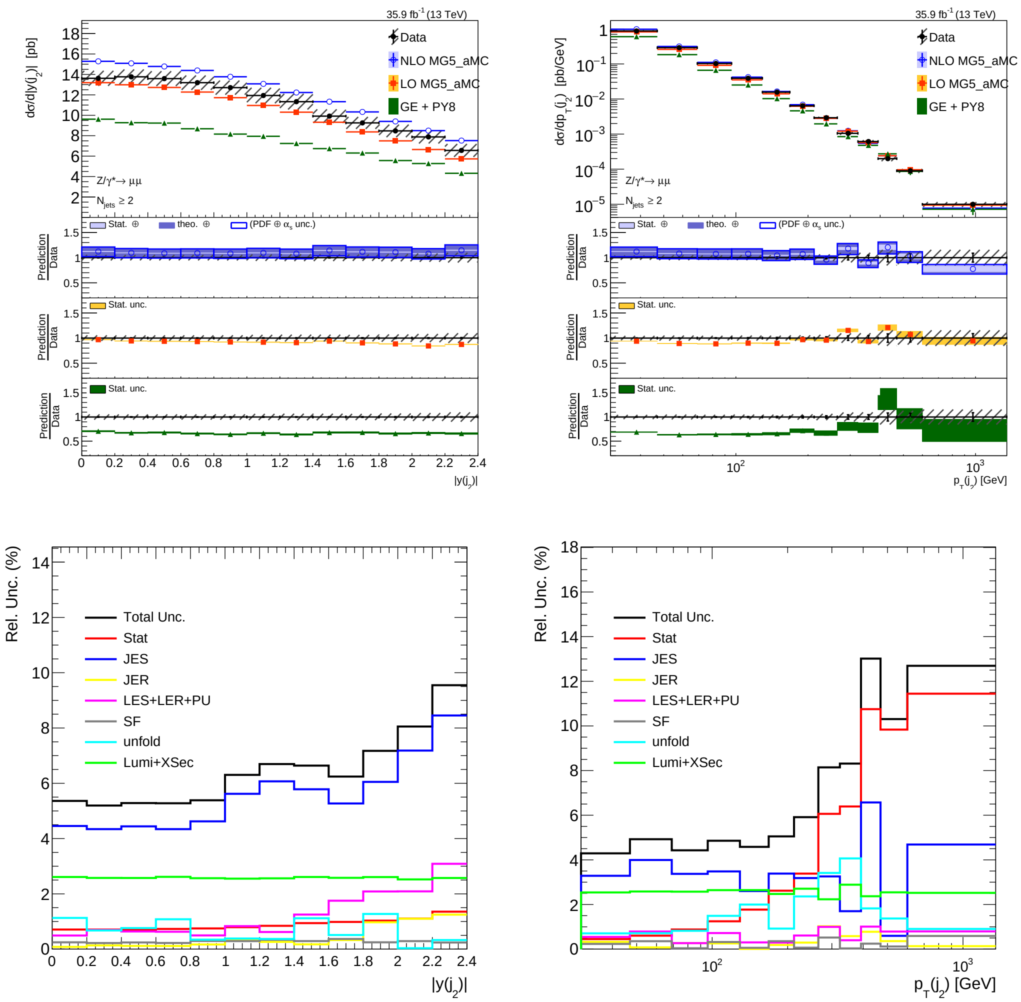

Figure 3·26: The measured differential cross section as a function of second jet $|y|$ (left) and p_T (right) with at least two jets for the combined channel. For data the black bars show the statistical uncertainty and the hashed area shows the total uncertainty. A break down of the uncertainty for each bin is shown in the right plots with sources defined in section 3.9. The measurement is compared to NLO MG5_AMC, LO MG5_AMC, and GENEVA. The uncertainty for predictions is shown only in the ratio plots with statistical, PDF, and scale uncertainties for the NLO MG5_AMC and statistical only for the GENEVA and LO MG5_AMC predictions.

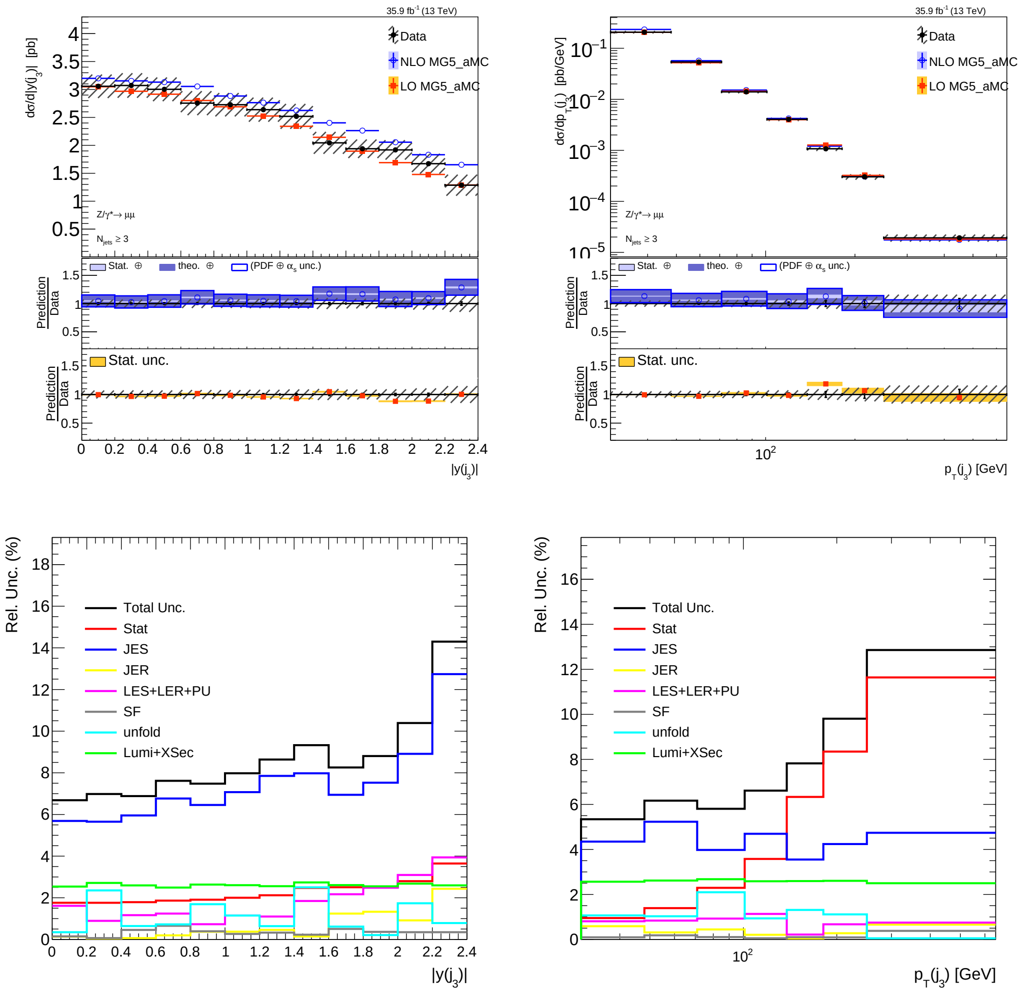

Figure 3·27: The measured differential cross section as a function of third jet $|y|$ (left) and p_T (right) with at least three jets for the combined channel. For data the black bars show the statistical uncertainty and the hashed area shows the total uncertainty. A break down of the uncertainty for each bin is shown in the right plots with sources defined in section 3.9. The measurement is compared to NLO MG5_aMC and LO MG5_aMC. The uncertainty for predictions is shown only in the ratio plots with statistical, PDF, and scale uncertainties for the NLO MG5_aMC and statistical only for the LO MG5_aMC predictions.

Table 3.8: Unfolding Numbers

Variable	Condition	χ^2_{reco}	χ^2_{unf}	dof
ZNGoodJets_Zexc	898885.30	14935.47	11828.81	9
FirstJetPt_Zinc1jet	15451.57	537053.62	14540.67	16
SecondJetPt_Zinc2jet	2894.30	154113.95	1959.30	13
ThirdJetPt_Zinc3jet	629.64	34252.99	225.41	8
FourthJetPt_Zinc4jet	339.46	5810.82	489.48	6
FifthJetPt_Zinc5jet	49.86	736.75	349.78	4
FirstJetAbsRapidity_Zinc1jet	3.66	124313.38	2747.19	12
SecondJetAbsRapidity_Zinc2jet	3.41	34030.45	644.80	12
ThirdJetAbsRapidity_Zinc3jet	3.44	7930.90	338.65	12
FourthJetAbsRapidity_Zinc4jet	4.08	632.03	94.84	12
FifthJetAbsRapidity_Zinc5jet	3.85	73.18	136.64	12
JetsHT_Zinc1jet	3420.74	283062.72	12113.22	16
JetsHT_Zinc2jet	578.42	54492.54	1893.86	15
JetsHT_Zinc3jet	107.43	9221.13	215.51	14
JetsHT_Zinc4jet	18.83	581.50	319.55	12
JetsHT_Zinc5jet	6.43	49.74	177.80	11
JetsMass_Zinc2jet	258.05	39265.41	1868.91	15
ZPt_Zinc0jet	8522.58	75441.58	70094.66	55
ZPt_Zinc1jet	483.48	208237.88	9300.63	54
ZPt_Zinc2jet	92.32	38695.40	1737.56	54
ZAbsRapidity_Zinc1jet	10.80	120353.26	1732.65	12
SumZFirstJetRapidity_Zinc1jet	114.36	121250.61	2499.35	12
DifZFirstJetRapidity_Zinc1jet	1411.84	120186.84	3619.02	12
SumZFirstJetRapidity_Zinc2jet	142.76	33426.92	1194.56	12
DifZFirstJetRapidity_Zinc2jet	873.23	33422.14	769.24	12
SumZSecondJetRapidity_Zinc2jet	214.57	33478.54	963.12	12
DifZSecondJetRapidity_Zinc2jet	479.07	33442.64	859.86	12
SumZTwoJetsRapidity_Zinc2jet	155.73	33445.96	657.31	6
DifZTwoJetsRapidity_Zinc2jet	2325.62	33404.99	563.19	6
SumFirstSecondJetRapidity_Zinc2jet	72.41	33799.86	2880.53	12
DifFirstSecondJetRapidity_Zinc2jet	238.31	33460.06	1174.13	12
DPhiZFirstJet_Zinc1jet	185.33	132910.98	8507.17	25
DPhiZFirstJet_Zinc2jet	37.45	33627.87	2072.65	25
DPhiZFirstJet_Zinc3jet	17.11	7774.54	586.37	25
DPhiZSecondJet_Zinc2jet	2.92	33739.31	1634.70	25
DPhiZSecondJet_Zinc3jet	2.82	7709.30	402.89	25
DPhiZThirdJet_Zinc3jet	4.52	7931.24	705.20	25
DPhiFirstSecondJet_Zinc2jet	7.73	33541.43	1932.58	25
DPhiFirstSecondJet_Zinc3jet	9.67	7829.29	537.04	25
DPhiFirstThirdJet_Zinc3jet	4.33	7820.15	415.85	25
DPhiSecondThirdJet_Zinc3jet	2.96	8440.03	923.12	25

In addition, the inclusive jet differential cross sections as a function of H_T for events with at least one, two, three jets respectively are presented in figure 3·31 and in dijet mass in Figure 3·32. Both MG5_aMC at LO and MG5_aMC at NLO are compatible with the measurement. The contribution at higher values of H_T is slightly overestimated, but the discrepancy is compatible with the theoretical and experimental uncertainties. The slopes of the distributions for the first two jet multiplicities predicted by GENEVA samples do not fully describe the data.

In all jet distributions the JES is the leading uncertainty below the statistical limit. In the leading jet distributions the JES uncertainty is as low as 3% and on par with the lumi uncertainty up to 600 GeV.

In figure 3·33 the measured cross sections as a function of the inclusive and exclusive jet multiplicity, for a total number of up to 8 jets in the final state, are shown. The trend of the jet multiplicity represents the expectation of the pQCD prediction for an exponential decay with the number of jets. The agreement is very satisfactory for both distributions for all the theoretical estimations, within the uncertainties and going up to the maximum number of final state partons included in the ME, namely 4 in the MC generators used here. Even at higher multiplicities, where a tuned PS model is used, the agreement is within theoretical uncertainty. Adding more jets in the hard scattering, NNLO and beyond, does not look promising when the PS already achieves this.

The GENEVA predictions do not model the jet multiplicity for events with greater than 2 jets. This is a result of using PS tune parameters from a different generator. If a dedicated tune was used the agreement should be of the same order as the MG5_aMC samples.

The $p_T(Z)$ distribution in figure 3·34 is described well above the jet cut of 30 GeV where the kinematics are dominated by jets modeled by hard scattering. Below the

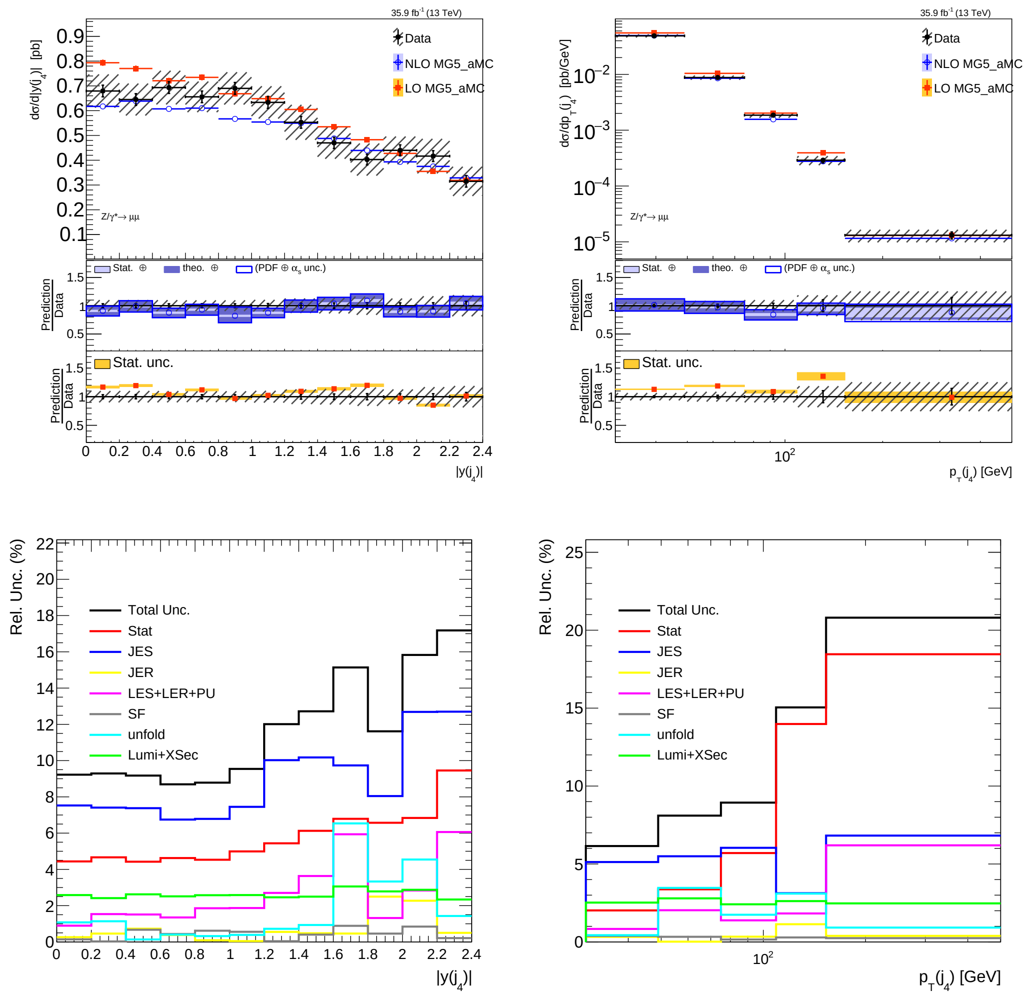

Figure 3·28: The measured differential cross section as a function of fourth jet $|y|$ (left) and p_T (right) with at least four jets for the combined channel. For data the black bars show the statistical uncertainty and the hashed area shows the total uncertainty. A break down of the uncertainty for each bin is shown in the right plots with sources defined in section 3.9. The measurement is compared to NLO MG5_AMC and LO MG5_AMC. The uncertainty for predictions is shown only in the ratio plots with statistical, PDF, and scale uncertainties for the NLO MG5_AMC and statistical only for the LO MG5_AMC predictions.

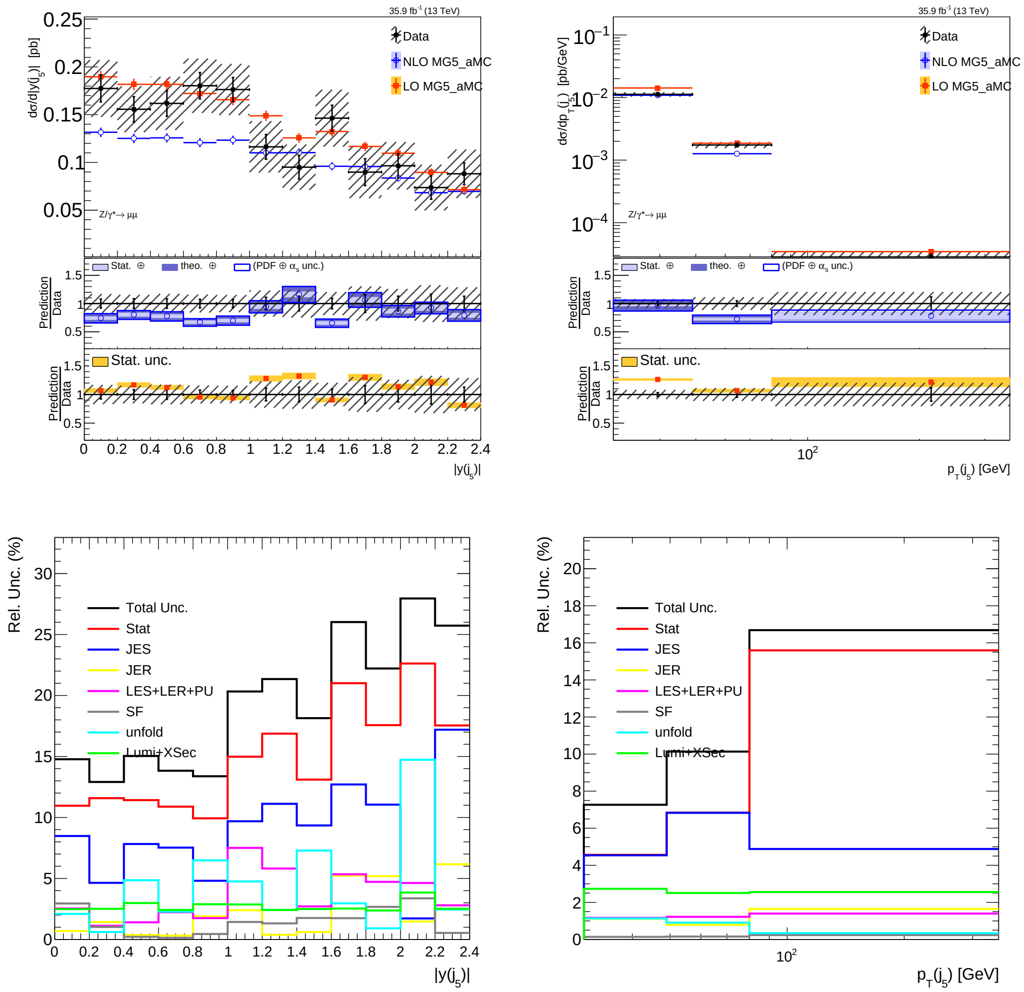

Figure 3·29: The measured differential cross section as a function of fifth jet $|y|$ (left) and p_T (right) with at least five jets for the combined channel. For data the black bars show the statistical uncertainty and the hashed area shows the total uncertainty. A break down of the uncertainty for each bin is shown in the right plots with sources defined in section 3.9. The measurement is compared to NLO MG5_aMC and LO MG5_aMC. The uncertainty for predictions is shown only in the ratio plots with statistical, PDF, and scale uncertainties for the NLO MG5_aMC and statistical only for the LO MG5_aMC predictions.

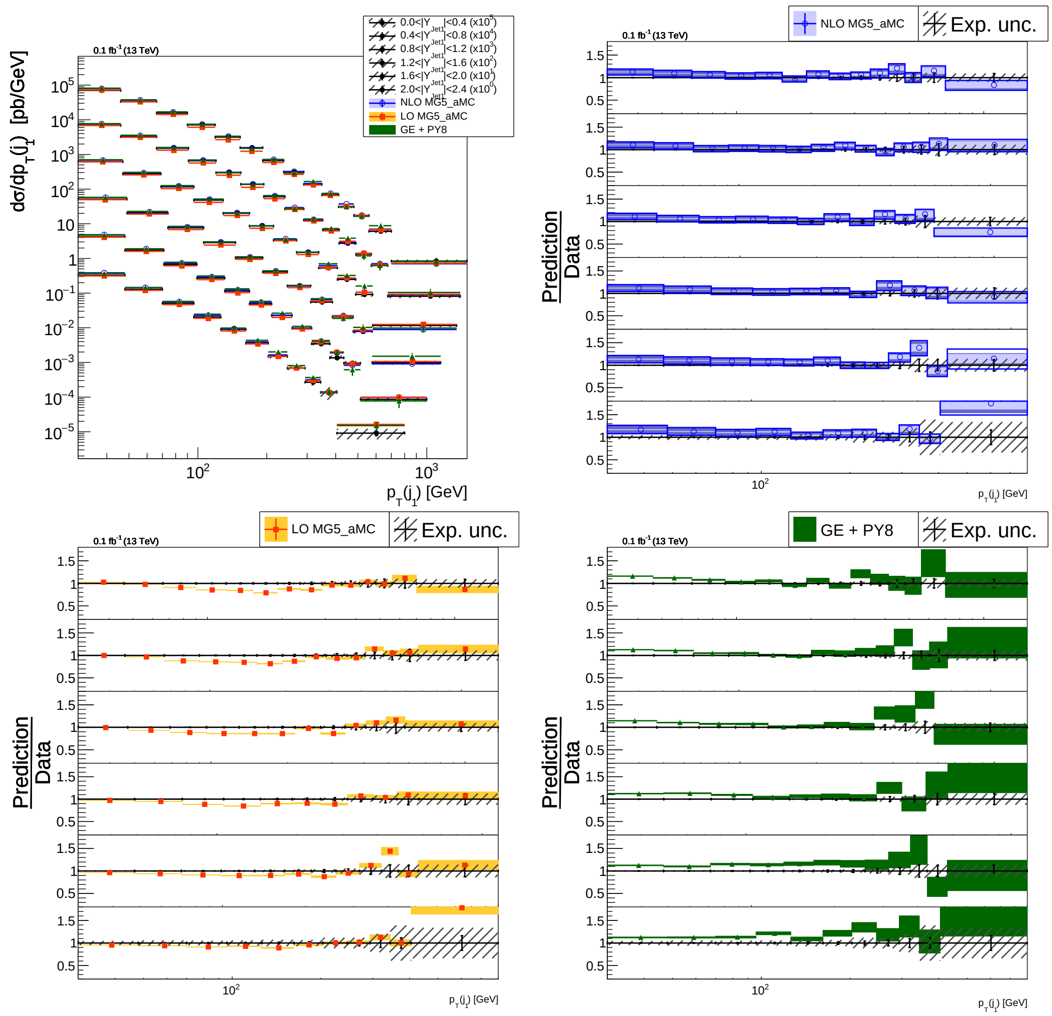

Figure 3·30: Double differential cross section as a function of leading jet p_T and rapidity with at least one jet (upper left). For data the black bars show the statistical uncertainty and the hashed area shows the total uncertainty. The measurement is compared to NLO MG5_aMC, LO MG5_aMC, and GENEVA and the ratios are shown in the upper right, lower left, and lower right plots, respectively. The uncertainty for predictions is shown only in the ratio plots with statistical, PDF, and scale uncertainties for the NLO MG5_aMC and statistical only for the GENEVA and LO MG5_aMC predictions.

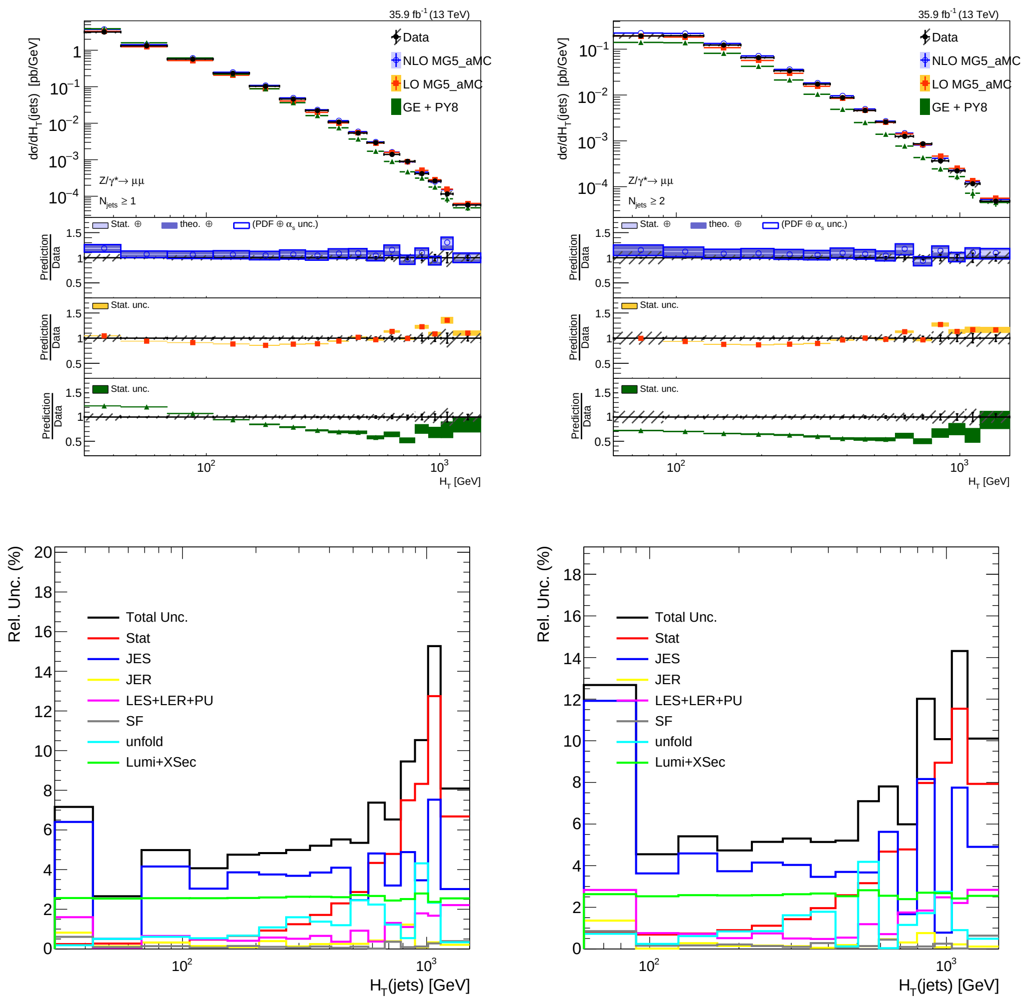

Figure 3·31: The measured differential cross section as a function of total hadronic p_T with at least one(left), two(middle), and three(right) jets. For data the black bars show the statistical uncertainty and the hashed area shows the total uncertainty. A break down of the uncertainty for each bin is shown in the right plots with sources defined in section 3.9. The measurement is compared to NLO MG5_AMC and LO MG5_AMC. The measurements with at least one and two jets is also compared to GENEVA. The uncertainty for predictions is shown only in the ratio plots with statistical, PDF, and scale uncertainties for the NLO MG5_AMC and statistical only for the GENEVA and LO MG5_AMC predictions.

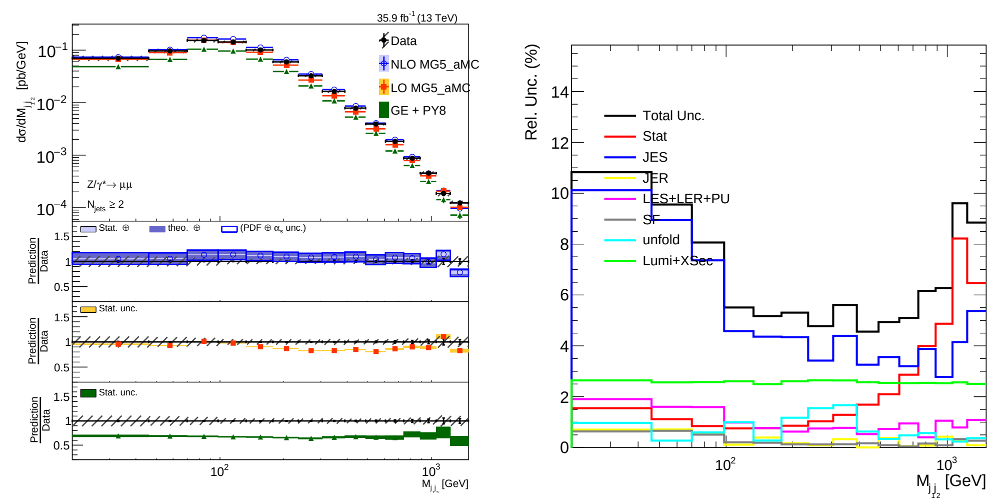

Figure 3·32: The measured differential cross section as a function of dijet mass with at least two jets. For data the black bars show the statistical uncertainty and the hashed area shows the total uncertainty. A break down of the uncertainty for each bin is shown in the right plots with sources defined in section 3.9. The measurement is compared to NLO MG5_aMC, LO MG5_aMC, and GENEVA. The uncertainty for predictions is shown only in the ratio plots with statistical, PDF, and scale uncertainties for the NLO MG5_aMC and statistical only for the GENEVA and LO MG5_aMC predictions.

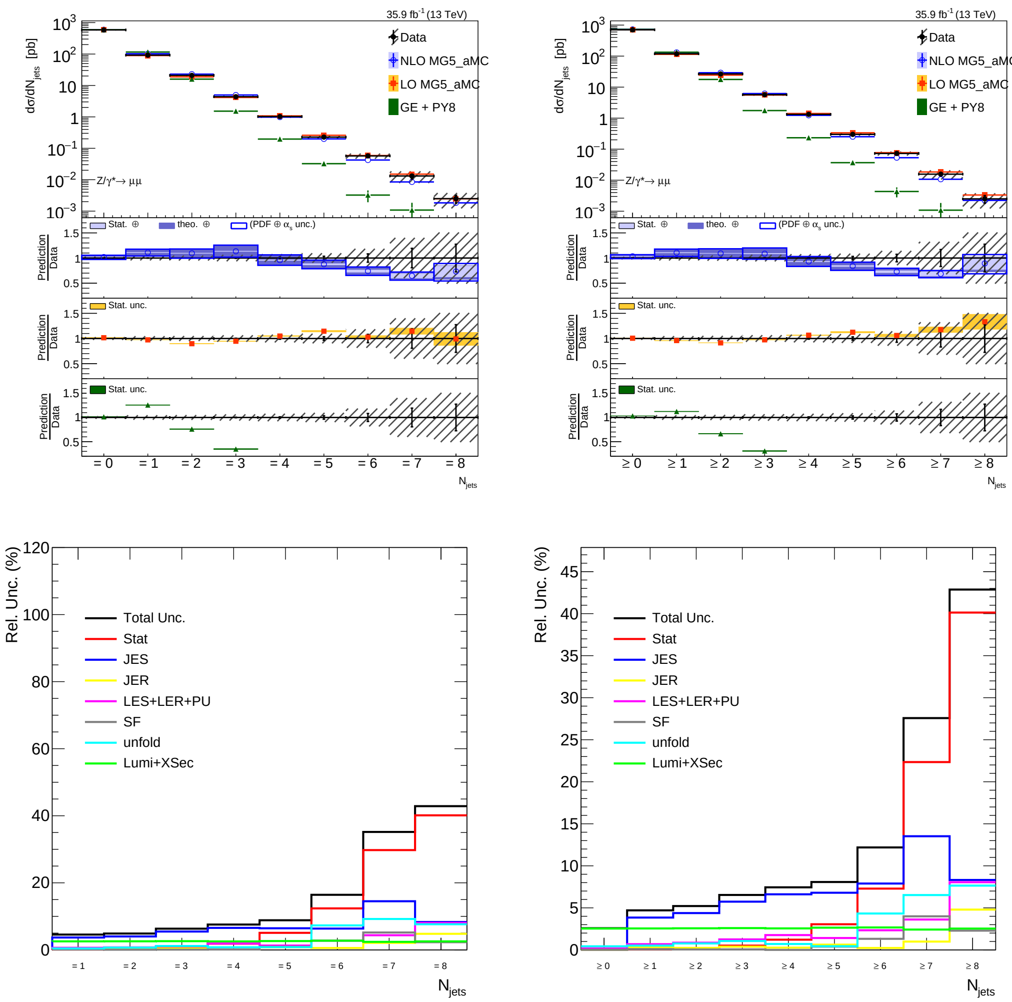

Figure 3·33: The measured differential cross section as a function of jet multiplicity exclusive (left) and inclusive (right). For data the black bars show the statistical uncertainty and the hashed area shows the total uncertainty. A break down of the uncertainty for each bin is shown in the right plots with sources defined in section 3.9. The measurement is compared to NLO MG5_aMC, LO MG5_aMC, and GENEVA. The uncertainty for predictions is shown only in the ratio plots with statistical, PDF, and scale uncertainties for the NLO MG5_aMC and statistical only for the GENEVA and LO MG5_aMC predictions.

jet cut of 30 GeV non-perturbative QCD effects become dominant. For the zero jet case, The GENEVA predictions show a few percent improvement over both NLO and LO MG5_aMC in this non-perturbative region. In the one jet distribution, the predictions show significant deviations from data in the same regions. GENEVA shows promise in the lowest bins but has large discrepancies right around the p_{T} peak. The strategy of adding in NNLL terms with resummation so far appears to improve modeling at low p_{T} by a few percent, but causes problem when a hard jet is introduced. The $p_{\mathrm{T}}(Z)$ measurements broken into 6 bins in $|y|$, shown in Figure 3·36, shows the same trends in modeling as the single differential distribution.

The uncertainty in the $p_{\mathrm{T}}(Z)$, shown figure 3·34, is dominated at low energy by the JES uncertainty. This is caused by jets being pushed above and below the cut of 30 GeV and changing the number of Z events in a particular inclusive bin. Above the jet cut, the uncertainty drops drastically to 2.5% from the lumi.

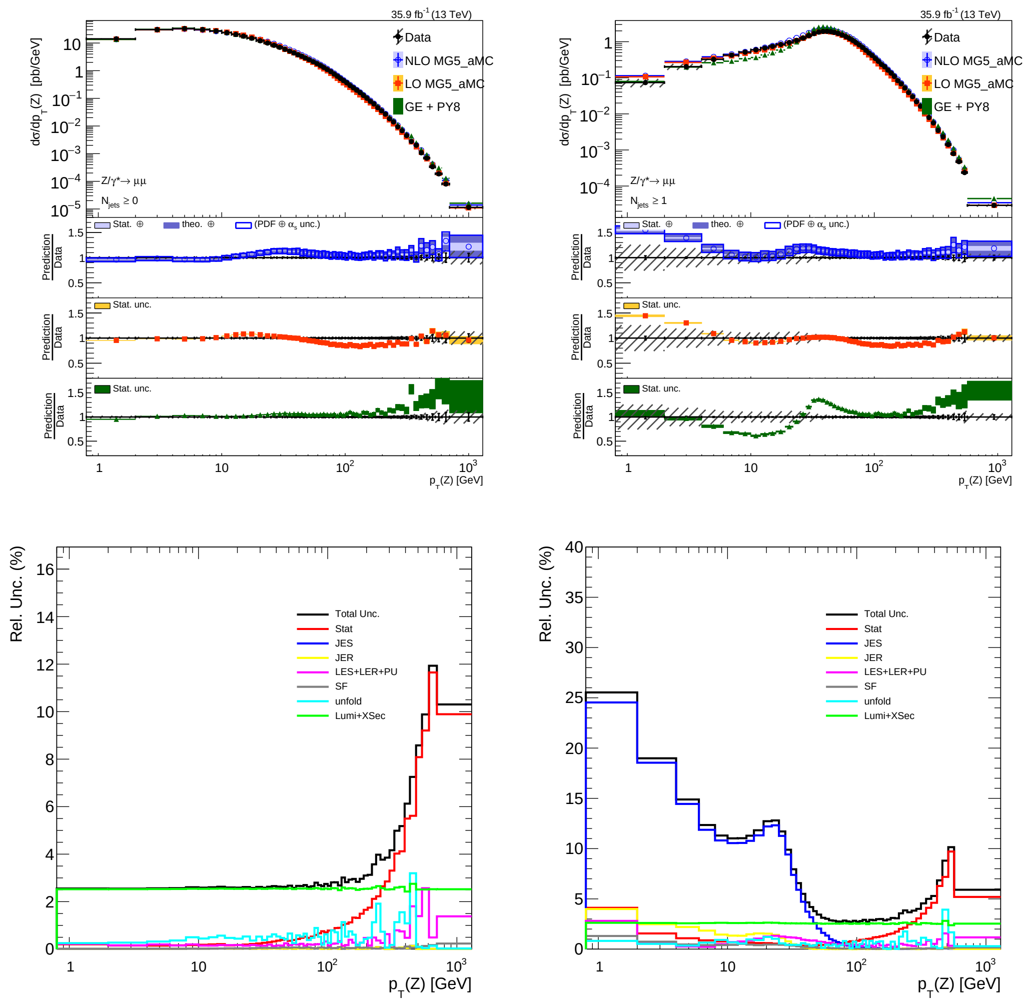

Figure 3·34: The measured differential cross section as a function of Z p_T with at least zero jets (left) and at least one jet (right). For data the black bars show the statistical uncertainty and the hashed area shows the total uncertainty. A break down of the uncertainty for each bin is shown in the right plots with sources defined in section 3.9. The measurement is compared to NLO MG5_AMC, LO MG5_AMC, and GENEVA. The uncertainty for predictions is shown only in the ratio plots with statistical, PDF, and scale uncertainties for the NLO MG5_AMC and statistical only for the GENEVA and LO MG5_AMC predictions.

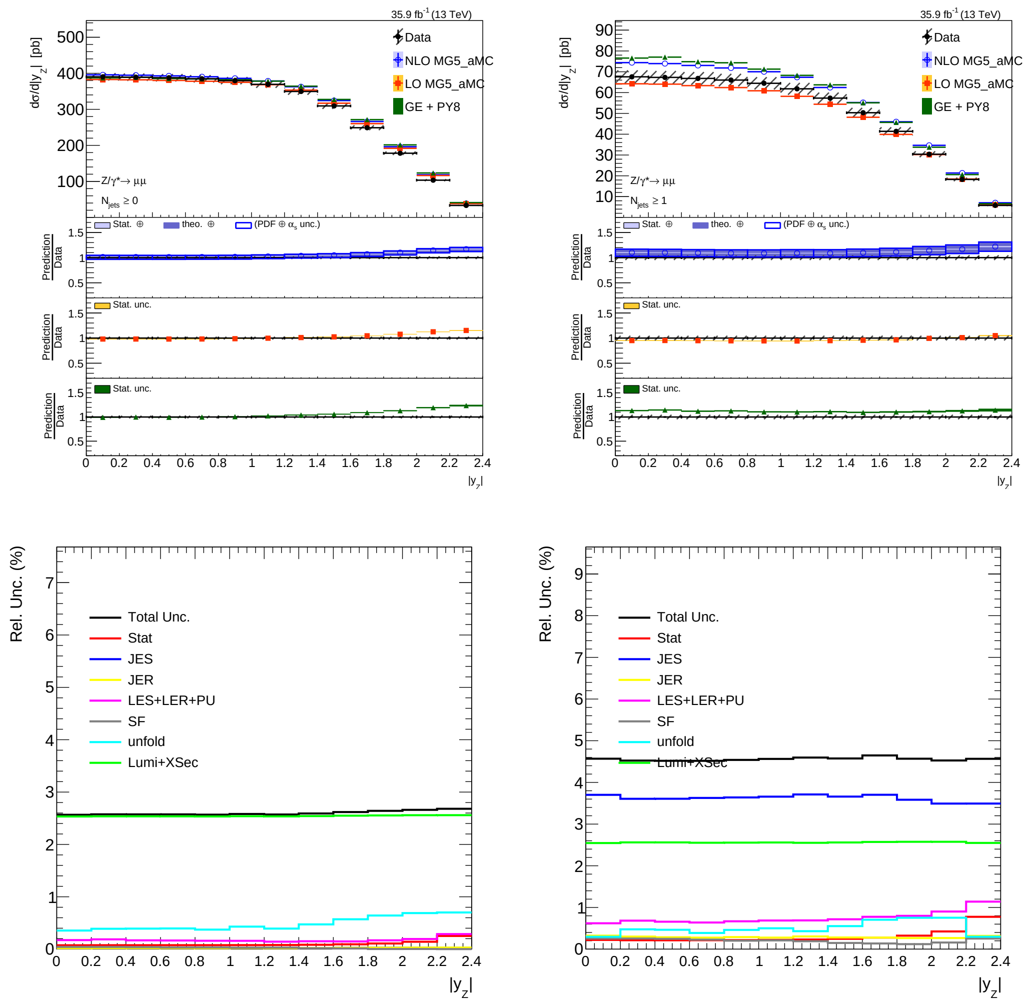

Figure 3·35: The measured differential cross section as a function of Z rapidity with at least zero jets (left) with at least one jet (right). For data the black bars show the statistical uncertainty and the hashed area shows the total uncertainty. A break down of the uncertainty for each bin is shown in the right plots with sources defined in section 3.9. The measurement is compared to NLO MG5_AMC, LO MG5_AMC, and GENEVA. The uncertainty for predictions is shown only in the ratio plots with statistical, PDF, and scale uncertainties for the NLO MG5_AMC and statistical only for the GENEVA and LO MG5_AMC predictions.

The differential cross sections as a function of rapidity sum and difference, between combinations of the Z and jets, and $\Delta\Phi$ are shown in Figures 3·38 - 3·47. For the LO MG5_aMC and GENEVA 10% and 20% discrepancies are seen in many rapidity distributions. Adding the NLO term for MG5_aMC improves the agreement significantly especially in the rapidity sum and difference between the Z and leading jet in Figure 3·39. The NLO reduces the discrepency from 25% to 5% in many bins and does not show any significant shape difference. Going to higher order seems to spoil this agreement where the GENEVA is similar to the LO with at least 25% differences.

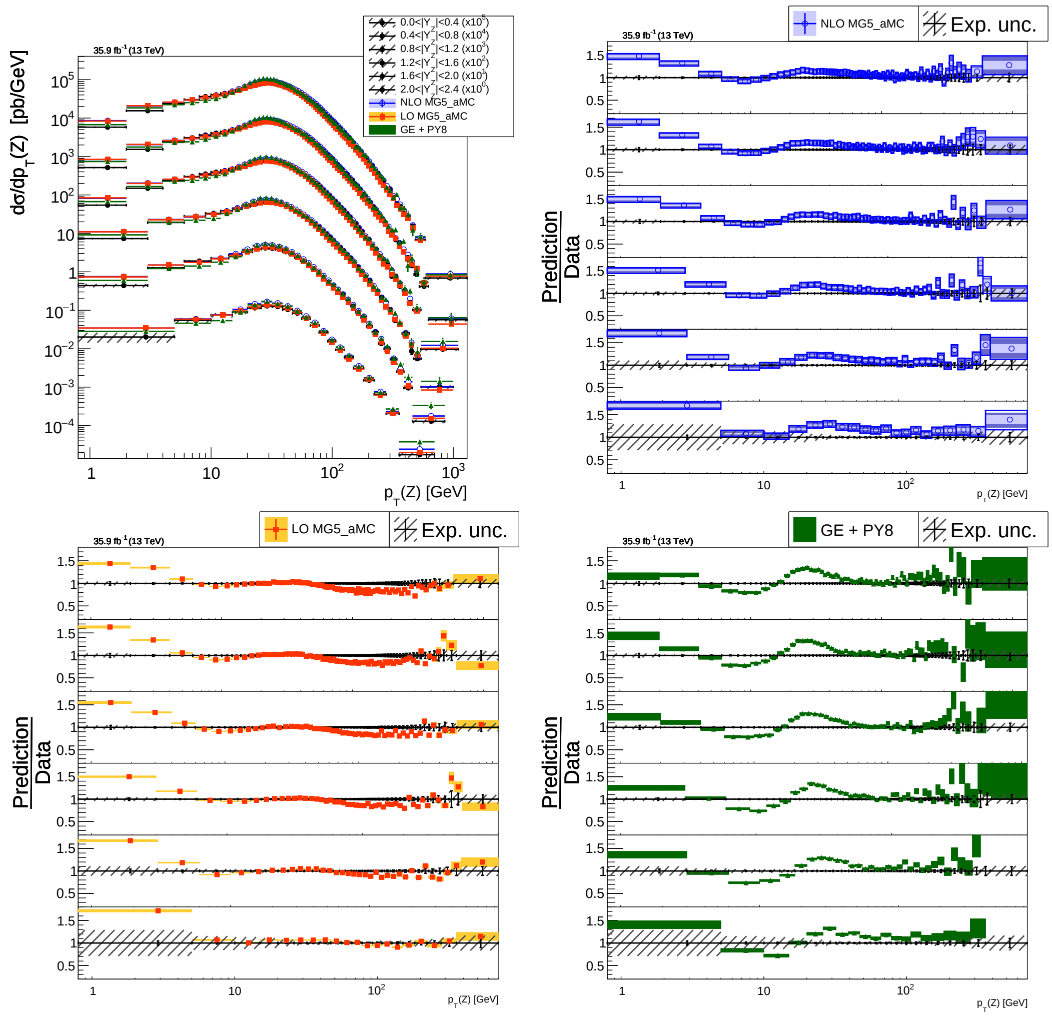

Figure 3·36: Double differential cross section as a function of Z boson p_T and rapidity with at least one jet. For data the black bars show the statistical uncertainty and the hashed area shows the total uncertainty. The measurement is compared to NLO MG5_aMC, LO MG5_aMC, and GENEVA and the ratios are shown in the upper right, lower left, and lower right plots, respectively. The uncertainty for predictions is shown only in the ratio plots with statistical, PDF, and scale uncertainties for the NLO MG5_aMC and statistical only for the GENEVA and LO MG5_aMC predictions.

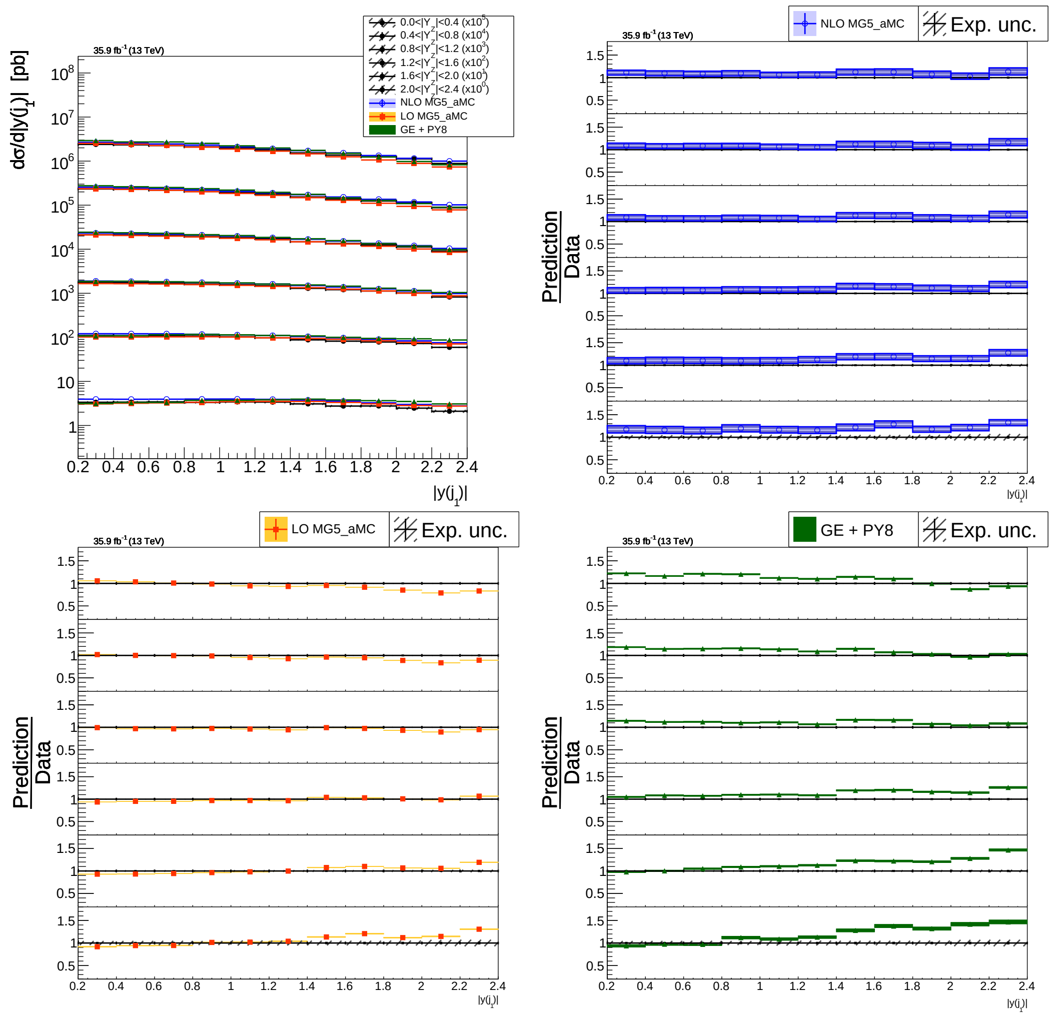

Figure 3·37: Double differential cross section as a function of leading jet and Z boson rapidity with at least one jet. For data the black bars show the statistical uncertainty and the hashed area shows the total uncertainty. The measurement is compared to NLO MG5_aMC, LO MG5_aMC, and GENEVA and the ratios are shown in the upper right, lower left, and lower right plots, respectively. The uncertainty for predictions is shown only in the ratio plots with statistical, PDF, and scale uncertainties for the NLO MG5_aMC and statistical only for the GENEVA and LO MG5_aMC predictions.

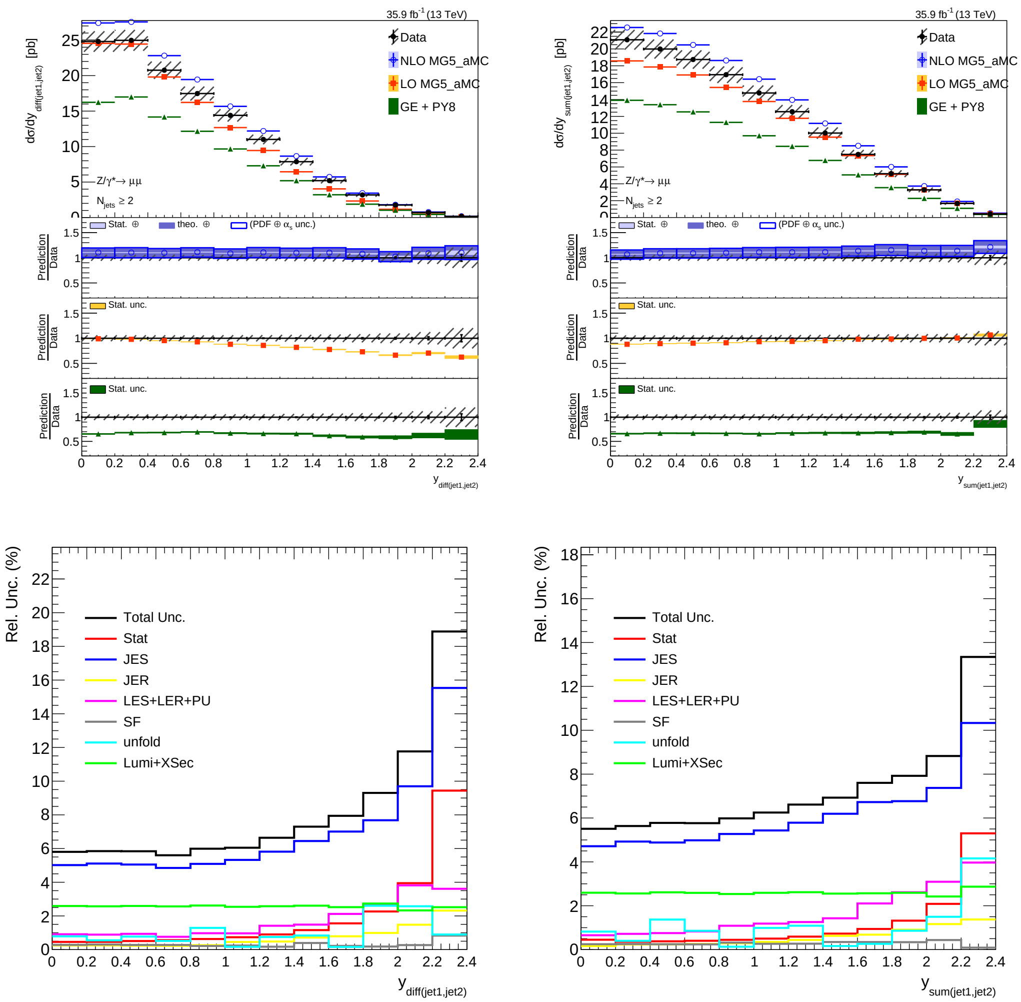

Figure 3·38: The measured differential cross section as a function of the leading and subleading jet rapidity difference(left) and sum(right) with at least two jets. For data the black bars show the statistical uncertainty and the hashed area shows the total uncertainty. A break down of the uncertainty for each bin is shown in the right plots with sources defined in section 3.9. The measurement is compared to NLO MG5_aMC, LO MG5_aMC, and GENEVA. The uncertainty for predictions is shown only in the ratio plots with statistical, PDF, and scale uncertainties for the NLO MG5_aMC and statistical only for the GENEVA and LO MG5_aMC predictions.

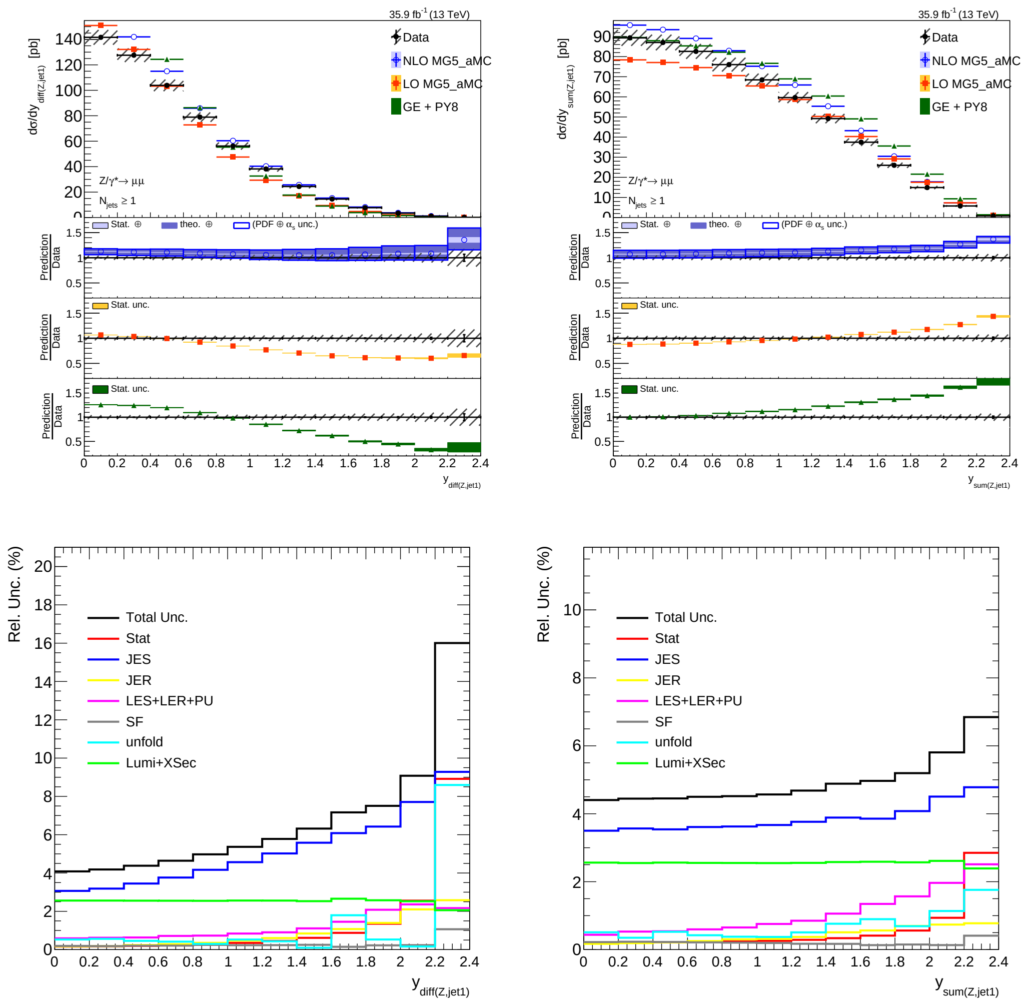

Figure 3·39: The measured differential cross section as a function of the Z boson and leading jet rapidity difference(left) and sum(right) with at least one jet. For data the black bars show the statistical uncertainty and the hashed area shows the total uncertainty. A break down of the uncertainty for each bin is shown in the right plots with sources defined in section 3.9. The measurement is compared to NLO MG5_aMC, LO MG5_aMC, and GENEVA. The uncertainty for predictions is shown only in the ratio plots with statistical, PDF, and scale uncertainties for the NLO MG5_aMC and statistical only for the GENEVA and LO MG5_aMC predictions.

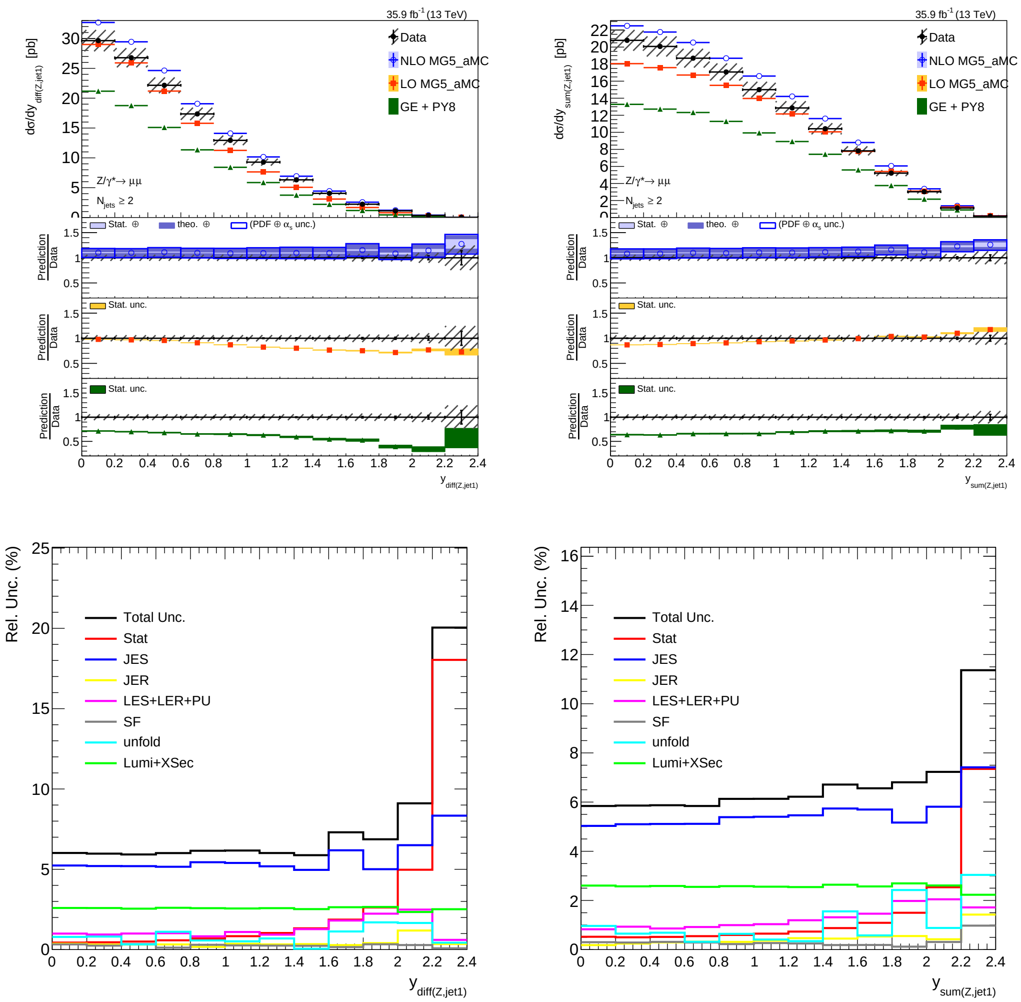

Figure 3·40: The measured differential cross section as a function of the Z boson and leading jet rapidity difference(left) and sum(right) with at least two jets. For data the black bars show the statistical uncertainty and the hashed area shows the total uncertainty. A break down of the uncertainty for each bin is shown in the right plots with sources defined in section 3.9. The measurement is compared to NLO MG5_AMC, LO MG5_AMC, and GENEVA. The uncertainty for predictions is shown only in the ratio plots with statistical, PDF, and scale uncertainties for the NLO MG5_AMC and statistical only for the GENEVA and LO MG5_AMC predictions.

Overall the MG5_aMC predictions at NLO coupled with parton showering describes the data within theoretical uncertainties over a wide variety of kinematics. Adding in higher order terms, both in the hard scattering and resummation, does not show significant improvement, and in some cases has worse agreement. The JES uncertainty is on par with the luminosity uncertainty at the 3% range and in many regions the total uncertainty in data is smaller than the theoretical uncertainty.

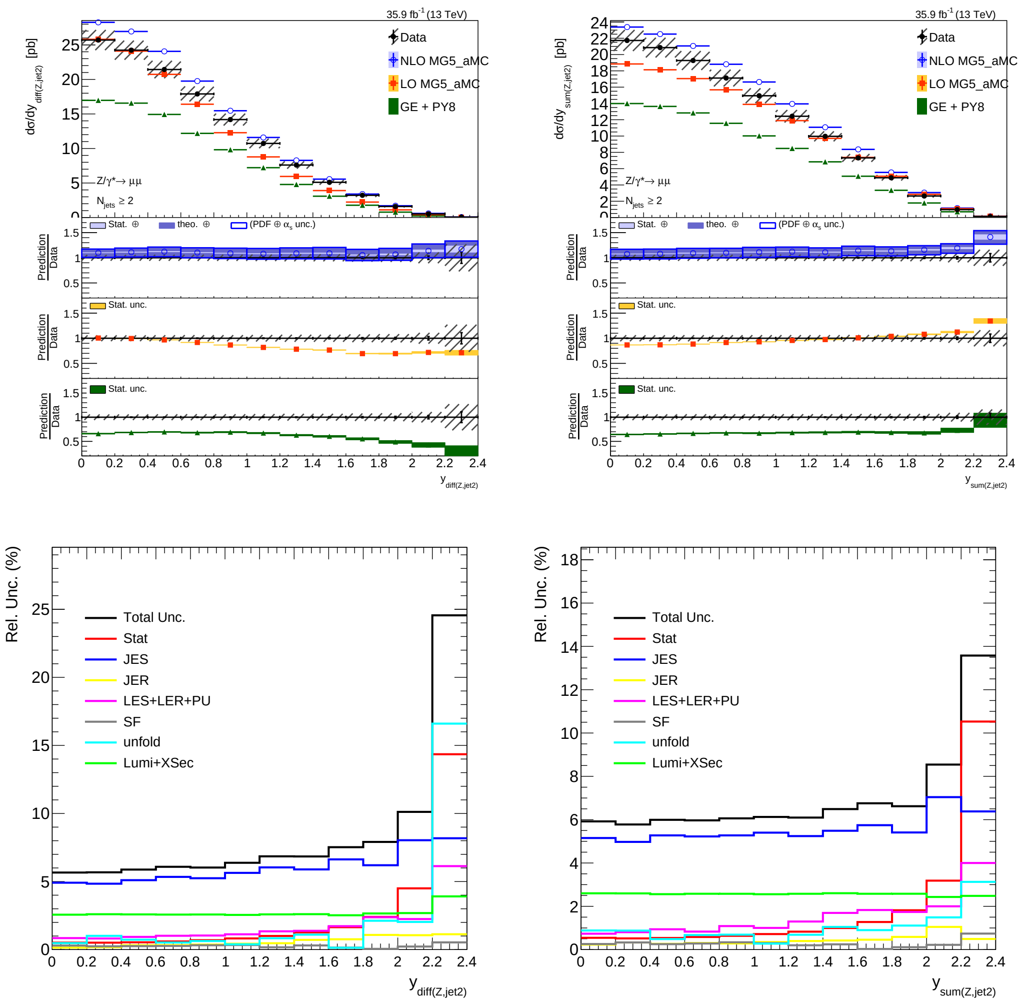

Figure 3·41: The measured differential cross section as a function of the Z boson and subleading jet rapidity difference(left) and sum(right) with at least two jets. For data the black bars show the statistical uncertainty and the hashed area shows the total uncertainty. A break down of the uncertainty for each bin is shown in the right plots with sources defined in section 3.9. The measurement is compared to NLO MG5_aMC, LO MG5_aMC, and GENEVA. The uncertainty for predictions is shown only in the ratio plots with statistical, PDF, and scale uncertainties for the NLO MG5_aMC and statistical only for the GENEVA and LO MG5_aMC predictions.

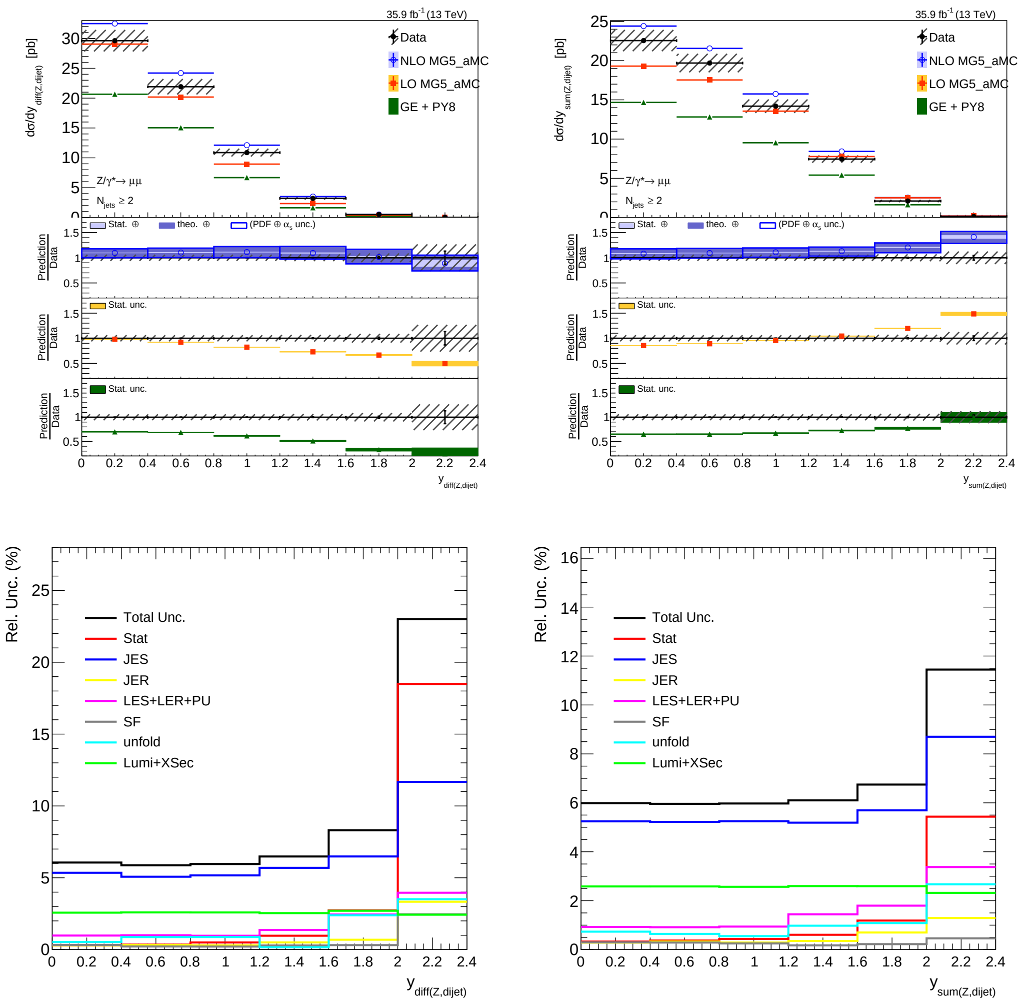

Figure 3·42: The measured differential cross section as a function of the Z boson and dijet rapidity difference(left) and sum(right) with two jets inclusive. For data the black bars show the statistical uncertainty and the hashed area shows the total uncertainty. A break down of the uncertainty for each bin is shown in the right plots with sources defined in section 3.9. The measurement is compared to NLO MG5_aMC, LO MG5_aMC, and GENEVA. The uncertainty for predictions is shown only in the ratio plots with statistical, PDF, and scale uncertainties for the NLO MG5_aMC and statistical only for the GENEVA and LO MG5_aMC predictions.

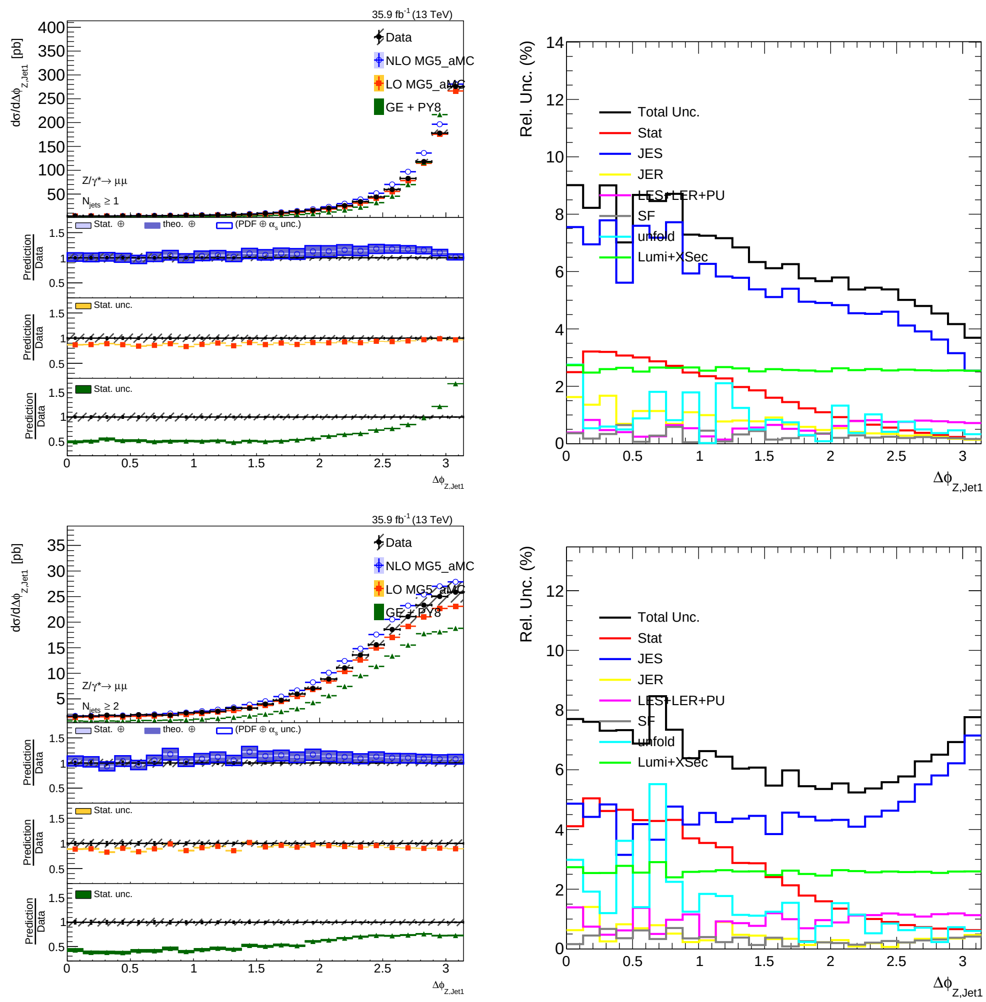

Figure 3·43: The measured differential cross section as a function of the Z boson and leading jet azimuthal difference with at least one (left), and two (right) jets. For data the black bars show the statistical uncertainty and the hashed area shows the total uncertainty. A break down of the uncertainty for each bin is shown in the right plots with sources defined in section 3.9. The measurement is compared to NLO MG5_aMC and LO MG5_aMC. The measurements with at least one and two jets is also compared to GENEVA. The uncertainty for predictions is shown only in the ratio plots with statistical, PDF, and scale uncertainties for the NLO MG5_aMC and statistical only for the GENEVA and LO MG5_aMC predictions.

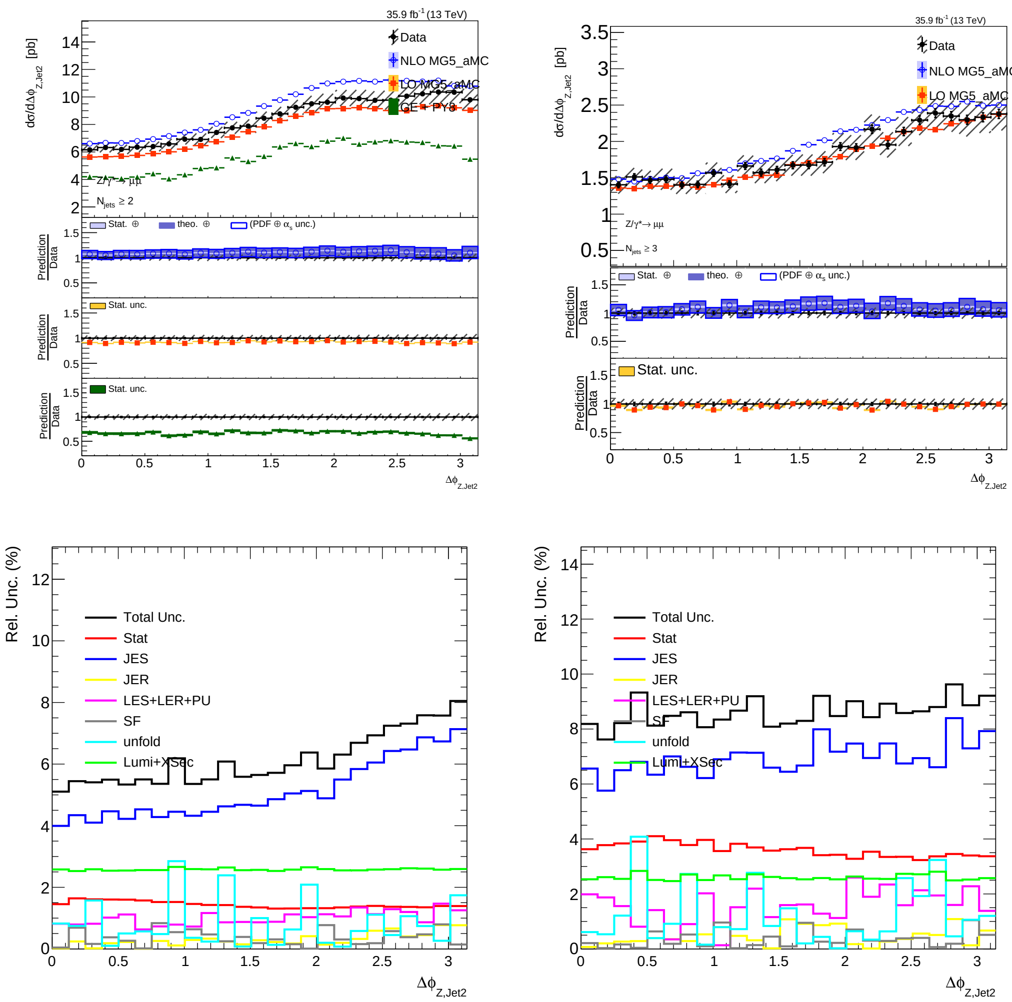

Figure 3·44: The measured differential cross section as a function of the Z boson and subleading jet azimuthal difference with at least two(left) and three(right) jets. For data the black bars show the statistical uncertainty and the hashed area shows the total uncertainty. A break down of the uncertainty for each bin is shown in the right plots with sources defined in section 3.9. The measurement is compared to NLO MG5_aMC and LO MG5_aMC. The measurement with at least two jets is also compared to GENEVA. The uncertainty for predictions is shown only in the ratio plots with statistical, PDF, and scale uncertainties for the NLO MG5_aMC and statistical only for the GENEVA and LO MG5_aMC predictions.

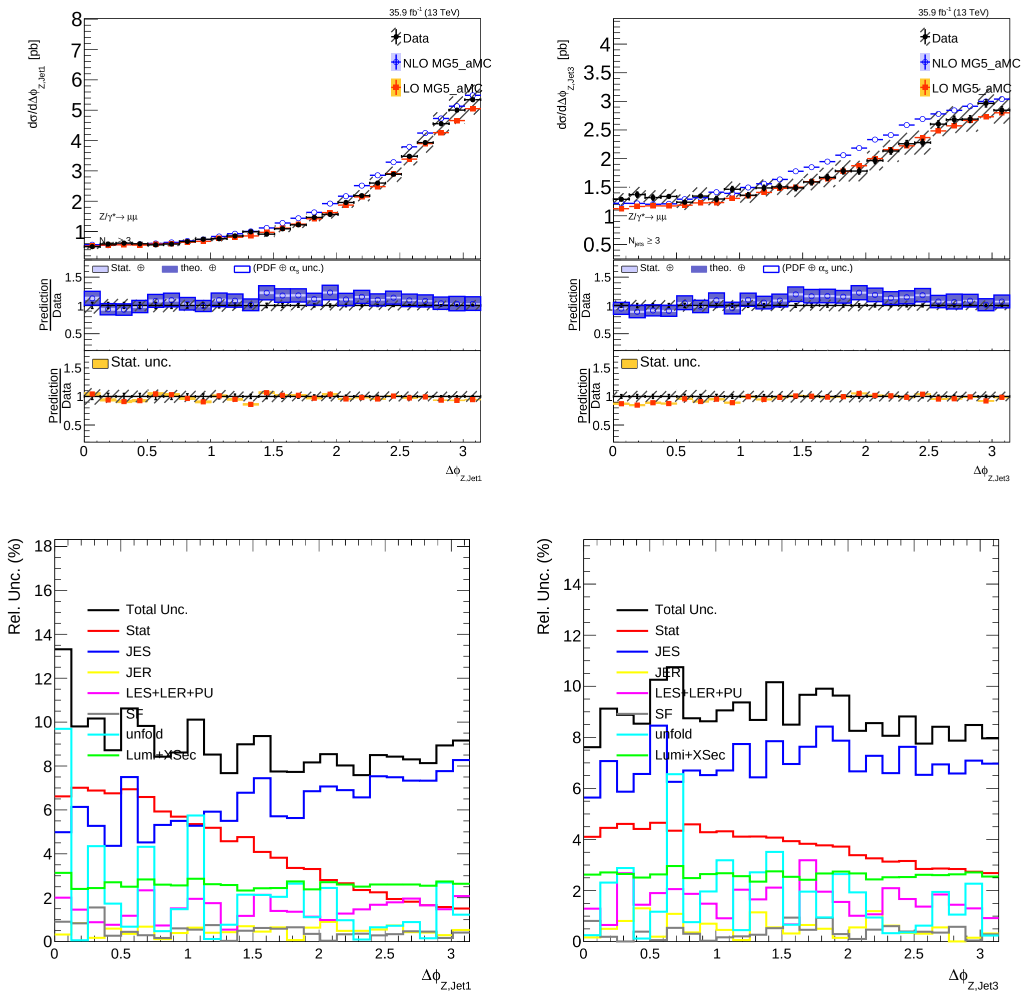

Figure 3·45: The measured differential cross section as a function of the Z boson and first (left) and third (right) jet azimuthal difference with at least three jets. For data the black bars show the statistical uncertainty and the hashed area shows the total uncertainty. A break down of the uncertainty for each bin is shown in the right plots with sources defined in section 3.9. The measurement is compared to NLO MG5_aMC and LO MG5_aMC. The uncertainty for predictions is shown only in the ratio plots with statistical, PDF, and scale uncertainties for the NLO MG5_aMC and statistical only for the LO MG5_aMC predictions.

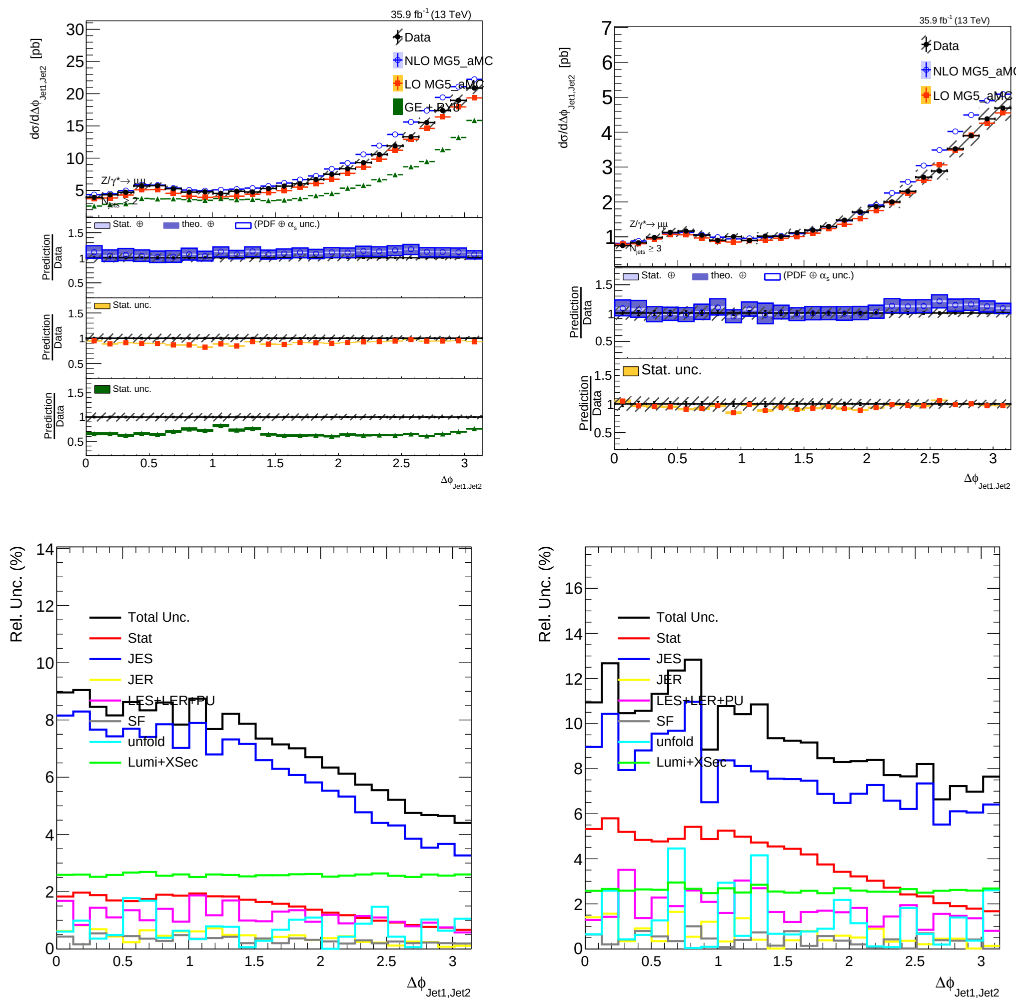

Figure 3·46: The measured differential cross section as a function of the leading and subleading jet azimuthal difference with at least two(left) and three(right) jets. For data the black bars show the statistical uncertainty and the hashed area shows the total uncertainty. A break down of the uncertainty for each bin is shown in the right plots with sources defined in section 3.9. The measurement is compared to NLO MG5_aMC and LO MG5_aMC. The measurement with at least two jets is also compared to GENEVA. The uncertainty for predictions is shown only in the ratio plots with statistical, PDF, and scale uncertainties for the NLO MG5_aMC and statistical only for the GENEVA and LO MG5_aMC predictions.

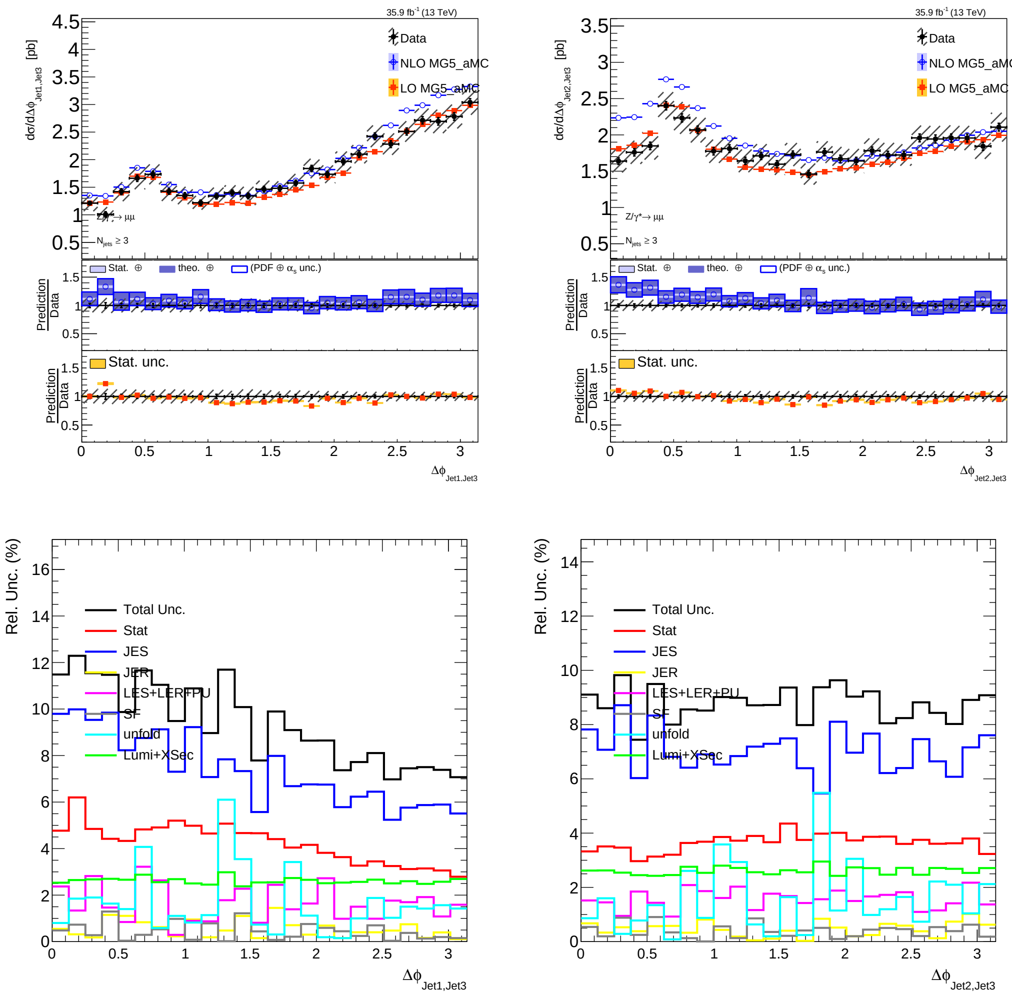

Figure 3·47: The measured differential cross section as a function of the leading and third jet azimuthal difference(left) and subleading and third jet azimuthal difference(right) with at least three jets. For data the black bars show the statistical uncertainty and the hashed area shows the total uncertainty. A break down of the uncertainty for each bin is shown in the right plots with sources defined in section 3.9. The measurement is compared to NLO MG5_aMC and LO MG5_aMC. The uncertainty for predictions is shown only in the ratio plots with statistical, PDF, and scale uncertainties for the NLO MG5_aMC and statistical only for the LO MG5_aMC predictions.

Chapter 4

Conclusions

With the strong performance of the HCAL DAQ, lead by the AMC13, the CMS detector collected a substantial data set at 13 TeV in 2016. With the numerous Z boson events, differential cross sections are measured for a Z boson decaying to muons with $p_{\mathrm{T}} > 30\,\mathrm{GeV}$ and $|\eta| < 2.4$ with at least one jet with $p_{\mathrm{T}} > 30\,\mathrm{GeV}$ and $|\eta| < 2.4$. The cross section are measured as functions of the exclusive and inclusive jet multiplicities up to 8, of the transverse momentum of the Z boson, jet kinematic variables including jet transverse momenta, the scalar sum of jet transverse momenta, and the jet rapidity for inclusive jet multiplicities up to five jets.

We reach the systematic limit of the CMS detector up to 600 GeV for the leading jet transverse momentum compared to 350 GeV in 2015 and reduced the jet energy scale uncertainty by a factor of 2 to $\sim 3\%$. All distributions have been extended to higher energies, including the leading jet and Z transverse momentum, which extends to 1500 and 1300 GeV, respectively, compared to 400 and 1000 GeV in 2015. Lastly, double differential cross sections are measured as functions of leading jet p_{T} and y, leading jet and $y(Z)$, $p_{\mathrm{T}}(Z)$ and y for the first time at 13TeV.

In order to relate these measurements to the strong interaction and progress the understanding of the theory, LO MG5_aMC, NLO MG5_aMC, and the NNLO GENEVA program are compared to the unfolded data. Overall, the NLO MG5_aMC has proved to be a powerful model in describing a wide range of phenomena at the LHC including the high energy jets and high multiplicity events. The strategy of GENEVA to incorporate NNLL resummation to account for low Q^2 phenomena shows promise in the low energy Z p_T zero jets inclusive spectrum. More work must be done to resolve the discrepancies with GENEVA in the Z p_T with at least one jet especially around the jet cut of 30 GeV where the parton shower from Pythia performs better.

The calculations predict the data within uncertainty for almost all variables. The theoretical uncertainties, however, are in many cases larger than the total uncertainty in data. As we look towards future runs, experimental uncertainties will improve and the theoretical uncertainties must follow suit to provide useful predictions. Adding higher order hard scattering terms, like GENEVA at NNLO, should lower the dependence on scales such as μ_R. As seen in [Sirunyan et al. (2018)], even at NNLO the theoretical predictions are of the same order as the NLO calculations and points towards a limit with adding higher order terms.

In summary, we made the most precise measurements of the Z in association with jets at 13 TeV with the CMS experiment, using data sets corresponding to an integrated luminosity of 35.9 fb^{-1}. The measured cross sections are generally described well by the predictions within the experimental and theoretical uncertainties. The Standard Model, specifically QCD in both the strongly coupled and perturbative regimes, accurately predicts a wide range of phenomena at the LHC.

Appendix A

Appendix

A.1 Systematic Tables

Table A.1: Differential cross section in 1st jet $|\eta|$ ($N_{\text{jets}} \geq 1$) and break down of the systematic uncertainties for the muon decay channel.

$\lvert y(j_1)\rvert$	$\frac{d\sigma}{d\lvert y(j_1)\rvert}$ [pb]	Tot. Unc [%]	stat [%]	JES [%]	JER [%]	Eff [%]	Lumi [%]	XSec [%]	PU [%]	LES+LER [%]	Unf sys [%]
0 – 0.2	64.9	4.0	0.24	3.0	0.029	0.18	2.6	0.031	0.42	0.028	0.52
0.2 – 0.4	65.2	4.0	0.23	3.0	0.028	0.18	2.6	0.027	0.40	0.041	0.46
0.4 – 0.6	64.2	4.0	0.23	3.0	0.068	0.20	2.6	0.027	0.42	0.038	0.43
0.6 – 0.8	61.9	4.1	0.24	3.1	0.11	0.18	2.6	0.029	0.35	0.040	0.53
0.8 – 1	58.7	3.9	0.25	2.9	0.12	0.20	2.6	0.026	0.41	0.033	0.39
1 – 1.2	55.2	4.8	0.26	4.0	0.27	0.21	2.6	0.027	0.41	0.056	0.39
1.2 – 1.4	51.2	5.0	0.28	4.2	0.24	0.23	2.5	0.033	0.55	0.053	0.51
1.4 – 1.6	44.3	5.0	0.31	4.1	0.20	0.22	2.6	0.039	0.88	0.029	0.67
1.6 – 1.8	39.6	4.8	0.34	3.8	0.50	0.22	2.6	0.024	1.3	0.030	0.33
1.8 – 2	35.8	5.3	0.36	4.2	0.93	0.20	2.6	0.043	1.6	0.074	0.78
2 – 2.2	31.4	6.3	0.40	5.4	1.1	0.22	2.6	0.036	1.6	0.057	0.59
2.2 – 2.4	24.6	8.2	0.52	7.2	1.6	0.32	2.6	0.026	2.2	0.043	0.27

Table A.2: Differential cross section in 1st jet p_{T} ($N_{\text{jets}} \geq 1$) and break down of the systematic uncertainties for the muon decay channel.

$p_{\text{T}}(j_1)$ [GeV]	$\frac{d\sigma}{dp_{\text{T}}(j_1)}$ [$\frac{\text{pb}}{\text{GeV}}$]	Tot. Unc [%]	stat [%]	JES [%]	JER [%]	Eff [%]	Lumi [%]	XSec [%]	PU [%]	LES+LER [%]	Unf sys [%]
30 – 47	3.30	3.7	0.21	2.6	0.22	0.15	2.5	0.018	0.51	0.035	0.55
47 – 69	1.44	3.6	0.26	2.5	0.086	0.22	2.6	0.026	0.53	0.030	0.37
69 – 96	0.609	4.0	0.35	3.0	0.16	0.035	2.6	0.026	0.26	0.043	0.59
96 – 128	0.253	4.1	0.50	3.0	0.11	0.13	2.6	0.041	0.37	0.026	0.81
128 – 166	0.107	3.9	0.70	2.6	0.12	0.063	2.6	0.044	0.28	0.045	0.99
166 – 210	0.0466	4.4	0.98	3.3	0.20	0.13	2.6	0.029	0.32	0.052	0.47
210 – 261	0.0191	4.5	1.4	2.5	0.035	0.026	2.7	0.081	0.052	0.11	1.9
261 – 319	0.00857	5.3	1.9	3.2	0.055	0.14	2.7	0.090	0.64	0.085	1.9
319 – 386	0.00355	5.8	2.9	2.9	0.29	0.053	2.7	0.094	0.22	0.22	2.3
386 – 460	0.00157	7.1	4.1	4.0	0.079	0.37	2.5	0.0087	0.55	0.087	0.17
460 – 544	0.000640	11.	6.4	1.9	0.0015	0.31	2.9	0.22	0.18	0.35	6.1
544 – 638	0.000304	13.	9.2	5.7	0.25	0.58	2.3	0.080	0.19	0.52	3.1
638 – 751	0.000129	16.	13.	2.3	0.85	0.14	2.7	0.096	0.29	0.41	2.5
751 – 870	5.48e-05	23.	18.	7.6	0.18	0.18	2.5	0.020	0.097	0.21	1.4
870 – 1500	9.60e-06	20.	16.	6.6	0.17	0.58	2.6	0.066	0.25	0.15	0.41

Table A.3: Differential cross section in 2[nd] jet $|\eta|$ ($N_{\text{jets}} \geq 2$) and break down of the systematic uncertainties for the muon decay channel.

$\lvert y(j_2)\rvert$	$\frac{d\sigma}{d\lvert y(j_2)\rvert}$ [pb]	Tot. Unc [%]	stat [%]	JES [%]	JER [%]	Eff [%]	Lumi [%]	XSec [%]	PU [%]	LES+LER [%]	Unf sys [%]
0 – 0.2	13.6	5.4	0.71	4.5	0.082	0.25	2.6	0.058	0.48	0.092	1.1
0.2 – 0.4	13.8	5.2	0.71	4.3	0.13	0.22	2.6	0.040	0.69	0.025	0.68
0.4 – 0.6	13.6	5.3	0.71	4.4	0.12	0.24	2.6	0.039	0.64	0.063	0.76
0.6 – 0.8	13.2	5.3	0.73	4.3	0.12	0.22	2.6	0.060	0.63	0.061	1.1
0.8 – 1	12.7	5.4	0.75	4.6	0.17	0.30	2.6	0.035	0.49	0.068	0.34
1 – 1.2	11.9	6.3	0.79	5.6	0.32	0.29	2.6	0.026	0.83	0.11	0.38
1.2 – 1.4	11.3	6.7	0.84	6.1	0.26	0.34	2.6	0.033	0.62	0.065	0.37
1.4 – 1.6	9.92	6.7	0.94	5.8	0.17	0.29	2.6	0.057	1.2	0.14	1.1
1.6 – 1.8	9.25	6.3	0.98	5.3	0.33	0.37	2.6	0.042	1.7	0.12	0.51
1.8 – 2	8.47	7.2	1.0	6.1	0.97	0.25	2.6	0.056	2.1	0.054	1.3
2 – 2.2	7.88	8.1	1.1	7.2	1.1	0.29	2.5	0.012	2.1	0.16	0.035
2.2 – 2.4	6.56	9.6	1.4	8.5	1.2	0.24	2.6	0.038	3.1	0.11	0.33

Table A.4: Differential cross section in 2[nd] jet p_{T} ($N_{\text{jets}} \geq 2$) and break down of the systematic uncertainties for the muon decay channel.

$p_{\text{T}}(j_2)$ [GeV]	$\frac{d\sigma}{dp_{\text{T}}(j_2)}$ $[\frac{\text{pb}}{\text{GeV}}]$	Tot. Unc [%]	stat [%]	JES [%]	JER [%]	Eff [%]	Lumi [%]	XSec [%]	PU [%]	LES+LER [%]	Unf sys [%]
30 – 47	0.871	4.3	0.45	3.3	0.33	0.23	2.5	0.021	0.54	0.079	0.71
47 – 69	0.291	4.9	0.60	4.0	0.079	0.36	2.6	0.043	0.79	0.057	0.72
69 – 96	0.103	4.5	0.88	3.4	0.27	0.041	2.6	0.039	0.24	0.12	0.82
96 – 129	0.0390	5.0	1.2	3.5	0.26	0.32	2.6	0.075	0.69	0.20	1.5
129 – 168	0.0157	4.8	1.8	2.6	0.0085	0.059	2.6	0.076	0.30	0.040	2.0
168 – 212	0.00642	5.4	2.6	3.4	0.19	0.36	2.5	0.017	0.28	0.089	0.92
212 – 265	0.00293	6.5	3.4	3.2	0.29	0.065	2.7	0.11	0.55	0.26	2.4
265 – 323	0.00105	9.3	6.1	3.3	1.0	0.52	2.2	0.14	0.94	0.32	3.4
323 – 392	0.000614	9.6	6.4	1.7	0.58	0.033	2.9	0.20	0.38	0.13	4.1
392 – 469	0.000200	15.	11.	6.6	0.78	0.25	2.4	0.070	0.96	0.31	1.8
469 – 600	8.98e-05	13.	9.8	0.60	0.36	0.12	2.5	0.023	0.78	0.13	1.4
600 – 1350	9.97e-06	15.	11.	4.7	0.13	0.59	2.5	0.011	0.64	0.47	0.91

Table A.5: Differential cross section in 3$^{\text{rd}}$ jet $|\eta|$ ($N_{\text{jets}} \geq 3$) and break down of the systematic uncertainties for the muon decay channel.

$\|y(j_3)\|$	$\frac{d\sigma}{d\|y(j_3)\|}$ [pb]	Tot. Unc [%]	stat [%]	JES [%]	JER [%]	Eff [%]	Lumi [%]	XSec [%]	PU [%]	LES+LER [%]	Unf sys [%]
0 – 0.2	3.06	6.8	1.8	5.7	0.13	0.15	2.5	0.020	1.6	0.096	0.35
0.2 – 0.4	3.07	7.1	1.8	5.7	0.043	0.064	2.7	0.11	0.86	0.25	2.4
0.4 – 0.6	3.00	7.0	1.8	6.0	0.065	0.46	2.6	0.049	1.2	0.16	0.64
0.6 – 0.8	2.76	7.8	1.9	6.8	0.20	0.66	2.5	0.0031	1.2	0.29	0.72
0.8 – 1	2.73	7.6	1.9	6.5	0.37	0.39	2.6	0.069	0.73	0.092	1.7
1 – 1.2	2.64	8.1	2.0	7.1	0.37	0.26	2.6	0.055	1.0	0.49	1.1
1.2 – 1.4	2.52	8.8	2.1	7.9	0.46	0.33	2.6	0.029	1.1	0.036	0.64
1.4 – 1.6	2.04	9.5	2.5	8.0	0.14	0.23	2.7	0.12	1.6	0.84	2.5
1.6 – 1.8	1.94	8.5	2.5	6.9	1.2	0.51	2.6	0.057	2.2	0.29	0.62
1.8 – 2	1.92	9.0	2.5	7.5	1.3	0.36	2.6	0.026	2.5	0.079	0.21
2 – 2.2	1.67	11.	2.8	8.9	0.92	0.35	2.7	0.092	3.1	0.18	1.7
2.2 – 2.4	1.29	15.	3.6	13.	2.4	0.35	2.6	0.049	3.9	0.64	0.79

Table A.6: Differential cross section in 3$^{\text{rd}}$ jet p_{T} ($N_{\text{jets}} \geq 3$) and break down of the systematic uncertainties for the muon decay channel.

$p_{\text{T}}(j_3)$ [GeV]	$\frac{d\sigma}{dp_{\text{T}}(j_3)}$ [$\frac{\text{pb}}{\text{GeV}}$]	Tot. Unc [%]	stat [%]	JES [%]	JER [%]	Eff [%]	Lumi [%]	XSec [%]	PU [%]	LES+LER [%]	Unf sys [%]
30 – 48	0.206	5.4	0.95	4.3	0.59	0.095	2.6	0.034	0.80	0.11	1.1
48 – 71	0.0538	6.3	1.4	5.2	0.31	0.18	2.6	0.061	0.82	0.17	1.0
71 – 101	0.0140	6.1	2.3	4.0	0.44	0.11	2.7	0.091	0.92	0.070	2.1
101 – 138	0.00405	7.2	3.6	4.7	0.21	0.054	2.6	0.045	1.1	0.24	0.94
138 – 181	0.00107	9.3	6.3	3.6	0.044	0.10	2.6	0.041	0.13	0.18	1.3
181 – 250	0.000303	12.	8.3	4.2	0.28	0.091	2.6	0.054	0.59	0.32	1.1
250 – 650	1.93e-05	16.	12.	4.7	0.66	0.38	2.5	0.0020	0.032	0.75	0.051

Table A.7: Differential cross section in 4^{th} jet $|\eta|$ ($N_{\text{jets}} \geq 4$) and break down of the systematic uncertainties for the muon decay channel.

$\lvert y(j_4)\rvert$	$\frac{d\sigma}{d\lvert y(j_4)\rvert}$ [pb]	Tot. Unc [%]	stat [%]	JES [%]	JER [%]	Eff [%]	Lumi [%]	XSec [%]	PU [%]	LES+LER [%]	Unf sys [%]
0 – 0.2	0.679	9.8	4.4	7.5	0.26	0.14	2.6	0.044	0.40	0.80	1.1
0.2 – 0.4	0.645	10.	4.7	7.4	0.46	0.027	2.4	0.044	1.3	0.73	1.1
0.4 – 0.6	0.693	9.8	4.4	7.4	0.73	0.67	2.6	0.064	1.4	0.68	0.13
0.6 – 0.8	0.656	9.4	4.6	6.7	0.38	0.44	2.5	0.0083	1.2	0.61	0.40
0.8 – 1	0.690	9.4	4.5	6.8	0.092	0.62	2.6	0.038	1.9	0.097	0.32
1 – 1.2	0.633	10.	5.0	7.4	0.045	0.56	2.6	0.045	1.7	0.82	0.39
1.2 – 1.4	0.553	13.	5.4	10.	0.55	0.039	2.5	0.020	2.6	0.70	0.72
1.4 – 1.6	0.470	14.	6.1	10.	0.48	0.40	2.5	0.0015	3.6	0.49	0.93
1.6 – 1.8	0.403	16.	6.8	9.7	0.46	0.89	3.0	0.29	5.8	1.3	6.5
1.8 – 2	0.440	13.	6.6	8.0	2.5	0.46	2.8	0.15	1.2	0.49	3.3
2 – 2.2	0.417	17.	6.8	13.	2.3	0.84	2.9	0.18	2.5	1.4	4.5
2.2 – 2.4	0.315	19.	9.5	13.	0.50	0.21	2.3	0.082	5.4	2.7	1.4

Table A.8: Differential cross section in 4^{th} jet p_{T} ($N_{\text{jets}} \geq 4$) and break down of the systematic uncertainties for the muon decay channel.

$p_{\text{T}}(j_4)$ [GeV]	$\frac{d\sigma}{dp_{\text{T}}(j_4)}$ [$\frac{\text{pb}}{\text{GeV}}$]	Tot. Unc [%]	stat [%]	JES [%]	JER [%]	Eff [%]	Lumi [%]	XSec [%]	PU [%]	LES+LER [%]	Unf sys [%]
30 – 49	0.0490	6.3	2.0	5.1	0.32	0.38	2.5	0.012	0.76	0.34	0.43
49 – 75	0.00877	8.5	3.4	5.5	0.017	0.33	2.8	0.15	2.0	0.52	3.5
75 – 109	0.00186	9.9	5.7	6.0	0.33	0.15	2.4	0.046	1.3	0.56	1.7
109 – 153	0.000290	18.	14.	3.1	1.1	0.29	2.6	0.061	0.56	1.7	3.1
153 – 500	1.31e-05	25.	18.	6.8	0.39	0.24	2.5	0.015	5.6	2.7	0.92

Table A.9: Differential cross section in H_T ($N_\mathrm{jets} \geq 1$) and break down of the systematic uncertainties for the muon decay channel.

H_T [GeV]	$\frac{d\sigma}{dH_\mathrm{T}}$ [$\frac{\mathrm{pb}}{\mathrm{GeV}}$]	Tot. Unc [%]	stat [%]	JES [%]	JER [%]	Eff [%]	Lumi [%]	XSec [%]	PU [%]	LES+LER [%]	Unf sys [%]
30 – 43	3.15	7.2	0.24	6.4	0.82	0.61	2.6	0.034	1.6	0.059	0.18
43 – 68	1.32	2.7	0.27	0.51	0.13	0.089	2.5	0.020	0.049	0.034	0.50
68 – 107	0.571	5.0	0.32	4.2	0.32	0.14	2.6	0.030	0.65	0.033	0.61
107 – 153	0.234	4.1	0.47	3.0	0.14	0.064	2.6	0.029	0.48	0.029	0.54
153 – 206	0.103	4.8	0.66	3.9	0.092	0.15	2.6	0.036	0.41	0.049	0.67
206 – 266	0.0462	4.9	0.93	3.8	0.39	0.10	2.6	0.049	0.57	0.053	1.1
266 – 333	0.0223	5.1	1.2	3.7	0.12	0.068	2.6	0.068	0.50	0.12	1.6
333 – 407	0.0108	5.4	1.7	3.9	0.24	0.12	2.6	0.067	0.65	0.088	1.4
407 – 488	0.00539	5.8	2.3	4.1	0.25	0.054	2.6	0.056	0.27	0.25	1.2
488 – 577	0.00294	5.8	2.9	2.5	0.26	0.11	2.7	0.11	0.84	0.38	2.5
577 – 674	0.00140	8.1	4.3	4.8	0.42	0.014	2.7	0.086	0.10	0.36	2.2
674 – 784	0.000901	7.5	4.8	3.2	0.38	0.36	2.4	0.031	1.3	0.19	1.2
784 – 896	0.000416	11.	7.5	4.9	1.2	0.087	2.5	0.0070	0.92	0.61	0.54
896 – 1014	0.000262	12.	8.3	3.5	0.087	0.12	2.8	0.15	1.7	0.39	4.3
1014 – 1141	0.000116	18.	13.	7.5	0.33	0.28	2.4	0.067	1.6	0.50	2.3
1141 – 1500	5.76e-05	9.8	6.7	3.0	0.21	0.39	2.5	0.025	2.1	0.54	0.33

Table A.10: Differential cross section in H_T ($N_\mathrm{jets} \geq 2$) and break down of the systematic uncertainties for the muon decay channel.

H_T [GeV]	$\frac{d\sigma}{dH_\mathrm{T}}$ [$\frac{\mathrm{pb}}{\mathrm{GeV}}$]	Tot. Unc [%]	stat [%]	JES [%]	JER [%]	Eff [%]	Lumi [%]	XSec [%]	PU [%]	LES+LER [%]	Unf sys [%]
60 – 90	0.195	13.	0.82	12.	1.4	0.85	2.6	0.069	2.8	0.11	0.73
90 – 125	0.197	4.6	0.69	3.6	0.017	0.16	2.5	0.014	0.75	0.097	0.24
125 – 169	0.123	5.4	0.74	4.6	0.28	0.17	2.6	0.044	0.71	0.10	0.61
169 – 221	0.0654	4.8	0.90	3.7	0.14	0.21	2.6	0.036	0.52	0.053	0.84
221 – 281	0.0338	5.2	1.1	4.1	0.16	0.14	2.6	0.044	0.74	0.062	0.85
281 – 349	0.0173	5.4	1.4	4.0	0.13	0.098	2.6	0.067	0.49	0.10	1.6
349 – 423	0.00876	5.4	2.0	3.5	0.053	0.28	2.7	0.085	0.48	0.028	1.8
423 – 504	0.00460	5.6	2.6	3.7	0.18	0.055	2.5	0.015	0.48	0.25	0.12
504 – 592	0.00258	7.5	3.2	3.7	0.13	0.14	2.8	0.17	1.2	0.13	4.2
592 – 686	0.00125	8.6	4.7	5.6	0.47	0.45	2.6	0.027	0.64	0.30	0.037
686 – 796	0.000863	7.0	4.8	1.7	0.31	0.093	2.4	0.057	1.7	0.54	1.2
796 – 913	0.000366	13.	8.0	8.2	0.76	0.12	2.7	0.10	1.6	0.90	1.7
913 – 1043	0.000221	12.	8.9	0.78	0.079	0.25	2.7	0.090	2.3	0.88	2.7
1043 – 1178	0.000116	17.	12.	7.8	0.22	0.022	2.4	0.040	1.7	1.4	0.90
1178 – 1500	4.82e-05	12.	7.9	4.9	0.11	0.64	2.5	0.025	2.8	0.50	0.49

Table A.11: Differential cross section in H_{T} ($N_{\mathrm{jets}} \geq 3$) and break down of the systematic uncertainties for the muon decay channel.

H_{T} [GeV]	$\frac{d\sigma}{dH_{\mathrm{T}}}$ [$\frac{\mathrm{pb}}{\mathrm{GeV}}$]	Tot. Unc [%]	stat [%]	JES [%]	JER [%]	Eff [%]	Lumi [%]	XSec [%]	PU [%]	LES+LER [%]	Unf sys [%]
90 – 141	0.0189	17.	2.4	16.	1.7	0.87	2.6	0.032	4.4	0.39	0.46
141 – 184	0.0284	8.3	1.9	7.3	0.14	0.49	2.5	0.0045	1.9	0.56	0.70
184 – 234	0.0228	8.6	1.8	7.3	0.76	0.31	2.7	0.082	1.5	0.32	2.2
234 – 292	0.0146	7.1	2.0	5.9	0.24	0.24	2.6	0.069	0.98	0.12	1.2
292 – 358	0.00939	7.0	2.2	5.7	0.20	0.030	2.6	0.036	0.97	0.27	0.81
358 – 430	0.00514	6.9	2.8	4.0	0.30	0.30	2.8	0.14	0.78	0.34	3.1
430 – 510	0.00311	7.3	3.3	5.4	0.25	0.083	2.5	0.0051	0.76	0.28	0.61
510 – 598	0.00179	8.6	4.0	4.1	0.45	0.065	2.8	0.17	1.2	0.14	4.7
598 – 692	0.000915	9.2	5.6	5.2	0.36	0.11	2.5	0.021	0.51	0.14	0.31
692 – 804	0.000652	8.5	5.6	3.6	0.69	0.27	2.4	0.032	1.7	0.20	0.59
804 – 917	0.000291	14.	9.5	6.1	1.1	0.069	2.6	0.031	0.26	0.37	0.40
917 – 1043	0.000185	14.	10.	0.31	1.1	0.081	2.8	0.16	1.4	0.66	4.9
1043 – 1175	9.97e-05	19.	13.	8.1	0.70	0.060	2.3	0.085	1.3	1.3	1.6
1175 – 1500	4.17e-05	13.	8.7	5.4	0.56	0.85	2.6	0.035	2.8	0.38	0.54

Table A.12: Differential cross section in dijet mass M_{jj} ($N_{\mathrm{jets}} \geq 2$) and break down of the systematic uncertainties for the muon decay channel.

M_{jj} [GeV]	$\frac{d\sigma}{dM_{jj}}$ [$\frac{\mathrm{pb}}{\mathrm{GeV}}$]	Tot. Unc [%]	stat [%]	JES [%]	JER [%]	Eff [%]	Lumi [%]	XSec [%]	PU [%]	LES+LER [%]	Unf sys [%]
20 – 46	0.0701	11.	1.5	10.	0.71	0.64	2.6	0.073	1.9	0.15	0.97
46 – 70	0.0968	9.6	1.1	8.9	0.71	0.66	2.6	0.034	1.6	0.10	0.27
70 – 98	0.153	8.1	0.85	7.4	0.58	0.51	2.6	0.038	1.6	0.11	0.60
98 – 133	0.143	5.5	0.75	4.6	0.11	0.21	2.6	0.055	0.98	0.048	1.0
133 – 178	0.101	5.2	0.76	4.4	0.39	0.19	2.5	0.0036	0.76	0.12	0.28
178 – 235	0.0597	5.3	0.86	4.3	0.17	0.13	2.6	0.056	0.63	0.043	1.2
235 – 305	0.0325	4.8	1.0	3.4	0.091	0.13	2.6	0.074	0.74	0.098	1.6
305 – 390	0.0163	5.7	1.3	4.4	0.33	0.13	2.6	0.073	0.77	0.064	1.7
390 – 489	0.00786	4.7	1.7	3.3	0.0064	0.17	2.6	0.036	0.52	0.073	0.63
489 – 607	0.00392	5.2	2.1	3.6	0.38	0.094	2.5	0.024	0.72	0.16	0.34
607 – 740	0.00183	5.5	2.9	3.2	0.055	0.043	2.5	0.018	0.89	0.32	0.48
740 – 886	0.000875	6.9	4.0	3.9	0.079	0.16	2.5	0.023	0.11	0.39	0.57
886 – 1056	0.000455	7.3	4.9	2.8	0.43	0.090	2.5	0.017	0.97	0.41	0.32
1056 – 1231	0.000186	11.	8.2	4.1	0.28	0.34	2.6	0.031	0.59	0.52	0.24
1231 – 1500	0.000123	10.	6.5	5.4	0.093	0.27	2.5	0.0034	0.89	0.63	0.37

Table A.13: Differential cross section in Exclusive jet multiplicity and break down of the systematic uncertainties for the muon decay channel.

N_{jets}	$\frac{d\sigma}{dN_{\text{jets}}}$ [pb]	Tot. Unc [%]	stat [%]	JES [%]	JER [%]	Eff [%]	Lumi [%]	XSec [%]	PU [%]	LES+LER [%]	Unf sys [%]
$= 0$	585.	2.7	0.028	0.77	0.087	0.019	2.5	0.019	0.061	0.030	0.41
$= 1$	92.2	4.6	0.11	3.7	0.35	0.099	2.5	0.023	0.63	0.036	0.44
$= 2$	20.9	4.9	0.28	4.0	0.20	0.048	2.6	0.032	0.75	0.034	0.69
$= 3$	4.38	6.3	0.75	5.5	0.42	0.079	2.6	0.053	1.1	0.037	1.2
$= 4$	1.02	7.7	1.9	6.6	0.16	0.12	2.5	0.017	1.9	0.22	0.78
$= 5$	0.227	9.5	5.1	6.4	0.75	0.94	2.6	0.069	1.0	0.79	0.81
$= 6$	0.0572	18.	12.	6.4	0.56	2.8	2.7	0.13	2.4	1.4	7.3
$= 7$	0.0131	40.	30.	15.	2.1	5.2	2.4	0.057	1.0	4.2	9.2
$= 8$	0.00250	51.	40.	8.3	4.8	2.3	2.5	0.018	6.7	4.5	7.6

Table A.14: Differential cross section in Inclusive jet multiplicity and break down of the systematic uncertainties for the muon decay channel.

N_{jets}	$\frac{d\sigma}{dN_{\text{jets}}}$ [pb]	Tot. Unc [%]	stat [%]	JES [%]	JER [%]	Eff [%]	Lumi [%]	XSec [%]	PU [%]	LES+LER [%]	Unf sys [%]
≥ 0	704.	2.6	0.024	0.0054	0.018	0.030	2.5	0.020	0.16	0.030	0.43
≥ 1	119.	4.7	0.082	3.8	0.32	0.088	2.6	0.026	0.68	0.035	0.51
≥ 2	26.6	5.2	0.20	4.4	0.24	0.050	2.6	0.036	0.85	0.032	0.77
≥ 3	5.71	6.5	0.51	5.7	0.38	0.060	2.6	0.047	1.2	0.021	1.1
≥ 4	1.32	7.5	1.2	6.6	0.27	0.0013	2.6	0.030	1.8	0.070	0.70
≥ 5	0.300	8.4	3.0	6.8	0.62	0.39	2.6	0.074	1.3	0.49	0.44
≥ 6	0.0728	13.	7.3	7.9	0.23	1.3	2.7	0.089	2.3	0.49	4.3
≥ 7	0.0156	31.	22.	14.	0.99	4.0	2.4	0.045	1.9	3.1	6.5
≥ 8	0.00250	51.	40.	8.3	4.8	2.3	2.5	0.018	6.7	4.5	7.6

Table A.15: Differential cross section in p_T^Z and break down of the systematic uncertainties for the muon decay channel.

$p_{\mathrm{T}}(Z)$ [GeV]	$\frac{d\sigma}{dp_{\mathrm{T}}(Z)}$ [$\frac{\mathrm{pb}}{\mathrm{GeV}}$]	Tot. Unc [%]	stat [%]	JES [%]	JER [%]	Eff [%]	Lumi [%]	XSec [%]	PU [%]	LES+LER [%]	Unf sys [%]
0.8 – 2	14.2	2.6	0.20	0.012	0.012	0.012	2.5	0.012	0.22	0.045	0.25
2 – 4	30.6	2.6	0.15	0.012	0.012	0.014	2.5	0.012	0.16	0.023	0.28
4 – 6	33.3	2.6	0.15	0.015	0.015	0.018	2.5	0.015	0.20	0.025	0.32
6 – 8	30.7	2.6	0.16	0.017	0.017	0.017	2.5	0.017	0.16	0.018	0.37
8 – 10	27.3	2.6	0.17	0.023	0.023	0.022	2.5	0.023	0.20	0.026	0.50
10 – 12	23.7	2.6	0.19	0.020	0.020	0.022	2.5	0.020	0.15	0.020	0.45
12 – 14	20.4	2.6	0.20	0.023	0.023	0.027	2.5	0.023	0.15	0.026	0.50
14 – 16	17.7	2.6	0.21	0.026	0.026	0.028	2.6	0.026	0.17	0.026	0.57
16 – 19	14.9	2.6	0.16	0.022	0.022	0.037	2.5	0.022	0.17	0.032	0.47
19 – 22	12.1	2.6	0.18	0.021	0.021	0.035	2.5	0.021	0.16	0.046	0.44
22 – 25	9.99	2.6	0.19	0.024	0.024	0.030	2.5	0.024	0.14	0.035	0.53
25 – 28	8.27	2.6	0.22	0.017	0.017	0.043	2.5	0.018	0.16	0.068	0.36
28 – 31	7.00	2.6	0.24	0.025	0.025	0.053	2.5	0.025	0.14	0.046	0.53
31 – 34	5.93	2.6	0.27	0.019	0.019	0.056	2.5	0.019	0.11	0.088	0.39
34 – 37	5.10	2.6	0.29	0.025	0.025	0.054	2.5	0.025	0.18	0.056	0.53
37 – 40	4.38	2.7	0.32	0.030	0.030	0.050	2.6	0.029	0.11	0.062	0.62
40 – 43	3.77	2.6	0.36	0.025	0.025	0.052	2.5	0.025	0.14	0.075	0.53
43 – 46	3.34	2.6	0.39	0.024	0.024	0.070	2.5	0.023	0.089	0.12	0.47
46 – 49	2.89	2.6	0.42	0.021	0.021	0.068	2.5	0.021	0.24	0.061	0.41
49 – 53	2.51	2.7	0.35	0.031	0.031	0.060	2.6	0.031	0.15	0.082	0.66
53 – 57	2.13	2.6	0.39	0.014	0.014	0.072	2.5	0.014	0.16	0.14	0.25
57 – 61	1.82	2.7	0.43	0.028	0.028	0.070	2.6	0.028	0.17	0.096	0.58
61 – 65	1.55	2.7	0.48	0.025	0.025	0.055	2.5	0.025	0.15	0.17	0.53
65 – 69	1.31	2.7	0.52	0.031	0.031	0.061	2.6	0.031	0.13	0.068	0.65
69 – 74	1.11	2.6	0.47	0.019	0.019	0.073	2.5	0.020	0.092	0.18	0.38
74 – 79	0.921	2.7	0.53	0.023	0.023	0.048	2.5	0.023	0.13	0.13	0.48
79 – 84	0.754	2.8	0.60	0.039	0.039	0.024	2.6	0.040	0.13	0.16	0.89
84 – 89	0.629	2.7	0.67	0.026	0.026	0.066	2.5	0.025	0.17	0.13	0.52
89 – 94	0.521	2.7	0.75	0.011	0.011	0.073	2.5	0.011	0.020	0.25	0.19
94 – 100	0.438	2.8	0.71	0.030	0.030	0.048	2.6	0.029	0.27	0.17	0.63
100 – 106	0.364	2.7	0.78	0.013	0.013	0.071	2.5	0.014	0.040	0.15	0.26
106 – 113	0.290	2.9	0.79	0.036	0.036	0.041	2.6	0.036	0.083	0.21	0.79
113 – 120	0.240	2.9	0.89	0.034	0.034	0.048	2.6	0.033	0.24	0.036	0.71
120 – 128	0.197	2.8	0.90	0.0097	0.0097	0.086	2.5	0.0092	0.094	0.32	0.30
128 – 136	0.161	3.1	1.0	0.052	0.052	0.016	2.6	0.050	0.0075	0.14	1.1
136 – 145	0.127	2.9	1.1	0.022	0.022	0.055	2.5	0.025	0.080	0.15	0.53
145 – 155	0.101	3.1	1.1	0.035	0.035	0.044	2.6	0.034	0.34	0.21	0.75
155 – 165	0.0781	3.1	1.3	0.029	0.029	0.043	2.6	0.028	0.028	0.27	0.61
165 – 177	0.0627	3.0	1.3	0.0067	0.0067	0.084	2.5	0.0033	0.080	0.18	0.16
177 – 190	0.0461	3.2	1.5	0.016	0.016	0.057	2.5	0.014	0.16	0.22	0.27
190 – 204	0.0354	3.3	1.7	0.019	0.019	0.065	2.5	0.021	0.24	0.40	0.43
204 – 220	0.0268	3.4	1.7	0.024	0.024	0.057	2.5	0.023	0.094	0.12	0.48
220 – 237	0.0184	3.9	2.1	0.050	0.050	0.028	2.6	0.050	0.23	0.43	1.1
237 – 256	0.0140	4.3	2.2	0.084	0.083	0.022	2.7	0.079	0.24	0.27	1.9
256 – 277	0.00937	4.3	2.6	0.034	0.034	0.054	2.6	0.036	0.039	0.26	0.73
277 – 301	0.00677	4.4	2.9	0.0054	0.0054	0.069	2.5	0.0051	0.20	0.60	0.061
301 – 328	0.00453	4.9	3.3	0.010	0.010	0.072	2.5	0.011	0.027	0.067	0.18
328 – 359	0.00277	5.9	4.0	0.050	0.050	0.041	2.6	0.049	0.27	0.75	1.1
359 – 394	0.00201	6.1	4.1	0.069	0.068	0.038	2.6	0.063	0.58	0.47	1.6
394 – 433	0.00107	7.5	5.5	0.044	0.043	0.11	2.4	0.038	0.47	0.067	1.1
433 – 483	0.000689	8.5	5.6	0.14	0.14	0.060	2.7	0.13	0.74	1.6	3.2
483 – 537	0.000336	11.	8.1	0.0061	0.0062	0.081	2.5	0.0065	1.3	0.39	0.10
537 – 608	0.000186	12.	9.2	0.0067	0.0067	0.13	2.5	0.0070	0.55	2.5	0.041
608 – 700	8.01e-05	15.	12.	0.012	0.012	0.17	2.5	0.012	0.20	0.45	0.14
700 – 1300	1.14e-05	13.	9.9	0.011	0.011	0.24	2.5	0.011	1.1	0.78	0.029

Table A.16: Differential cross section in p_T^Z and break down of the systematic uncertainties for the muon decay channel.

$p_{\mathrm{T}}(Z)$ [GeV]	$\frac{d\sigma}{dp_{\mathrm{T}}(Z)}$ [$\frac{\mathrm{pb}}{\mathrm{GeV}}$]	Tot. Unc [%]	stat [%]	JES [%]	JER [%]	Eff [%]	Lumi [%]	XSec [%]	PU [%]	LES+LER [%]	Unf sys [%]
0.8 – 2	0.0737	26.	4.1	25.	4.0	1.3	2.6	0.065	2.8	0.55	0.82
2 – 4	0.204	19.	1.6	19.	2.5	0.74	2.6	0.053	0.50	0.24	0.52
4 – 6	0.324	15.	1.1	14.	2.2	0.47	2.6	0.038	0.21	0.16	0.36
6 – 8	0.426	12.	0.88	12.	1.8	0.40	2.6	0.051	0.18	0.14	0.65
8 – 10	0.514	11.	0.77	11.	1.4	0.41	2.6	0.062	0.40	0.30	0.92
10 – 12	0.595	11.	0.69	11.	1.3	0.43	2.6	0.051	0.67	0.22	0.68
12 – 14	0.667	11.	0.65	11.	1.3	0.52	2.6	0.052	0.75	0.15	0.57
14 – 16	0.743	11.	0.64	11.	1.5	0.45	2.6	0.061	0.86	0.17	0.97
16 – 19	0.840	12.	0.61	11.	1.6	0.40	2.6	0.056	1.0	0.14	0.91
19 – 22	0.950	13.	0.60	12.	1.5	0.46	2.6	0.071	1.2	0.27	1.2
22 – 25	1.09	13.	0.55	12.	1.4	0.46	2.6	0.063	1.3	0.17	1.0
25 – 28	1.26	12.	0.49	11.	1.1	0.43	2.6	0.044	1.2	0.22	0.58
28 – 31	1.47	9.9	0.43	9.4	0.78	0.40	2.6	0.036	1.2	0.15	0.43
31 – 34	1.68	8.0	0.39	7.4	0.48	0.35	2.6	0.036	1.2	0.082	0.44
34 – 37	1.85	6.6	0.36	5.9	0.37	0.28	2.6	0.030	1.1	0.15	0.42
37 – 40	1.93	5.5	0.35	4.7	0.20	0.22	2.6	0.035	0.94	0.050	0.60
40 – 43	1.94	4.7	0.34	3.7	0.13	0.21	2.6	0.029	0.89	0.046	0.47
43 – 46	1.90	4.2	0.35	3.2	0.086	0.19	2.5	0.023	0.85	0.024	0.34
46 – 49	1.81	3.8	0.39	2.6	0.012	0.18	2.5	0.026	0.87	0.030	0.39
49 – 53	1.69	3.5	0.38	2.0	0.032	0.12	2.6	0.031	0.74	0.037	0.61
53 – 57	1.54	3.1	0.43	1.6	0.039	0.14	2.5	0.013	0.71	0.097	0.13
57 – 61	1.38	3.0	0.46	1.4	0.0059	0.12	2.5	0.025	0.61	0.032	0.44
61 – 65	1.24	2.9	0.50	0.99	0.023	0.095	2.5	0.018	0.62	0.15	0.36
65 – 69	1.09	2.9	0.54	0.85	0.011	0.084	2.5	0.026	0.49	0.048	0.47
69 – 73	0.952	2.8	0.60	0.71	0.0078	0.11	2.5	0.017	0.47	0.093	0.27
73 – 78	0.820	2.8	0.56	0.60	0.017	0.068	2.5	0.020	0.47	0.13	0.37
78 – 83	0.695	2.9	0.63	0.46	0.037	0.052	2.6	0.037	0.44	0.12	0.81
83 – 88	0.581	2.8	0.70	0.36	0.015	0.079	2.6	0.026	0.43	0.13	0.53
88 – 93	0.489	2.7	0.79	0.34	0.010	0.080	2.5	0.0073	0.31	0.16	0.082
93 – 99	0.418	2.9	0.73	0.25	0.0017	0.055	2.6	0.035	0.40	0.23	0.75
99 – 105	0.344	2.8	0.83	0.24	0.013	0.084	2.5	0.012	0.41	0.00024	0.22
105 – 111	0.286	2.9	0.93	0.24	0.022	0.052	2.5	0.025	0.18	0.27	0.52
111 – 118	0.235	3.0	0.93	0.16	0.037	0.049	2.6	0.040	0.46	0.15	0.87
118 – 125	0.202	2.8	1.0	0.15	0.0043	0.094	2.5	0.0060	0.30	0.14	0.22
125 – 133	0.163	3.0	1.0	0.13	0.019	0.048	2.6	0.037	0.18	0.31	0.82
133 – 141	0.134	3.0	1.2	0.12	0.018	0.027	2.5	0.026	0.15	0.16	0.56
141 – 150	0.109	3.1	1.2	0.10	0.0058	0.042	2.6	0.033	0.35	0.48	0.73
150 – 160	0.0836	3.2	1.3	0.024	0.035	0.041	2.6	0.037	0.37	0.032	0.78
160 – 171	0.0682	3.0	1.3	0.11	0.013	0.066	2.5	0.00073	0.025	0.34	0.055
171 – 183	0.0522	3.2	1.5	0.067	0.0011	0.081	2.5	0.0050	0.33	0.28	0.011
183 – 197	0.0390	3.3	1.6	0.081	0.030	0.049	2.6	0.034	0.078	0.23	0.75
197 – 212	0.0301	3.3	1.7	0.049	0.017	0.077	2.5	0.0033	0.19	0.18	0.020
212 – 228	0.0217	3.9	2.0	0.013	0.033	0.022	2.6	0.055	0.47	0.25	1.2
228 – 246	0.0163	4.2	2.1	0.042	0.066	0.027	2.6	0.074	0.067	0.43	1.8
246 – 266	0.0112	4.1	2.5	0.015	0.039	0.055	2.6	0.035	0.32	0.19	0.78
266 – 289	0.00792	4.4	2.7	0.014	0.021	0.055	2.6	0.038	0.017	0.32	0.83
289 – 314	0.00561	4.6	3.1	0.036	0.0052	0.081	2.5	0.017	0.38	0.47	0.48
314 – 344	0.00347	5.3	3.5	0.059	0.039	0.034	2.6	0.050	0.31	0.31	1.1
344 – 377	0.00232	5.9	4.1	0.076	0.055	0.066	2.6	0.038	0.49	0.67	0.91
377 – 418	0.00141	6.4	4.6	0.032	0.032	0.064	2.5	0.012	0.0043	0.53	0.26
418 – 460	0.000792	8.5	6.3	0.014	0.029	0.061	2.5	0.0067	0.98	0.029	0.092
460 – 511	0.000474	10.	7.2	0.18	0.16	0.072	2.8	0.16	0.65	1.4	3.9
511 – 567	0.000236	13.	9.7	0.045	0.066	0.11	2.4	0.063	0.22	0.25	1.7
567 – 1300	2.91e-05	7.5	5.2	0.049	0.019	0.16	2.5	0.019	0.57	1.0	0.29

Table A.17: Differential cross section in $|y_{\mathrm{Z}}|$ ($N_{\mathrm{jets}} \geq 1$) and break down of the systematic uncertainties for the muon decay channel.

$\lvert y_{\mathrm{Z}}\rvert$	$\frac{d\sigma}{d\lvert y_{\mathrm{Z}}\rvert}$ [pb]	Tot. Unc [%]	stat [%]	JES [%]	JER [%]	Eff [%]	Lumi [%]	XSec [%]	PU [%]	LES+LER [%]	Unf sys [%]
0 – 0.2	67.6	4.6	0.22	3.7	0.32	0.25	2.5	0.023	0.62	0.054	0.30
0.2 – 0.4	67.3	4.5	0.21	3.6	0.30	0.26	2.6	0.032	0.68	0.044	0.48
0.4 – 0.6	66.8	4.5	0.21	3.6	0.28	0.25	2.6	0.032	0.66	0.051	0.46
0.6 – 0.8	66.0	4.5	0.21	3.6	0.28	0.23	2.6	0.027	0.64	0.035	0.39
0.8 – 1	64.5	4.5	0.22	3.6	0.29	0.20	2.6	0.029	0.67	0.021	0.46
1 – 1.2	61.8	4.6	0.22	3.7	0.28	0.21	2.6	0.031	0.69	0.039	0.50
1.2 – 1.4	57.3	4.6	0.23	3.7	0.30	0.19	2.6	0.026	0.69	0.046	0.43
1.4 – 1.6	50.3	4.6	0.25	3.7	0.28	0.15	2.6	0.031	0.71	0.050	0.55
1.6 – 1.8	41.4	4.7	0.28	3.7	0.28	0.14	2.6	0.037	0.77	0.042	0.71
1.8 – 2	30.4	4.6	0.32	3.6	0.27	0.12	2.6	0.039	0.80	0.047	0.75
2 – 2.2	18.3	4.5	0.42	3.5	0.27	0.16	2.6	0.039	0.90	0.055	0.75
2.2 – 2.4	5.78	4.6	0.78	3.5	0.32	0.25	2.5	0.025	1.1	0.040	0.30

Table A.18: Differential cross section in $y_{\mathrm{diff(jet1,jet2)}}$ ($N_{\mathrm{jets}} \geq 2$) and break down of the systematic uncertainties for the muon decay channel.

$y_{\mathrm{diff(jet1,jet2)}}$	$\frac{d\sigma}{dy_{\mathrm{diff(jet1,jet2)}}}$ [pb]	Tot. Unc [%]	stat [%]	JES [%]	JER [%]	Eff [%]	Lumi [%]	XSec [%]	PU [%]	LES+LER [%]	Unf sys [%]
0 – 0.2	24.8	5.8	0.46	5.0	0.25	0.28	2.6	0.046	0.91	0.074	0.79
0.2 – 0.4	25.0	5.9	0.46	5.1	0.26	0.30	2.6	0.037	0.89	0.044	0.55
0.4 – 0.6	20.8	5.9	0.51	5.1	0.23	0.28	2.6	0.048	0.94	0.048	0.78
0.6 – 0.8	17.5	5.6	0.56	4.8	0.22	0.28	2.6	0.034	0.76	0.053	0.52
0.8 – 1	14.4	6.0	0.63	5.1	0.26	0.22	2.6	0.061	0.97	0.078	1.3
1 – 1.2	11.0	6.1	0.74	5.3	0.45	0.24	2.5	0.021	0.96	0.090	0.17
1.2 – 1.4	7.87	6.7	0.90	5.8	0.48	0.17	2.6	0.040	1.4	0.088	0.75
1.4 – 1.6	5.20	7.4	1.2	6.4	0.72	0.39	2.6	0.057	1.5	0.081	0.84
1.6 – 1.8	3.19	8.0	1.6	7.0	0.79	0.22	2.5	0.010	2.1	0.085	0.16
1.8 – 2	1.76	9.5	2.3	7.7	0.99	0.18	2.7	0.12	2.7	0.22	2.6
2 – 2.2	0.709	12.	3.9	9.7	1.5	0.27	2.3	0.093	3.8	0.62	2.6
2.2 – 2.4	0.168	20.	9.4	16.	2.3	0.83	2.5	0.0088	3.5	1.0	0.90

Table A.19: Differential cross section in $y_{\mathrm{sum(jet1,jet2)}}$ ($N_{\mathrm{jets}} \geq 2$) and break down of the systematic uncertainties for the muon decay channel.

$y_{\mathrm{sum(jet1,jet2)}}$	$\frac{d\sigma}{dy_{\mathrm{sum(jet1,jet2)}}}$ [pb]	Tot. Unc [%]	stat [%]	JES [%]	JER [%]	Eff [%]	Lumi [%]	XSec [%]	PU [%]	LES+LER [%]	Unf sys [%]
0 – 0.2	21.1	5.5	0.45	4.7	0.16	0.25	2.6	0.050	0.65	0.026	0.82
0.2 – 0.4	20.0	5.6	0.36	4.9	0.23	0.26	2.6	0.033	0.72	0.0094	0.40
0.4 – 0.6	18.7	5.8	0.38	4.9	0.24	0.25	2.6	0.055	0.75	0.055	1.4
0.6 – 0.8	16.9	5.8	0.40	5.0	0.26	0.24	2.6	0.045	0.83	0.043	0.86
0.8 – 1	14.8	6.0	0.45	5.3	0.29	0.32	2.5	0.022	1.1	0.029	0.13
1 – 1.2	12.6	6.3	0.50	5.4	0.35	0.27	2.6	0.042	1.2	0.090	0.99
1.2 – 1.4	10.0	6.6	0.59	5.8	0.44	0.27	2.6	0.062	1.3	0.13	1.1
1.4 – 1.6	7.49	7.0	0.73	6.2	0.63	0.35	2.6	0.029	1.4	0.11	0.16
1.6 – 1.8	5.20	7.6	0.94	6.7	0.68	0.35	2.6	0.037	2.1	0.049	0.26
1.8 – 2	3.28	8.0	1.3	6.8	0.91	0.34	2.6	0.045	2.6	0.042	0.86
2 – 2.2	1.67	9.0	2.1	7.4	1.2	0.44	2.4	0.038	3.1	0.077	1.5
2.2 – 2.4	0.427	14.	5.3	10.	1.4	0.090	2.9	0.18	3.9	0.60	4.2

Table A.20: Differential cross section in $y_{\mathrm{diff(Z,jet1)}}$ ($N_{\mathrm{jets}} \geq 1$) and break down of the systematic uncertainties for the muon decay channel.

$y_{\mathrm{diff(Z,jet1)}}$	$\frac{d\sigma}{dy_{\mathrm{diff(Z,jet1)}}}$ [pb]	Tot. Unc [%]	stat [%]	JES [%]	JER [%]	Eff [%]	Lumi [%]	XSec [%]	PU [%]	LES+LER [%]	Unf sys [%]
0 – 0.2	142.	4.1	0.16	3.1	0.17	0.19	2.6	0.032	0.59	0.037	0.53
0.2 – 0.4	128.	4.2	0.17	3.2	0.18	0.18	2.6	0.031	0.62	0.043	0.56
0.4 – 0.6	104.	4.4	0.20	3.5	0.24	0.21	2.6	0.029	0.63	0.048	0.46
0.6 – 0.8	78.9	4.6	0.23	3.8	0.28	0.21	2.6	0.027	0.72	0.028	0.42
0.8 – 1	56.2	5.0	0.28	4.2	0.35	0.25	2.5	0.025	0.73	0.037	0.30
1 – 1.2	38.2	5.4	0.35	4.6	0.47	0.23	2.6	0.033	0.84	0.029	0.53
1.2 – 1.4	24.4	5.8	0.46	5.0	0.60	0.23	2.6	0.031	0.90	0.051	0.43
1.4 – 1.6	14.5	6.3	0.61	5.6	0.84	0.25	2.5	0.015	1.1	0.096	0.098
1.6 – 1.8	7.72	7.2	0.88	6.1	1.1	0.15	2.7	0.083	1.5	0.062	1.8
1.8 – 2	3.44	7.6	1.4	6.4	1.4	0.22	2.6	0.040	2.1	0.15	0.53
2 – 2.2	1.08	9.3	2.6	7.7	2.1	0.23	2.5	0.013	2.3	0.38	0.16
2.2 – 2.4	0.107	17.	8.9	9.3	2.6	1.1	2.0	0.24	1.7	1.3	8.6

Table A.21: Differential cross section in $y_{\mathrm{sum(Z,jet1)}}$ ($N_{\mathrm{jets}} \geq 1$) and break down of the systematic uncertainties for the muon decay channel.

$y_{\mathrm{sum(Z,jet1)}}$	$\frac{d\sigma}{dy_{\mathrm{sum(Z,jet1)}}}$ [pb]	Tot. Unc [%]	stat [%]	JES [%]	JER [%]	Eff [%]	Lumi [%]	XSec [%]	PU [%]	LES+LER [%]	Unf sys [%]
0 − 0.2	89.3	4.4	0.21	3.5	0.17	0.22	2.6	0.032	0.43	0.049	0.51
0.2 − 0.4	87.0	4.4	0.21	3.6	0.19	0.23	2.5	0.026	0.53	0.030	0.35
0.4 − 0.6	82.6	4.5	0.22	3.5	0.21	0.23	2.6	0.032	0.54	0.043	0.52
0.6 − 0.8	76.0	4.5	0.23	3.6	0.25	0.21	2.6	0.027	0.59	0.058	0.42
0.8 − 1	68.4	4.5	0.24	3.6	0.30	0.21	2.6	0.026	0.65	0.047	0.38
1 − 1.2	59.6	4.6	0.26	3.7	0.32	0.19	2.5	0.025	0.75	0.029	0.37
1.2 − 1.4	49.2	4.7	0.29	3.8	0.37	0.17	2.6	0.028	0.85	0.017	0.51
1.4 − 1.6	37.5	4.9	0.34	3.9	0.51	0.17	2.6	0.041	1.1	0.042	0.76
1.6 − 1.8	26.0	5.0	0.41	3.9	0.56	0.13	2.6	0.046	1.3	0.062	0.90
1.8 − 2	14.9	5.2	0.56	4.1	0.70	0.15	2.6	0.036	1.6	0.053	0.69
2 − 2.2	5.75	5.9	0.94	4.5	0.74	0.13	2.6	0.059	2.0	0.088	1.1
2.2 − 2.4	0.790	7.2	2.8	4.8	0.78	0.41	2.4	0.059	2.5	0.17	1.8

Table A.22: Differential cross section in $y_{\mathrm{diff(Z,jet1)}}$ ($N_{\mathrm{jets}} \geq 2$) and break down of the systematic uncertainties for the muon decay channel.

$y_{\mathrm{diff(Z,jet1)}}$	$\frac{d\sigma}{dy_{\mathrm{diff(Z,jet1)}}}$ [pb]	Tot. Unc [%]	stat [%]	JES [%]	JER [%]	Eff [%]	Lumi [%]	XSec [%]	PU [%]	LES+LER [%]	Unf sys [%]
0 − 0.2	29.6	6.0	0.44	5.2	0.37	0.33	2.6	0.049	1.0	0.043	0.79
0.2 − 0.4	26.8	6.0	0.46	5.2	0.31	0.25	2.6	0.046	0.94	0.087	0.81
0.4 − 0.6	22.2	5.9	0.50	5.2	0.31	0.34	2.5	0.026	1.0	0.071	0.33
0.6 − 0.8	17.4	6.0	0.58	5.2	0.32	0.12	2.6	0.054	1.0	0.037	1.1
0.8 − 1	12.9	6.2	0.70	5.4	0.17	0.30	2.6	0.042	0.83	0.073	0.57
1 − 1.2	9.28	6.2	0.84	5.4	0.36	0.26	2.6	0.032	1.1	0.036	0.52
1.2 − 1.4	6.32	6.1	1.0	5.2	0.32	0.25	2.6	0.043	0.93	0.027	0.70
1.4 − 1.6	4.05	6.0	1.3	5.0	0.34	0.24	2.5	0.011	1.3	0.058	0.054
1.6 − 1.8	2.23	7.5	1.9	6.2	0.28	0.16	2.6	0.073	1.8	0.16	1.1
1.8 − 2	1.13	7.2	2.6	5.0	0.41	0.33	2.7	0.081	2.2	0.093	1.7
2 − 2.2	0.350	9.9	5.0	6.5	1.2	0.28	2.3	0.084	2.5	0.27	1.7
2.2 − 2.4	0.0380	24.	18.	8.3	0.35	0.081	2.5	0.0067	0.019	0.61	0.43

Table A.23: Differential cross section in $y_{\mathrm{sum(Z,jet1)}}$ ($N_{\mathrm{jets}} \geq 2$) and break down of the systematic uncertainties for the muon decay channel.

$y_{\mathrm{sum(Z,jet1)}}$	$\frac{d\sigma}{dy_{\mathrm{sum(Z,jet1)}}}$ [pb]	Tot. Unc [%]	stat [%]	JES [%]	JER [%]	Eff [%]	Lumi [%]	XSec [%]	PU [%]	LES+LER [%]	Unf sys [%]
0 – 0.2	20.8	5.9	0.52	5.0	0.18	0.30	2.6	0.054	0.83	0.019	0.96
0.2 – 0.4	20.1	5.9	0.50	5.1	0.25	0.29	2.6	0.038	0.93	0.010	0.65
0.4 – 0.6	18.7	5.9	0.52	5.1	0.29	0.31	2.6	0.046	0.86	0.037	0.69
0.6 – 0.8	17.1	5.9	0.55	5.1	0.32	0.29	2.6	0.027	0.91	0.10	0.32
0.8 – 1	15.0	6.2	0.60	5.4	0.31	0.23	2.6	0.042	0.99	0.097	0.64
1 – 1.2	12.9	6.2	0.65	5.4	0.36	0.27	2.6	0.031	1.0	0.057	0.41
1.2 – 1.4	10.4	6.2	0.73	5.5	0.47	0.25	2.5	0.023	1.2	0.045	0.34
1.4 – 1.6	7.82	6.7	0.88	5.7	0.45	0.19	2.6	0.073	1.3	0.11	1.6
1.6 – 1.8	5.21	6.6	1.1	5.7	0.54	0.19	2.6	0.037	1.5	0.16	0.58
1.8 – 2	3.03	6.9	1.5	5.2	0.55	0.12	2.7	0.10	2.0	0.26	2.4
2 – 2.2	1.12	7.5	2.5	5.8	0.42	0.31	2.6	0.057	2.0	0.36	0.88
2.2 – 2.4	0.158	13.	7.3	7.4	1.4	0.98	2.2	0.15	1.7	0.12	3.0

Table A.24: Differential cross section in $y_{\mathrm{diff(Z,jet2)}}$ ($N_{\mathrm{jets}} \geq 2$) and break down of the systematic uncertainties for the muon decay channel.

$y_{\mathrm{diff(Z,jet2)}}$	$\frac{d\sigma}{dy_{\mathrm{diff(Z,jet2)}}}$ [pb]	Tot. Unc [%]	stat [%]	JES [%]	JER [%]	Eff [%]	Lumi [%]	XSec [%]	PU [%]	LES+LER [%]	Unf sys [%]
0 – 0.2	25.7	5.7	0.51	4.9	0.14	0.30	2.6	0.026	0.84	0.076	0.48
0.2 – 0.4	24.2	5.7	0.51	4.8	0.18	0.24	2.6	0.064	0.82	0.016	1.0
0.4 – 0.6	21.4	5.9	0.54	5.1	0.32	0.26	2.6	0.045	0.93	0.036	0.73
0.6 – 0.8	17.9	6.1	0.60	5.3	0.33	0.27	2.6	0.036	1.0	0.069	0.52
0.8 – 1	14.2	6.1	0.69	5.2	0.37	0.32	2.6	0.041	1.0	0.029	0.63
1 – 1.2	10.7	6.4	0.82	5.6	0.44	0.34	2.5	0.025	1.1	0.13	0.39
1.2 – 1.4	7.60	6.9	1.0	6.0	0.47	0.17	2.6	0.046	1.3	0.10	0.84
1.4 – 1.6	5.10	6.9	1.3	5.9	0.72	0.31	2.6	0.053	1.4	0.015	1.1
1.6 – 1.8	3.22	7.6	1.6	6.6	0.76	0.15	2.5	0.014	1.7	0.11	0.14
1.8 – 2	1.60	8.1	2.4	6.2	1.1	0.055	2.7	0.083	2.4	0.26	2.1
2 – 2.2	0.525	11.	4.5	8.0	1.1	0.23	2.7	0.090	2.2	0.18	2.0
2.2 – 2.4	0.0636	27.	14.	8.2	1.1	0.53	3.8	0.70	5.9	1.7	17.

Table A.25: Differential cross section in $y_{\mathrm{sum(Z,jet2)}}$ ($N_{\mathrm{jets}} \geq 2$) and break down of the systematic uncertainties for the muon decay channel.

$y_{\mathrm{sum(Z,jet2)}}$	$\frac{d\sigma}{dy_{\mathrm{sum(Z,jet2)}}}$ [pb]	Tot. Unc [%]	stat [%]	JES [%]	JER [%]	Eff [%]	Lumi [%]	XSec [%]	PU [%]	LES+LER [%]	Unf sys [%]
0 − 0.2	21.7	5.9	0.55	5.2	0.23	0.26	2.6	0.050	0.73	0.047	0.88
0.2 − 0.4	20.9	5.8	0.52	5.0	0.33	0.33	2.6	0.053	0.80	0.10	0.88
0.4 − 0.6	19.3	6.0	0.54	5.3	0.27	0.25	2.6	0.031	0.94	0.052	0.49
0.6 − 0.8	17.1	6.0	0.58	5.2	0.30	0.28	2.6	0.040	0.83	0.020	0.67
0.8 − 1	14.9	6.1	0.64	5.3	0.29	0.34	2.6	0.042	1.1	0.056	0.69
1 − 1.2	12.4	6.2	0.72	5.4	0.35	0.30	2.6	0.028	1.0	0.062	0.28
1.2 − 1.4	9.96	6.1	0.83	5.2	0.40	0.20	2.6	0.042	1.3	0.050	0.69
1.4 − 1.6	7.32	6.5	1.0	5.5	0.42	0.24	2.6	0.054	1.7	0.040	1.0
1.6 − 1.8	4.88	6.8	1.3	5.7	0.46	0.029	2.6	0.041	1.8	0.090	0.90
1.8 − 2	2.64	6.8	1.8	5.4	0.59	0.11	2.6	0.041	1.7	0.052	1.1
2 − 2.2	0.971	8.9	3.2	7.0	1.0	0.22	2.4	0.042	2.0	0.070	1.5
2.2 − 2.4	0.118	16.	11.	6.4	0.49	0.74	2.5	0.0061	3.8	1.2	3.1

Table A.26: Differential cross section in $y_{\mathrm{diff(Z,jet1+jet2)}}$ ($N_{\mathrm{jets}} \geq 2$) and break down of the systematic uncertainties for the muon decay channel.

$y_{\mathrm{diff(Z,jet1+jet2)}}$	$\frac{d\sigma}{dy_{\mathrm{diff(Z,jet1+jet2)}}}$ [pb]	Tot. Unc [%]	stat [%]	JES [%]	JER [%]	Eff [%]	Lumi [%]	XSec [%]	PU [%]	LES+LER [%]	Unf sys [%]
0 − 0.4	29.6	6.1	0.29	5.3	0.30	0.33	2.6	0.037	0.98	0.054	0.53
0.4 − 0.8	21.9	5.9	0.35	5.1	0.33	0.22	2.6	0.048	1.0	0.041	0.87
0.8 − 1.2	10.9	6.0	0.50	5.2	0.30	0.21	2.6	0.046	0.96	0.051	0.88
1.2 − 1.6	3.21	6.5	0.97	5.7	0.50	0.29	2.5	0.021	1.4	0.10	0.17
1.6 − 2	0.504	8.6	2.7	6.5	0.69	0.31	2.7	0.11	2.4	0.35	2.4
2 − 2.4	0.0221	27.	18.	12.	3.3	2.5	2.4	0.038	3.4	2.0	3.5

Table A.27: Differential cross section in $y_{\mathrm{sum(Z,jet1+jet2)}}$ ($N_{\mathrm{jets}} \geq 2$) and break down of the systematic uncertainties for the muon decay channel.

$y_{\mathrm{sum(Z,jet1+jet2)}}$	$\frac{d\sigma}{dy_{\mathrm{sum(Z,jet1+jet2)}}}$ [pb]	Tot. Unc [%]	stat [%]	JES [%]	JER [%]	Eff [%]	Lumi [%]	XSec [%]	PU [%]	LES+LER [%]	Unf sys [%]
0 – 0.4	22.6	6.0	0.33	5.2	0.29	0.30	2.6	0.043	0.93	0.038	0.73
0.4 – 0.8	19.7	6.0	0.37	5.2	0.33	0.29	2.6	0.043	0.92	0.020	0.64
0.8 – 1.2	14.2	6.0	0.43	5.2	0.29	0.25	2.6	0.035	0.94	0.049	0.55
1.2 – 1.6	7.45	6.1	0.61	5.2	0.35	0.18	2.6	0.051	1.4	0.086	0.98
1.6 – 2	2.10	6.8	1.2	5.7	0.70	0.22	2.6	0.048	1.8	0.17	1.1
2 – 2.4	0.130	12.	5.4	8.7	1.3	0.46	2.3	0.097	3.4	0.37	2.7

Table A.28: Differential cross section in $\Delta\phi_{\mathrm{Z,jet1}}$ ($N_{\mathrm{jets}} \geq 1$) and break down of the systematic uncertainties for the muon decay channel.

$\Delta\phi_{\mathrm{Z,jet1}}$	$\frac{d\sigma}{d\Delta\phi_{\mathrm{Z,jet1}}}$ [pb]	Tot. Unc [%]	stat [%]	JES [%]	JER [%]	Eff [%]	Lumi [%]	XSec [%]	PU [%]	LES+LER [%]	Unf sys [%]
0 – 0.1256	3.90	9.2	2.5	7.6	1.6	0.36	2.7	0.12	0.35	0.16	2.8
0.1256 – 0.2512	3.97	8.6	3.2	6.9	1.4	0.18	2.5	0.012	0.32	0.76	0.54
0.2512 – 0.3768	3.96	9.3	3.2	7.8	1.7	0.34	2.6	0.051	0.13	0.45	0.60
0.3768 – 0.5024	4.18	7.4	3.1	5.6	0.69	0.65	2.6	0.076	0.25	0.32	0.50
0.5024 – 0.628	4.48	9.0	3.0	7.6	1.1	0.065	2.5	0.0063	0.093	0.22	0.88
0.628 – 0.7536	4.55	8.7	2.9	7.2	1.1	0.28	2.7	0.081	0.026	0.26	1.8
0.7536 – 0.8792	4.71	8.9	2.7	7.7	0.69	0.59	2.6	0.075	0.24	0.60	0.82
0.8792 – 1.0048	5.34	7.5	2.5	5.9	1.1	0.047	2.7	0.082	0.30	0.44	1.8
1.0048 – 1.1304	5.66	7.5	2.4	6.3	1.0	0.45	2.5	0.023	0.11	0.23	0.021
1.1304 – 1.256	6.11	7.4	2.3	5.8	0.77	0.077	2.7	0.089	0.073	0.12	2.1
1.256 – 1.3816	7.19	7.0	2.0	5.8	0.81	0.32	2.6	0.065	0.40	0.35	1.2
1.3816 – 1.5072	7.76	6.5	1.9	5.4	0.78	0.44	2.5	0.0098	0.096	0.55	0.49
1.5072 – 1.6328	9.38	6.2	1.6	5.1	0.91	0.14	2.6	0.051	0.61	0.23	0.83
1.6328 – 1.7584	10.9	6.4	1.4	5.4	0.67	0.19	2.6	0.035	0.48	0.19	0.74
1.7584 – 1.884	13.5	5.8	1.2	4.9	0.59	0.28	2.5	0.026	0.44	0.11	0.30
1.884 – 2.0096	16.2	5.7	1.1	4.9	0.48	0.36	2.5	0.010	0.33	0.095	0.085
2.0096 – 2.1352	20.6	5.8	0.93	4.8	0.54	0.20	2.6	0.067	0.61	0.084	1.3
2.1352 – 2.2608	25.9	5.4	0.79	4.5	0.41	0.29	2.6	0.033	0.79	0.050	0.37
2.2608 – 2.3864	34.2	5.5	0.66	4.5	0.36	0.21	2.6	0.052	0.81	0.087	1.0
2.3864 – 2.512	43.9	5.4	0.56	4.6	0.34	0.24	2.6	0.027	0.76	0.073	0.41
2.512 – 2.6376	59.7	5.0	0.46	4.1	0.28	0.20	2.6	0.042	0.76	0.051	0.77
2.6376 – 2.7632	82.8	4.8	0.38	3.9	0.29	0.23	2.6	0.031	0.80	0.051	0.50
2.7632 – 2.8888	118.	4.5	0.30	3.6	0.24	0.20	2.5	0.024	0.78	0.053	0.37
2.8888 – 3.0144	178.	4.2	0.23	3.2	0.17	0.19	2.6	0.029	0.75	0.033	0.46
3.0144 – 3.14	276.	3.7	0.15	2.5	0.14	0.16	2.5	0.022	0.72	0.039	0.33

Table A.29: Differential cross section in $\Delta\phi_{\mathrm{Z,jet1}}$ ($N_{\mathrm{jets}} \geq 2$) and break down of the systematic uncertainties for the muon decay channel.

$\Delta\phi_{\mathrm{Z,jet1}}$	$\frac{d\sigma}{d\Delta\phi_{\mathrm{Z,jet1}}}$ [pb]	Tot. Unc [%]	stat [%]	JES [%]	JER [%]	Eff [%]	Lumi [%]	XSec [%]	PU [%]	LES+LER [%]	Unf sys [%]
0 – 0.1256	1.61	8.3	4.1	4.9	0.63	0.16	2.7	0.12	1.3	0.44	3.0
0.1256 – 0.2512	1.63	8.5	5.0	4.4	1.4	0.45	2.5	0.022	0.055	0.74	1.9
0.2512 – 0.3768	1.82	8.1	4.6	4.8	0.25	0.67	2.5	0.022	0.28	0.38	1.2
0.3768 – 0.5024	1.69	8.1	4.7	3.2	0.83	0.36	2.8	0.15	0.073	0.62	3.6
0.5024 – 0.628	1.90	7.6	4.3	4.2	0.69	0.62	2.6	0.029	1.3	0.38	1.4
0.628 – 0.7536	1.87	9.1	4.3	3.7	0.79	0.33	2.9	0.21	0.48	0.14	5.5
0.7536 – 0.8792	1.83	8.1	4.3	4.8	0.51	0.70	2.4	0.055	0.31	0.93	2.2
0.8792 – 1.0048	2.26	7.0	3.7	4.2	0.23	0.35	2.6	0.042	1.0	0.50	1.2
1.0048 – 1.1304	2.39	7.2	3.5	4.6	0.29	0.40	2.6	0.050	0.27	0.28	1.8
1.1304 – 1.256	2.58	7.0	3.4	4.2	0.90	0.23	2.6	0.072	0.88	0.28	1.8
1.256 – 1.3816	3.16	6.4	2.9	4.4	0.47	0.38	2.6	0.048	0.35	0.79	1.1
1.3816 – 1.5072	3.17	6.5	2.9	4.5	0.45	0.13	2.6	0.050	0.55	0.54	1.1
1.5072 – 1.6328	3.99	5.8	2.4	3.8	0.33	0.37	2.5	0.014	1.1	0.47	1.2
1.6328 – 1.7584	4.73	6.2	2.1	4.6	0.34	0.083	2.6	0.063	0.97	0.23	1.5
1.7584 – 1.884	5.95	5.6	1.8	4.4	0.13	0.26	2.5	0.0044	0.65	0.23	0.23
1.884 – 2.0096	7.05	5.5	1.6	4.3	0.22	0.22	2.5	0.024	0.96	0.12	0.77
2.0096 – 2.1352	8.89	5.6	1.3	4.3	0.30	0.20	2.6	0.072	0.87	0.15	1.5
2.1352 – 2.2608	11.1	5.3	1.1	4.1	0.080	0.14	2.6	0.056	1.1	0.069	1.1
2.2608 – 2.3864	13.6	5.4	1.0	4.4	0.19	0.21	2.6	0.034	1.1	0.093	0.52
2.3864 – 2.512	15.6	5.6	0.90	4.6	0.066	0.27	2.6	0.048	1.2	0.10	0.85
2.512 – 2.6376	18.6	5.8	0.80	4.9	0.21	0.22	2.6	0.039	1.1	0.084	0.63
2.6376 – 2.7632	21.1	6.3	0.73	5.5	0.34	0.28	2.6	0.043	1.1	0.10	0.71
2.7632 – 2.8888	23.3	6.5	0.68	5.8	0.35	0.32	2.5	0.024	1.2	0.038	0.23
2.8888 – 3.0144	25.0	6.9	0.66	6.2	0.35	0.37	2.6	0.048	1.2	0.064	0.73
3.0144 – 3.14	25.9	7.8	0.63	7.1	0.47	0.41	2.6	0.050	1.1	0.078	0.60

Table A.30: Differential cross section in $\Delta\phi_{\mathrm{Z,jet1}}$ ($N_{\mathrm{jets}} \geq 3$) and break down of the systematic uncertainties for the muon decay channel.

$\Delta\phi_{\mathrm{Z,jet1}}$	$\frac{d\sigma}{d\Delta\phi_{\mathrm{Z,jet1}}}$ [pb]	Tot. Unc [%]	stat [%]	JES [%]	JER [%]	Eff [%]	Lumi [%]	XSec [%]	PU [%]	LES+LER [%]	Unf sys [%]
0 – 0.1256	0.503	14.	6.6	5.0	0.33	0.91	3.1	0.32	1.8	0.90	9.7
0.1256 – 0.2512	0.589	11.	7.0	6.1	0.84	0.84	2.4	0.054	0.99	1.1	0.063
0.2512 – 0.3768	0.619	11.	6.9	5.3	0.17	1.6	2.4	0.032	0.091	0.88	4.3
0.3768 – 0.5024	0.597	10.	6.8	4.4	0.59	0.27	2.7	0.11	0.72	0.27	1.7
0.5024 – 0.628	0.562	12.	6.9	7.5	0.36	0.45	2.5	2.5e-05	0.32	1.1	0.68
0.628 – 0.7536	0.588	11.	6.6	4.5	0.68	0.29	2.8	0.17	2.2	0.76	4.3
0.7536 – 0.8792	0.672	9.6	5.9	5.3	0.12	0.17	2.6	0.049	0.70	0.21	0.48
0.8792 – 1.0048	0.747	9.7	5.7	5.5	0.39	0.60	2.6	0.034	1.4	0.48	1.5
1.0048 – 1.1304	0.764	11.	5.4	5.3	0.64	0.55	2.9	0.18	1.9	0.42	5.7
1.1304 – 1.256	0.856	9.5	5.2	5.9	0.40	0.75	2.6	0.059	1.6	0.70	0.12
1.256 – 1.3816	0.994	8.5	4.6	5.5	0.43	0.035	2.6	0.044	0.45	0.32	0.77
1.3816 – 1.5072	0.914	9.8	4.8	6.8	0.70	0.50	2.3	0.093	1.2	0.053	2.1
1.5072 – 1.6328	1.09	9.9	4.1	7.4	0.46	0.62	2.4	0.035	2.1	0.13	2.1
1.6328 – 1.7584	1.22	8.3	3.8	5.7	0.65	0.59	2.4	0.034	1.4	0.29	2.0
1.7584 – 1.884	1.47	8.2	3.4	5.6	0.072	0.65	2.7	0.13	1.3	0.36	2.6
1.884 – 2.0096	1.56	8.6	3.3	6.9	0.64	0.35	2.4	0.067	1.1	0.37	1.1
2.0096 – 2.1352	1.96	8.8	2.8	7.1	0.90	0.041	2.7	0.11	0.89	0.41	2.4
2.1352 – 2.2608	2.18	8.3	2.7	6.9	0.49	0.34	2.6	0.052	1.3	0.19	0.98
2.2608 – 2.3864	2.60	7.8	2.4	6.6	0.49	0.36	2.5	0.0040	1.5	0.20	0.097
2.3864 – 2.512	2.89	8.7	2.2	7.5	0.55	0.29	2.6	0.053	1.7	0.25	0.65
2.512 – 2.6376	3.48	8.6	1.9	7.5	0.74	0.34	2.6	0.055	1.8	0.076	0.72
2.6376 – 2.7632	3.93	8.4	1.8	7.3	0.43	0.47	2.6	0.053	1.9	0.25	0.89
2.7632 – 2.8888	4.56	8.2	1.7	7.3	0.41	0.46	2.5	0.024	1.7	0.0099	0.15
2.8888 – 3.0144	5.00	9.0	1.6	7.8	0.30	0.17	2.7	0.13	1.5	0.14	2.7
3.0144 – 3.14	5.35	9.2	1.5	8.3	0.53	0.41	2.6	0.071	2.1	0.19	1.2

Table A.31: Differential cross section in $\Delta\phi_{\mathrm{Z,jet2}}$ ($N_{\mathrm{jets}} \geq 2$) and break down of the systematic uncertainties for the muon decay channel.

$\Delta\phi_{\mathrm{Z,jet2}}$	$\frac{d\sigma}{d\Delta\phi_{\mathrm{Z,jet2}}}$ [pb]	Tot. Unc [%]	stat [%]	JES [%]	JER [%]	Eff [%]	Lumi [%]	XSec [%]	PU [%]	LES+LER [%]	Unf sys [%]
0 – 0.1256	6.16	5.2	1.5	4.0	0.020	0.044	2.6	0.036	0.81	0.099	0.82
0.1256 – 0.2512	6.32	5.6	1.6	4.3	0.24	0.69	2.5	0.028	0.79	0.095	0.75
0.2512 – 0.3768	6.19	5.5	1.6	4.1	0.019	0.16	2.6	0.032	0.82	0.022	1.6
0.3768 – 0.5024	6.35	5.6	1.6	4.5	0.19	0.38	2.5	0.027	1.0	0.20	0.10
0.5024 – 0.628	6.40	5.5	1.6	4.2	0.22	0.27	2.5	0.018	1.1	0.18	0.50
0.628 – 0.7536	6.59	5.6	1.6	4.5	0.0069	0.017	2.6	0.026	0.63	0.051	0.57
0.7536 – 0.8792	6.93	5.5	1.5	4.3	0.26	0.84	2.6	0.048	0.72	0.15	0.48
0.8792 – 1.0048	6.91	6.3	1.5	4.5	0.11	0.54	2.7	0.064	0.79	0.041	2.8
1.0048 – 1.1304	7.42	5.5	1.5	4.3	0.29	0.64	2.6	0.056	0.72	0.12	0.36
1.1304 – 1.256	7.75	5.6	1.4	4.5	0.33	0.47	2.6	0.054	1.2	0.070	0.24
1.256 – 1.3816	7.88	6.2	1.4	4.6	0.24	0.25	2.6	0.059	0.86	0.077	2.4
1.3816 – 1.5072	8.45	5.7	1.4	4.7	0.15	0.39	2.6	0.037	0.87	0.015	0.077
1.5072 – 1.6328	8.77	5.7	1.3	4.7	0.28	0.19	2.6	0.029	0.86	0.12	1.0
1.6328 – 1.7584	9.25	5.8	1.3	4.9	0.22	0.31	2.5	0.021	0.87	0.12	0.13
1.7584 – 1.884	9.51	6.0	1.3	5.0	0.18	0.15	2.6	0.040	1.1	0.10	0.63
1.884 – 2.0096	9.61	6.5	1.3	5.1	0.41	0.0091	2.6	0.070	1.0	0.12	2.1
2.0096 – 2.1352	9.92	5.9	1.3	4.9	0.14	0.77	2.6	0.059	1.1	0.19	0.20
2.1352 – 2.2608	9.88	6.4	1.3	5.5	0.20	0.31	2.5	0.029	1.0	0.24	0.075
2.2608 – 2.3864	9.76	6.8	1.4	5.8	0.32	0.16	2.6	0.020	1.3	0.14	0.58
2.3864 – 2.512	9.77	7.0	1.4	6.1	0.59	0.19	2.6	0.028	1.1	0.19	1.1
2.512 – 2.6376	10.1	7.3	1.4	6.4	0.66	0.58	2.6	0.050	1.3	0.13	0.45
2.6376 – 2.7632	10.2	7.4	1.4	6.5	0.40	0.38	2.6	0.061	1.2	0.17	1.1
2.7632 – 2.8888	10.4	7.7	1.4	6.9	0.45	0.47	2.6	0.060	0.82	0.28	0.74
2.8888 – 3.0144	10.3	7.7	1.4	6.7	0.77	0.80	2.6	0.053	1.4	0.30	0.26
3.0144 – 3.14	9.80	8.1	1.4	7.1	0.77	0.14	2.6	0.034	1.2	0.15	1.7

Table A.32: Differential cross section in $\Delta\phi_{\mathrm{Z,jet2}}$ ($N_{\mathrm{jets}} \geq 3$) and break down of the systematic uncertainties for the muon decay channel.

$\Delta\phi_{\mathrm{Z,jet2}}$	$\frac{d\sigma}{d\Delta\phi_{\mathrm{Z,jet2}}}$ [pb]	Tot. Unc [%]	stat [%]	JES [%]	JER [%]	Eff [%]	Lumi [%]	XSec [%]	PU [%]	LES+LER [%]	Unf sys [%]
0 – 0.1256	1.40	8.7	3.6	6.6	0.071	0.21	2.5	0.017	1.9	0.39	0.61
0.1256 – 0.2512	1.51	8.1	3.8	5.8	0.20	0.029	2.6	0.057	1.9	0.15	0.53
0.2512 – 0.3768	1.47	8.7	3.8	6.5	0.27	0.16	2.5	0.024	1.5	0.45	1.2
0.3768 – 0.5024	1.48	9.8	3.9	6.8	0.28	0.039	2.8	0.18	0.73	0.35	4.1
0.5024 – 0.628	1.40	8.7	4.1	6.3	0.40	0.64	2.5	0.0042	1.3	0.51	0.39
0.628 – 0.7536	1.41	9.0	4.0	7.0	0.35	0.19	2.5	0.018	0.13	0.32	0.91
0.7536 – 0.8792	1.57	9.1	3.8	6.6	0.29	0.52	2.7	0.11	0.84	0.33	2.7
0.8792 – 1.0048	1.41	8.7	4.0	6.2	0.53	0.096	2.5	0.0014	1.9	0.58	0.16
1.0048 – 1.1304	1.66	8.8	3.6	6.9	0.79	0.96	2.7	0.092	0.030	0.13	0.79
1.1304 – 1.256	1.57	9.2	3.8	7.1	0.48	0.026	2.5	0.017	1.5	0.33	0.72
1.256 – 1.3816	1.61	9.6	3.7	7.1	0.31	0.14	2.7	0.11	2.2	0.43	2.8
1.3816 – 1.5072	1.67	8.6	3.6	6.6	0.022	0.45	2.6	0.062	1.1	0.43	0.83
1.5072 – 1.6328	1.67	8.7	3.6	6.4	1.1	0.093	2.6	0.039	1.4	0.85	1.5
1.6328 – 1.7584	1.71	8.8	3.7	6.7	0.91	0.95	2.5	0.015	1.5	0.66	0.20
1.7584 – 1.884	1.93	9.6	3.4	8.0	0.86	0.26	2.6	0.041	1.1	0.65	0.44
1.884 – 2.0096	1.92	8.9	3.4	7.2	0.92	0.22	2.5	0.015	0.97	0.56	0.023
2.0096 – 2.1352	2.17	9.4	3.3	7.5	0.17	0.71	2.6	0.070	2.5	0.74	0.64
2.1352 – 2.2608	1.95	8.9	3.5	6.9	0.015	0.30	2.6	0.029	1.9	0.30	0.34
2.2608 – 2.3864	2.14	9.3	3.3	7.5	0.27	0.29	2.5	0.023	2.3	0.42	0.64
2.3864 – 2.512	2.29	9.0	3.4	6.7	0.36	0.38	2.7	0.12	1.4	0.73	2.6
2.512 – 2.6376	2.39	9.0	3.2	6.9	0.56	0.40	2.7	0.11	2.1	0.31	1.9
2.6376 – 2.7632	2.35	9.2	3.4	6.6	0.51	0.064	2.8	0.16	1.8	0.71	3.2
2.7632 – 2.8888	2.30	10.	3.5	8.4	1.1	0.19	2.5	0.0054	1.6	0.37	0.46
2.8888 – 3.0144	2.33	9.3	3.4	7.3	0.13	1.0	2.5	0.012	2.2	0.74	1.1
3.0144 – 3.14	2.38	9.6	3.4	7.9	0.67	0.51	2.6	0.039	1.4	0.11	1.2

Table A.33: Differential cross section in $\Delta\phi_{\mathrm{Z,jet3}}$ ($N_{\mathrm{jets}} \geq 3$) and break down of the systematic uncertainties for the muon decay channel.

$\Delta\phi_{\mathrm{Z,jet3}}$	$\frac{d\sigma}{d\Delta\phi_{\mathrm{Z,jet3}}}$ [pb]	Tot. Unc [%]	stat [%]	JES [%]	JER [%]	Eff [%]	Lumi [%]	XSec [%]	PU [%]	LES+LER [%]	Unf sys [%]
0 – 0.1256	1.29	8.3	4.1	5.6	0.16	0.81	2.6	0.063	1.3	0.17	0.25
0.1256 – 0.2512	1.37	9.7	4.5	7.1	0.50	0.19	2.7	0.11	0.43	0.50	2.3
0.2512 – 0.3768	1.32	9.5	4.6	5.9	0.81	0.0079	2.6	0.076	2.6	0.46	2.9
0.3768 – 0.5024	1.34	9.2	4.4	6.6	1.3	0.39	2.5	0.0071	1.3	0.56	0.12
0.5024 – 0.628	1.24	11.	4.7	8.5	0.19	0.060	2.6	0.066	1.8	0.59	1.2
0.628 – 0.7536	1.34	11.	4.3	6.3	1.1	0.54	3.0	0.24	2.0	0.29	6.6
0.7536 – 0.8792	1.29	9.5	4.6	6.7	0.36	0.31	2.5	0.012	1.8	0.54	0.76
0.8792 – 1.0048	1.46	9.3	4.3	6.5	0.70	0.036	2.6	0.081	1.4	0.58	2.0
1.0048 – 1.1304	1.36	9.7	4.3	6.7	0.46	0.17	2.7	0.091	0.58	0.71	3.2
1.1304 – 1.256	1.49	9.9	4.1	7.7	0.062	0.21	2.6	0.035	2.0	0.29	0.45
1.256 – 1.3816	1.51	9.3	4.1	6.4	1.1	0.27	2.3	0.083	1.6	0.35	2.7
1.3816 – 1.5072	1.49	11.	4.1	7.8	0.56	0.53	2.8	0.13	2.1	0.25	3.5
1.5072 – 1.6328	1.59	9.1	3.9	7.0	0.32	0.94	2.5	0.021	0.67	0.072	0.66
1.6328 – 1.7584	1.67	10.	3.8	7.6	0.65	0.46	2.4	0.043	3.2	0.26	2.0
1.7584 – 1.884	1.78	10.	3.8	8.4	0.50	0.93	2.7	0.092	1.9	0.16	0.95
1.884 – 2.0096	1.78	10.	3.7	7.9	0.15	0.30	2.7	0.12	1.4	0.63	2.6
2.0096 – 2.1352	1.96	8.7	3.4	6.7	0.56	0.10	2.7	0.092	1.0	0.16	1.9
2.1352 – 2.2608	2.13	8.9	3.3	7.3	1.2	0.47	2.4	0.035	1.0	0.23	0.95
2.2608 – 2.3864	2.26	8.4	3.1	6.6	0.63	0.61	2.5	0.013	2.1	0.28	0.33
2.3864 – 2.512	2.28	9.2	3.2	7.6	0.34	0.40	2.5	0.012	1.6	0.30	0.36
2.512 – 2.6376	2.60	8.1	2.8	6.5	0.31	0.39	2.6	0.064	1.3	0.49	0.63
2.6376 – 2.7632	2.68	8.7	2.9	6.9	0.56	0.35	2.6	0.053	1.8	0.33	1.9
2.7632 – 2.8888	2.69	8.2	2.8	6.6	0.0088	0.58	2.6	0.069	1.4	0.33	1.1
2.8888 – 3.0144	2.96	8.7	2.7	7.1	0.15	0.044	2.7	0.11	1.3	0.29	2.3
3.0144 – 3.14	2.84	8.2	2.7	7.0	0.32	0.29	2.5	0.025	0.85	0.36	0.24

Table A.34: Differential cross section in $\Delta\phi_{\mathrm{jet1,jet2}}$ ($N_{\mathrm{jets}} \geq 2$) and break down of the systematic uncertainties for the muon decay channel.

$\Delta\phi_{\mathrm{jet1,jet2}}$	$\frac{d\sigma}{d\Delta\phi_{\mathrm{jet1,jet2}}}$ [pb]	Tot. Unc [%]	stat [%]	JES [%]	JER [%]	Eff [%]	Lumi [%]	XSec [%]	PU [%]	LES+LER [%]	Unf sys [%]
0 – 0.1256	3.92	9.1	1.8	8.2	0.63	0.43	2.6	0.046	1.7	0.15	0.61
0.1256 – 0.2512	4.31	9.2	2.0	8.3	0.83	0.16	2.6	0.050	0.80	0.26	0.99
0.2512 – 0.3768	4.70	8.6	1.9	7.7	0.69	0.54	2.5	0.010	1.4	0.13	0.36
0.3768 – 0.5024	5.68	8.3	1.7	7.4	0.44	0.48	2.6	0.043	1.1	0.32	0.49
0.5024 – 0.628	5.73	8.7	1.7	7.7	0.23	0.45	2.7	0.088	1.3	0.18	1.8
0.628 – 0.7536	5.25	8.4	1.7	7.4	0.65	0.36	2.7	0.098	1.0	0.045	1.7
0.7536 – 0.8792	4.73	8.7	1.9	7.8	0.46	0.28	2.6	0.030	1.4	0.18	0.39
0.8792 – 1.0048	4.77	8.0	1.9	7.0	0.61	0.48	2.6	0.053	0.95	0.085	0.63
1.0048 – 1.1304	4.53	8.9	1.9	7.9	0.61	0.36	2.5	0.0061	1.9	0.090	0.34
1.1304 – 1.256	4.86	7.8	1.8	6.8	0.72	0.38	2.6	0.052	1.2	0.15	0.79
1.256 – 1.3816	4.75	8.3	1.8	7.3	0.49	0.42	2.6	0.044	1.7	0.11	0.77
1.3816 – 1.5072	5.29	8.0	1.7	7.2	0.48	0.20	2.5	0.017	0.99	0.057	0.061
1.5072 – 1.6328	5.66	7.5	1.6	6.6	0.29	0.37	2.6	0.038	0.96	0.083	0.28
1.6328 – 1.7584	6.03	7.3	1.6	6.3	0.42	0.20	2.6	0.039	1.3	0.11	0.67
1.7584 – 1.884	6.70	7.1	1.5	6.1	0.48	0.37	2.6	0.057	1.4	0.070	1.0
1.884 – 2.0096	7.50	6.8	1.4	5.8	0.31	0.32	2.6	0.061	0.95	0.066	1.1
2.0096 – 2.1352	8.36	6.4	1.3	5.5	0.38	0.26	2.5	0.012	1.2	0.11	0.0042
2.1352 – 2.2608	9.31	6.2	1.2	5.3	0.44	0.19	2.6	0.032	0.89	0.11	0.43
2.2608 – 2.3864	10.6	5.8	1.1	4.8	0.24	0.30	2.6	0.053	1.1	0.041	0.88
2.3864 – 2.512	11.9	5.6	0.99	4.4	0.22	0.20	2.6	0.072	1.1	0.14	1.5
2.512 – 2.6376	13.3	5.3	0.92	4.3	0.12	0.26	2.6	0.028	0.94	0.11	0.43
2.6376 – 2.7632	15.5	4.8	0.83	3.8	0.26	0.20	2.5	0.0055	0.79	0.043	0.062
2.7632 – 2.8888	17.4	4.7	0.77	3.5	0.24	0.22	2.6	0.052	0.92	0.048	1.0
2.8888 – 3.0144	19.0	4.7	0.74	3.7	0.075	0.20	2.6	0.032	0.75	0.052	0.64
3.0144 – 3.14	20.9	4.4	0.66	3.3	0.11	0.19	2.6	0.053	0.57	0.074	1.1

Table A.35: Differential cross section in $\Delta\phi_{\mathrm{jet1,jet2}}$ ($N_{\mathrm{jets}} \geq 3$) and break down of the systematic uncertainties for the muon decay channel.

$\Delta\phi_{\mathrm{jet1,jet2}}$	$\frac{d\sigma}{d\Delta\phi_{\mathrm{jet1,jet2}}}$ [pb]	Tot. Unc [%]	stat [%]	JES [%]	JER [%]	Eff [%]	Lumi [%]	XSec [%]	PU [%]	LES+LER [%]	Unf sys [%]
0 – 0.1256	0.749	12.	5.3	9.0	1.4	0.64	2.6	0.040	1.2	0.39	0.65
0.1256 – 0.2512	0.828	13.	5.8	10.	1.6	0.20	2.7	0.083	1.4	0.42	2.6
0.2512 – 0.3768	0.982	11.	5.2	7.9	0.34	0.42	2.6	0.044	3.4	0.75	0.43
0.3768 – 0.5024	1.13	11.	4.8	8.8	0.91	0.79	2.6	0.075	1.3	0.23	0.62
0.5024 – 0.628	1.16	12.	4.8	9.6	0.35	0.56	2.6	0.062	2.1	0.81	1.3
0.628 – 0.7536	1.05	13.	4.9	9.7	1.6	0.35	2.9	0.23	1.9	0.30	4.5
0.7536 – 0.8792	0.899	14.	5.4	11.	0.54	1.0	2.7	0.089	2.6	0.27	0.040
0.8792 – 1.0048	1.00	9.6	4.9	6.5	1.2	0.46	2.5	0.014	2.0	0.67	0.092
1.0048 – 1.1304	0.897	12.	5.2	8.4	0.33	0.080	2.7	0.096	1.5	0.63	2.9
1.1304 – 1.256	1.02	11.	5.0	8.1	1.4	0.40	2.5	0.0023	2.9	0.96	0.58
1.256 – 1.3816	1.01	11.	4.7	7.9	0.41	0.73	2.8	0.18	2.7	0.25	4.2
1.3816 – 1.5072	1.12	10.	4.5	7.6	0.016	0.15	2.5	0.025	1.6	0.15	0.67
1.5072 – 1.6328	1.19	9.9	4.4	7.5	0.38	0.79	2.5	0.0011	1.1	0.42	0.64
1.6328 – 1.7584	1.29	9.7	4.2	7.5	0.79	0.13	2.6	0.040	1.6	0.35	0.78
1.7584 – 1.884	1.48	9.0	3.7	6.9	0.38	0.57	2.5	0.015	1.7	0.26	0.90
1.884 – 2.0096	1.71	8.7	3.4	6.5	0.59	0.37	2.7	0.098	1.6	0.23	2.2
2.0096 – 2.1352	1.87	8.7	3.2	6.9	0.51	0.20	2.6	0.047	1.8	0.13	1.1
2.1352 – 2.2608	2.00	8.7	3.0	7.3	0.89	0.074	2.5	0.020	0.98	0.17	0.11
2.2608 – 2.3864	2.31	8.0	2.7	6.6	0.32	0.42	2.5	0.019	1.4	0.14	0.079
2.3864 – 2.512	2.71	7.9	2.4	6.2	0.36	0.021	2.7	0.080	1.9	0.050	1.8
2.512 – 2.6376	2.89	8.4	2.3	7.3	0.21	0.69	2.5	0.0015	0.82	0.23	0.66
2.6376 – 2.7632	3.52	6.8	2.0	5.5	0.45	0.39	2.6	0.040	1.5	0.11	0.20
2.7632 – 2.8888	3.90	7.4	1.9	6.1	0.46	0.36	2.6	0.061	1.5	0.20	1.4
2.8888 – 3.0144	4.38	7.1	1.8	6.1	0.020	0.42	2.6	0.046	1.4	0.16	0.37
3.0144 – 3.14	4.69	7.8	1.7	6.4	0.13	0.0070	2.7	0.096	0.79	0.13	2.6

Table A.36: Differential cross section in $\Delta\phi_{\text{jet1,jet3}}$ ($N_{\text{jets}} \geq 3$) and break down of the systematic uncertainties for the muon decay channel.

$\Delta\phi_{\text{jet1,jet3}}$	$\frac{d\sigma}{d\Delta\phi_{\text{jet1,jet3}}}$ [pb]	Tot. Unc [%]	stat [%]	JES [%]	JER [%]	Eff [%]	Lumi [%]	XSec [%]	PU [%]	LES+LER [%]	Unf sys [%]
0 – 0.1256	1.21	12.	4.8	9.8	0.55	0.48	2.5	0.017	2.3	0.45	0.80
0.1256 – 0.2512	1.01	13.	6.2	10.	0.32	0.73	2.6	0.078	1.1	0.77	1.8
0.2512 – 0.3768	1.42	12.	4.8	9.5	0.18	0.28	2.7	0.092	2.4	1.5	1.9
0.3768 – 0.5024	1.66	12.	4.4	9.8	1.2	1.3	2.7	0.11	1.3	0.65	1.6
0.5024 – 0.628	1.73	10.	4.3	8.2	1.1	0.040	2.7	0.083	0.83	0.13	1.4
0.628 – 0.7536	1.43	12.	4.8	8.8	0.83	0.29	2.9	0.20	3.1	0.68	4.1
0.7536 – 0.8792	1.35	12.	4.9	9.1	0.62	0.53	2.6	0.028	2.6	0.10	0.58
0.8792 – 1.0048	1.22	10.	5.2	7.3	0.23	0.98	2.7	0.095	0.16	0.24	1.1
1.0048 – 1.1304	1.34	12.	5.0	9.2	0.95	0.081	2.5	0.0016	0.25	0.86	0.82
1.1304 – 1.256	1.40	9.6	4.6	7.1	0.19	0.79	2.5	0.028	0.77	0.42	1.1
1.256 – 1.3816	1.34	12.	5.1	7.8	0.48	0.019	3.0	0.25	1.6	0.68	6.1
1.3816 – 1.5072	1.46	11.	4.7	7.3	1.1	1.2	2.4	0.068	2.3	0.17	3.5
1.5072 – 1.6328	1.48	8.6	4.7	5.6	0.15	0.44	2.5	0.025	0.70	0.40	0.73
1.6328 – 1.7584	1.58	10.	4.4	8.0	1.5	0.075	2.6	0.026	2.4	0.52	0.31
1.7584 – 1.884	1.84	9.6	4.0	6.7	0.71	0.21	2.7	0.12	1.3	0.43	3.4
1.884 – 2.0096	1.74	9.2	4.2	6.8	0.30	0.76	2.7	0.085	1.6	0.36	1.1
2.0096 – 2.1352	1.97	9.1	3.8	6.8	0.69	0.59	2.5	0.0042	2.7	0.55	0.19
2.1352 – 2.2608	2.10	7.9	3.6	5.8	0.16	0.45	2.5	0.022	0.67	0.72	0.15
2.2608 – 2.3864	2.42	8.1	3.3	6.2	0.40	0.25	2.6	0.035	1.5	0.21	1.0
2.3864 – 2.512	2.28	8.5	3.5	6.4	0.40	0.70	2.7	0.088	0.80	0.58	1.9
2.512 – 2.6376	2.51	7.4	3.3	5.2	0.48	0.037	2.5	0.0014	1.7	0.43	1.0
2.6376 – 2.7632	2.71	7.8	3.1	5.8	0.75	0.38	2.6	0.052	1.7	0.33	1.5
2.7632 – 2.8888	2.69	7.9	3.1	5.9	0.16	0.13	2.5	0.0093	1.8	0.60	1.4
2.8888 – 3.0144	2.78	7.8	3.1	5.9	0.40	0.20	2.6	0.040	1.1	0.25	1.6
3.0144 – 3.14	3.04	7.4	2.8	5.5	0.11	0.15	2.7	0.10	1.5	0.44	1.4

Table A.37: Differential cross section in $\Delta\phi_{\text{jet2,jet3}}$ ($N_{\text{jets}} \geq 3$) and break down of the systematic uncertainties for the muon decay channel.

$\Delta\phi_{\text{jet2,jet3}}$	$\frac{d\sigma}{d\Delta\phi_{\text{jet2,jet3}}}$ [pb]	Tot. Unc [%]	stat [%]	JES [%]	JER [%]	Eff [%]	Lumi [%]	XSec [%]	PU [%]	LES+LER [%]	Unf sys [%]
0 – 0.1256	1.64	9.5	3.3	7.8	0.67	0.54	2.6	0.063	1.5	0.33	0.86
0.1256 – 0.2512	1.76	9.1	3.5	7.1	0.33	0.20	2.6	0.066	1.4	0.35	1.6
0.2512 – 0.3768	1.85	10.	3.5	8.7	0.53	0.88	2.5	0.022	0.92	0.22	0.29
0.3768 – 0.5024	2.40	7.8	3.0	6.0	0.38	0.25	2.5	0.026	1.8	0.33	0.78
0.5024 – 0.628	2.23	9.8	3.1	8.3	0.57	0.91	2.4	0.040	1.4	0.13	1.3
0.628 – 0.7536	2.07	8.4	3.2	6.8	0.58	0.34	2.5	0.026	0.75	0.54	0.084
0.7536 – 0.8792	1.77	9.0	3.6	6.4	0.33	0.13	2.8	0.14	2.1	0.28	2.6
0.8792 – 1.0048	1.81	9.0	3.7	6.9	0.81	0.0079	2.5	0.019	1.8	0.24	0.88
1.0048 – 1.1304	1.64	9.5	3.9	6.5	0.43	0.56	2.8	0.16	1.6	0.16	3.6
1.1304 – 1.256	1.71	9.4	3.7	6.8	0.19	0.13	2.7	0.11	2.0	0.35	2.9
1.256 – 1.3816	1.60	9.2	3.9	7.2	0.048	0.86	2.6	0.029	1.0	0.55	0.64
1.3816 – 1.5072	1.73	9.2	3.7	7.3	0.11	0.36	2.5	0.0088	1.8	0.18	0.20
1.5072 – 1.6328	1.46	10.	4.4	7.5	0.40	0.21	2.6	0.067	1.6	0.62	1.6
1.6328 – 1.7584	1.76	8.5	3.7	6.4	0.030	0.41	2.6	0.029	1.4	0.27	0.24
1.7584 – 1.884	1.67	9.9	4.0	5.5	0.84	0.51	2.9	0.23	1.6	0.20	5.5
1.884 – 2.0096	1.64	10.	4.0	8.1	0.52	0.098	2.4	0.041	1.9	0.24	1.1
2.0096 – 2.1352	1.78	9.5	3.7	7.0	0.20	0.20	2.7	0.12	1.5	0.067	3.1
2.1352 – 2.2608	1.72	9.7	3.9	7.7	0.24	0.44	2.7	0.11	1.6	0.24	0.98
2.2608 – 2.3864	1.72	8.6	3.9	6.2	0.66	0.50	2.5	0.017	1.7	0.34	1.2
2.3864 – 2.512	1.96	8.7	3.6	6.4	0.59	0.46	2.7	0.11	1.8	0.44	1.6
2.512 – 2.6376	1.94	9.3	3.8	7.5	0.38	0.21	2.5	0.020	1.1	0.21	0.74
2.6376 – 2.7632	1.96	8.9	3.6	6.6	0.13	0.54	2.7	0.11	1.1	0.33	2.2
2.7632 – 2.8888	1.96	8.5	3.6	6.1	0.74	0.39	2.7	0.096	1.4	0.34	2.1
2.8888 – 3.0144	1.84	9.4	3.8	7.2	1.0	0.63	2.5	0.017	2.2	0.13	1.0
3.0144 – 3.14	2.11	9.4	3.2	7.6	0.63	0.18	2.7	0.11	1.4	0.21	2.1

List of Abbreviations

Chin. Phys.	....	Chinese Physics
Commun. Math. Phys.	....	Communications in Mathematical Physics
Comput. Phys. Commun.	....	Computer Physics Communications
Conf. Proc.	....	Conference Proceedings
Eur. Phys. J	....	European Physics Journal
IEEE Trans. Nucl. Sci.	....	IEEE Transactions on Nuclear Science
JHEP	....	Journal of High Energy Physics
JINST	....	Journal of Instrumentation
Nucl. Phys.	....	Nuclear Physics
Phys. Lett.	....	Physics Letters
Phys. Rev.	....	Physics Review
Phys. Rev. Lett.	....	Physics Review Letters

References

(1994). CMS, the Compact Muon Solenoid: Technical proposal.

Aaboud, M., Aad, G., Abbott, B., Abdallah, J., Abdinov, O., Abeloos, B., Aben, R., AbouZeid, O. S., Abraham, N. L., and et al. (2016). Measurements of the Production Cross Section of a Z Boson in Association with Jets in pp collisions at $\sqrt{s} = 13$ TeV with the ATLAS Detector.

Aad, G. et al. (2012a). Measurement of the production cross section for Z/gamma* in association with jets in pp collisions at $\sqrt{s} = 7$ TeV with the ATLAS detector. *Phys. Rev.*, D85:032009.

Aad, G. et al. (2012b). Observation of a new particle in the search for the Standard Model Higgs boson with the ATLAS detector at the LHC. *Phys. Lett.*, B716:1–29.

Aad, G. et al. (2013). Measurement of the production cross section of jets in association with a Z boson in pp collisions at $\sqrt{s} = 7$ TeV with the ATLAS detector. *JHEP*, 07:032.

Aaij, R. et al. (2016). Measurement of forward W and Z boson production in association with jets in proton-proton collisions at $\sqrt{s} = 8$ TeV. *JHEP*, 05:131.

Aaltonen, T. A. et al. (2015). Measurement of Differential Production Cross Section for Z/γ^* Bosons in Association with Jets in $p\bar{p}$ Collisions at $\sqrt{s} = 1.96$ TeV. *Phys. Rev.*, D91(1):012002.

Abazov, V. M. et al. (2008). Measurement of differential Z/γ^* + jet + X cross sections in $p\bar{p}$ collisions at $\sqrt{s}$ = 1.96-TeV. *Phys. Lett.*, B669:278–286.

Adam, W., Mangano, B., Speer, T., and Todorov, T. (2005). Track reconstruction in the CMS tracker.

Alioli, S., Bauer, C. W., Berggren, C., Tackmann, F. J., and Walsh, J. R. (2015). Drell-Yan production at NNLL'+NNLO matched to parton showers. *Phys. Rev.*, D92(9):094020.

Alioli, S., Bauer, C. W., Berggren, C. J., Hornig, A., Tackmann, F. J., Vermilion, C. K., Walsh, J. R., and Zuberi, S. (2013). Combining Higher-Order Resummation with Multiple NLO Calculations and Parton Showers in GENEVA. *JHEP*, 09:120.

Alioli, S., Nason, P., Oleari, C., and Re, E. (2010). A general framework for implementing NLO calculations in shower Monte Carlo programs: the POWHEG BOX. *JHEP*, 06:043.

Allison, J. et al. (2006). GEANT4 developments and applications. *IEEE Trans. Nucl. Sci.*, 53:270.

Altarelli, G. and Parisi, G. (1977). Asymptotic Freedom in Parton Language. *Nucl. Phys.*, B126:298–318.

Alwall, J., de Visscher, S., and Maltoni, F. (2009). QCD radiation in the production of heavy colored particles at the LHC. *JHEP*, 02:017.

Alwall, J. et al. (2008). Comparative study of various algorithms for the merging of parton showers and matrix elements in hadronic collisions. *Eur. Phys. J.*, C53:473–500.

Alwall, J., Frederix, R., Frixione, S., Hirschi, V., Maltoni, F., Mattelaer, O., Shao, H.-S., Stelzer, T., Torielli, P., and Zaro, M. (2014). The automated computation of tree-level and next-to-leading order differential cross sections, and their matching to parton shower simulations. *JHEP*, 07:079.

Ball, R. D., Bertone, V., Carrazza, S., Deans, C. S., Del Debbio, L., Forte, S., Guffanti, A., Hartland, N. P., Latorre, J. I., Rojo, J., and Ubiali, M. (2013). Parton distributions with LHC data. *Nucl. Phys. B*, 867:244.

Ball, R. D. et al. (2015). Parton distributions for the LHC Run II. *JHEP*, 04:040.

Bruning, O. S., Collier, P., Lebrun, P., Myers, S., Ostojic, R., Poole, J., and Proudlock, P. (2004). LHC Design Report Vol.1: The LHC Main Ring.

Cabibbo, N. (1963). Unitary Symmetry and Leptonic Decays. *Phys. Rev. Lett.*, 10:531–533. [,648(1963)].

Cacciari, M., Salam, G. P., and Soyez, G. (2008). The anti-k_t jet clustering algorithm. *JHEP*, 04:063.

Cacciari, M., Salam, G. P., and Soyez, G. (2008). The anti-k_t jet clustering algorithm. *Journal of High Energy Physics*, 2008(4):063.

Cacciari, M., Salam, G. P., and Soyez, G. (2012). FastJet user manual. *Eur. Phys. J. C*, 72:1896.

Callan, Jr., C. G. (1970). Broken scale invariance in scalar field theory. *Phys. Rev.*, D2:1541–1547.

Calvetti, D., Reichel, L., and Shuibi, A. (2004). L-Curve and Curvature Bounds for Tikhonov Regularization. *Numerical Algorithms*, 35:301–314.

Campbell, J. M., Ellis, R. K., and Williams, C. (2011). Vector boson pair production at the LHC. *JHEP*, 07:018.

Chatrchyan, S. et al. (2008). The CMS experiment at the CERN LHC. *JINST*, 3:S08004.

Chatrchyan, S. et al. (2011). Measurement of the Inclusive W and Z Production Cross Sections in pp Collisions at $\sqrt{s} = 7$ TeV. *JHEP*, 10:132.

Chatrchyan, S. et al. (2012a). Jet Production Rates in Association with W and Z Bosons in pp Collisions at $\sqrt{s} = 7$ TeV. *JHEP*, 01:010.

Chatrchyan, S. et al. (2012b). Observation of a New Boson at a Mass of 125 GeV with the CMS Experiment at the LHC. *Phys. Lett.*, B716:30–61.

Chatrchyan, S. et al. (2012c). Performance of CMS Muon Reconstruction in pp Collision Events at $\sqrt{s} = 7$ TeV. *JINST*, 7:P10002.

Chatrchyan, S. et al. (2014). Description and performance of track and primary-vertex reconstruction with the CMS tracker. *JINST*, 9:P10009.

CMS Collaboration (2015). Event generator tunes obtained from underlying event and multiparton scattering measurements. *arXiv e-prints*, page arXiv:1512.00815.

Collaboration, C. (2014). Pileup Removal Algorithms.

Collaboration, C. (2017). CMS Luminosity Measurements for the 2016 Data Taking Period.

Drell, S. D. and Yan, T.-M. (1970). Massive Lepton Pair Production in Hadron-Hadron Collisions at High-Energies. *Phys. Rev. Lett.*, 25:316–320. [Erratum: Phys. Rev. Lett.25,902(1970)].

Frederix, R. and Frixione, S. (2012). Merging meets matching in MC@NLO. *Journal of High Energy Physics*, 2012:61.

Frederix, R. and Frixione, S. (2012). Merging meets matching in MC@NLO. *JHEP*, 12:061.

Frederix, R., Frixione, S., Hirschi, V., Maltoni, F., Pittau, R., and Torrielli, P. (2012). Four-lepton production at hadron colliders: aMC@NLO predictions with theoretical uncertainties. *JHEP*, 02:099.

Frixione, S., Nason, P., and Oleari, C. (2007a). Matching NLO QCD computations with parton shower simulations: the POWHEG method. *JHEP*, 11:070.

Frixione, S., Nason, P., and Ridolfi, G. (2007b). A Positive-weight next-to-leading-order Monte Carlo for heavy flavour hadroproduction. *JHEP*, 09:126.

Glashow, S. L. (1961). Partial Symmetries of Weak Interactions. *Nucl. Phys.*, 22:579–588.

Hazen, E., Heister, A., Hill, C., Rohlf, J., Wu, S. X., and Zou, D. (2013). The AMC13xg: a new generation clock/timing/DAQ module for CMS MicroTCA. *Journal of Instrumentation*, 8(12):C12036–C12036.

Higgs, P. (1964). Broken symmetries, massless particles and gauge fields. *Physics Letters*, 12(2):132 – 133.

Khachatryan, V. et al. (2015a). Comparison of the Z/γ^* + jets to γ + jets cross sections in pp collisions at $\sqrt{s} = 8$ TeV. *JHEP*, 10:128. [Erratum: JHEP04,010(2016)].

Khachatryan, V. et al. (2015b). Measurements of jet multiplicity and differential production cross sections of $Z+$ jets events in proton-proton collisions at $\sqrt{s} = 7$ TeV. *Phys. Rev.*, D91(5):052008.

Khachatryan, V. et al. (2015c). Performance of Electron Reconstruction and Selection with the CMS Detector in Proton-Proton Collisions at sqrt(s) = 8 TeV. *JINST*, 10(06):P06005.

Khachatryan, V. et al. (2015d). Performance of photon reconstruction and identification with the CMS detector in proton-proton collisions at $\sqrt{s} = 8$ TeV. *JINST*, 10:P08010.

Khachatryan, V. et al. (2016). Event generator tunes obtained from underlying event and multiparton scattering measurements. *Eur. Phys. J.*, C76(3):155.

Khachatryan, V. et al. (2017a). Measurements of differential production cross sections for a Z boson in association with jets in pp collisions at $\sqrt{s} = 8$ TeV. *JHEP*, 04:022.

Khachatryan, V. et al. (2017b). The CMS trigger system. *JINST*, 12(01):P01020.

Lai, H.-L., Huston, J., Li, Z., Nadolsky, P., Pumplin, J., Stump, D., and Yuan, C.-P. (2010). Uncertainty induced by QCD coupling in the CTEQ global analysis of parton distributions. *Phys. Rev. D*, 82:054021.

Nason, P. (2004). A new method for combining NLO QCD with shower Monte Carlo algorithms. *JHEP*, 11:040.

Patrignani, C. et al. (2016). Review of Particle Physics. *Chin. Phys.*, C40(10):100001.

Salam, A. (1968). Weak and Electromagnetic Interactions. *Conf. Proc.*, C680519:367–377.

Schmitt, S. (2012). TUnfold, an algorithm for correcting migration effects in high energy physics. *Journal of Instrumentation*, 7(10):T10003–T10003.

Sirunyan, A. M. et al. (2017). Particle-flow reconstruction and global event description with the cms detector. *JINST*, 12:P10003.

Sirunyan, A. M. et al. (2018). Measurement of differential cross sections for Z boson production in association with jets in proton-proton collisions at $\sqrt{s} = 13$ TeV. *Eur. Phys. J.*, C78(11):965.

Sjöstrand, T., Ask, S., Christiansen, J. R., Corke, R., Desai, N., Ilten, P., Mrenna, S., Prestel, S., Rasmussen, C. O., and Skands, P. Z. (2015). An introduction to PYTHIA 8.2. *Comput. Phys. Commun.*, 191:159.

Sjöstrand, T., Mrenna, S., and Skands, P. (2008). A brief introduction to PYTHIA 8.1. *Computer Physics Communications*, 178(11):852–867.

Symanzik, K. (1970). Small distance behavior in field theory and power counting. *Commun. Math. Phys.*, 18:227–246.

Tikhonov, I. V. (1963). Solution of incorrectly formulated problems and the regularization method. *Soviet Mathematics*, 4(1):1023–1038.

Weinberg, S. (1967). A model of leptons. *Phys. Rev. Lett.*, 19:1264–1266.

CURRICULUM VITAE

Daniel John Arcaro

Boston University
Physics Department
590 Commonwealth Ave.
Boston, MA 02215

Email: djarcaro@bu.edu
Phone: 508-479-8049

EDUCATION

Ph.D. Candidate, Physics Graduate Program, Boston University, 2013-Present

Thesis: Measurement of the total and differential cross section of Z boson production in association with jets in proton-proton collisions at $\sqrt{s} = 13$ TeV.âĂİ

Advisor: Lawrence R. Sulak

PhD committee members: Profs. J.Butler, S. Glashow, R. Carey, K. Ludwig, I. Suarez

B.A. Physics, Boston University, 2013

EMPLOYMENT

Boston University - Physics Graduate Program

2013-Present Research Assistant, Boston University CMS Group

2013-2015 Teaching Fellow, Boston University Physics Department

Boston University - College of Arts and Sciences

2011-2013 Research Assistant, Multi-functional Materials Spectroscopy Laboratory

PROFESSIONAL SKILLS

Programming C++, C, Python, VHDL, LaTeX, HTML, bash

Software Vivado, CMSSW, ROOT, MATLAB, LabView, MS Office, AutoCAD, SOLIDWORKS, Fusion360

Hardware Analog and digital circuitry, fast electronics, FGPAs, photo-detectors, Calorimetry, Standards: NIM, CAMAC, VME, uTCA, ATCA

Platforms Linux/Unix, Windows, Mac OS

Machining CNC and manual machining, 3D printing

Optics Pump probe spectroscopy, chopper with lock-in amplifier, laser alignment

PUBLICATIONS AND PRESENTATIONS

Articles

CMS Collaboration "Multi-differential Z+jets cross sections at 13 TeV" CMS pre-approved SMP-19-009.

CMS Analysis Note Contributions

CMS AN-2018/005 – Measurement of the Z boson differential cross sections in the muon channel in association with jets in proton-proton collisions at sqrt(s) = 13 TeV

CMS AN-2018/310 – Z boson differential cross sections in the electron channel in association with jets in proton-proton collisions at sqrt(s) = 13 TeV

Presentations

2019 "Precision Measurement of Z+jets" DPF Grad Slam, APS April 2019, Denver, CO

2019 "Electroweak and QCD aspects in V+jets" APS April 2019, Denver, CO

2018 "Electroweak and QCD aspects in V+jets" Pheno2018: Phenomenology 2018 Symposium, Pittsburgh, PA

RESEARCH AND LABORATORY EXPERIENCE

Boston University Physics Department

High Energy Physics Group, CMS Experiment

Work on the Compact Muon Solenoid (CMS) at the Large Hadron Collider (LHC) at the European Organization for Nuclear Research (CERN) particle physics laboratory. Member of the CMS Hadron Calorimeter (HCAL) subsystem operations team.

- Developed software for monitoring the data integrity of the AMC13 data acquisition (daq) card used in micro-telecommunications crates for CMS.
- Diagnosed and fixed the HCAL daq system during the 2016 run 2 as an on site 24/7 on call expert for 1 year.

– Maintained all AMC13 cards on HCAL and other subsystems and coordinated firmware and software updates into the HCAL daq system.

– Implemented an increase in the AMC13 data throughput by a factor of 2 in anticipation of larger data volumes in the 2017 and 2018 LHC runs.

– Involved in HCAL daq operations at the CERN testbeam and re-cabling new electronics and took data taking shifts.

– Mentoring undergraduate and graduate students on CMS analysis projects: Chris Cosby (BU), Peter Riley (Tufts).

– Training graduate students to continue with AMC13 operations support at CERN: Chris Cosby (BU), Siqi Yuan (BU).

– Assisting PI with writing grant proposal/progress report and recruiting graduate students.

Boston University Physics Department
Prof. Lawrence Sulak, Advanced Laboratory

– Measured the lifetime of a muon using a water Cherenkov chamber equipped with photomultiplier tubes and fast electronics.

– Resolved the angular distribution of cosmic muons and measured Helium-3 thermal neutron capture using a state of the art time projection chamber.

– Gained experience with high-temperature superconductors and optical techniques including Rubidium optical pumping and Faraday rotation measurements.

– Characterized terrestrial and cosmic background radiation at sea level with a Sodium Iodide crystal and multi-channel analyzer.

– Observed single photon diffraction with visible laser light and photomultiplier tube counter.

Boston University Physics Department
Prof. Richard Averitt, Multi-functional Materials Spectroscopy Laboratory

– Developed a high field Terahertz spectroscopy apparatus to investigate photo-induced phase transitions in correlated electron material such as Vanadium Oxide.

– Collaborated with colleagues from the condensed matter theory group at Boston University to investigate phase transitions in 5CB Liquid Crystals. The time dynamics of the first and second order transitions was measured and compared to simulated Ising model magnetic transitions.

TEACHING EXPERIENCE

Boston University

2014, 2015 *Electronics for Scientists*

Teaching Assistant, BU PY681 Electronics for Scientists. Application of analog circuitry to research such as filters, amplifiers, and comparators. Digital electronics with an Arduino for DAC/ADC, displays, and stepper motor controls.

2013, 2014 *Advanced Laboratory*

Teaching Assistant, BU PY581 Advanced Laboratory (24 students). Teaching one eight-hour lab section per week. Assisting students on classical experiments in atomic and nuclear physics. Improving existing apparatuses, formulating new experiments, and guiding students' research projects. Experiments include magnetic resonance, nuclear-decay studies, Zeeman effect, holography, black-body radiation, cosmic ray detection, muon lifetime measurement, and X-ray diffraction.

2014 *General Physics*

Teaching Assistant, BU PY211 Calculus-based general physics for scientists and engineers. Teaching three hour lab sections per week. Guiding student in successful completion of experiments. Teaching both fundamental concepts and advising hands-on troubleshooting skills. Topics include Newtonian mechanics, basic fluid mechanics, and thermal physics.

AWARDS RECEIVED

2016 Department of Physics Teaching Fellow of the Year Award

2013 Graduated Cum Laude at Boston University

2011-2013 Dean's List at Boston University

2011 Undergraduate Research Opportunities Program at Boston University Summer Funding recipient

OUTREACH

2018 Boston University Women in physics panel session: Life After a Physics BA

Panelist: Advice on finding a research adviser and typical work as a CMS graduate student

2018 Boston University Artemis Project

Instructor: Taught soldering and basic programming for an Arduino based art project

2018 Big Bang Science Fair at WaterFire Providence, RI

Student assistant: demonstrated Physics of Food experiments with Prof. Rama Bansil

2016-2018 Boston University Physics Department Open House

Student host: assisted with student-run welcome dinners for prospectus students, presented research projects during poster sessions

2016 Boston University CAS Alumni Dinner

Student assistant: helped Prof. Rama Bansil with Physics of Food demonstrations

2011-2013 Boston University SET in the City

Photon Representative: classic physics demonstrations to attract high school girls to STEM

2011-2013 Boston University Physics Club

Club president: Weekly meeting organization, set up outreach for BU physics students in the Boston area, coordinated BU annual pumpkin drop and cleanup crew

REFERENCES

Prof. Lawrence Sulak
Professor of physics, Boston University
Phone: 617-735-7637, Email: sulak@physics.bu.edu

Eric Hazen
Director of Electronics Design Facility, Boston University
Phone: 617-448-9705, Email: hazen@bu.edu

Dr. Philippe Gras
Universite Paris-Saclay (FR)
Philippe.Gras@cern.ch

CMS COLLABORATORS

Dr. Paolo Azzurri ∘ Dr. Pawel De Barbaro ∘ Assoc. Prof. Emanuela Barberis ∘ Asst. Prof. Zeynep Demiragli ∘ Prof. Elisabetta Gallo ∘ Prof. James Rohlf ∘ Dr. David Sperka